2003

Ultrasonic characterization of engineering performance of oriented strandboard

Ronnie Yunheu Vun
Louisiana State University and Agricultural and Mechanical College

ULTRASONIC CHARACTERIZATION OF ENGINEERING PERFORMANCE OF ORIENTED STRANDBOARD

A Dissertation

Submitted to the Graduate School of the
Louisiana State University and
Agricultural and Mechanical College
in partial fulfillment of the
requirements for the degree of
Doctor of Philosophy

In

The School of Renewable Natural Resources

by

Ronnie Yunheu Vun

Dip., Universiti Pertanian Malaysia at Kuching, 1984
B.S., University of the Philippines at Los Baňos, 1994
M.F., University of the Philippines at Los Baňos, 1995
M.S., University of California at Berkeley, 1998

August, 2003

ACKNOWLEDGMENTS

This research was funded in part by USDA NRI-CGP 99-351103-8298. Many thanks are due to my thesis advisor, Dr. Qinglin Wu, for inspiring this research, for his mentoring and patience, and for his continued support. Thanks to Dr. W. Ramsay Smith for his constant motivation; Dr. Quang V. Cao for his eveready to solve my inquiries; Ms. Pat LeFeaux for their invaluable administrative supports. Acknowledgment is due to Dr. Eyassu Woldensenbet for his teaching in composite mechanics; Dr. Charles J. Monlezun for his skillful analytical approaches; Dr. Aravamudhan Raman for his suggestions in material science; Dr. Richard L. Kurtz, an active committee member; Dr. Richard P. Vlosky and Dr. Paul Burns for their personal helps and reviews of the manuscripts. Utmost gratitude is due to Mr. Mahesh C. Bhardwaj and Mr. Gary Stead of Ultran/Secondwave Systems for cordially providing the non-contact ultrasonic measurements. My vintage car is due to the memory of Dr. Elvin T. Choong. Memorable experiences and a friend are due to fellows: Dr. Sunyoung Lee, Dr. Jong Lee, Dr. John Lu, XW Xu, Dr. XF Duan, and Dr. GP Han for making stay at LSU enjoyable. Indebted to Mr. Cyril T. Pinso of Innoprise Corporation and Prof. Frank C. Beall of University of California at Berkeley for making the first leap to the U.S. possible. Tom Breiner "Gumby", Dr. Cadian Lou, Dr. Liheng Chen, and those not mentioned for their pleasant hospitality and technical assistances indirectly have contributed to my success. For my daughters Melissa and Vanessa, and my parents Apapa and Amama, without you the struggle and sacrifices mean nothing. The constant encouragements and teachings of the Good News from friends of The Chapel On The Campus give spiritual enlightenments and forgiveness. For all these graces, I thank God.

TABLE OF CONTENTS

LIST OF TABLES

LIST OF FIGURES

ABTRACT

Direct-contact (DC) and non-contact (NC) ultrasonic transmission (UT) methods were developed to characterize the structural performance of oriented strandboard (OSB). The UT variable velocity was shown to be sensitive to the physical impediments caused by flake interfacial boundaries and embedded voids. Both attenuation and root mean square (RMS) voltage were good indicators of the "zero void" densification level for OSB, a point of the greatest transmissivity of the stress wave energy.

For both DC and NC methods, the predicted densities of the model were validated for spatial distribution over each OSB type. Based on the EN300 standard for panel manufacturing, the control limits were ±10% of the panel average density. The density prediction was found to improve with higher resin content (RC) and higher nominal density (ND) levels. From the out-of-limits plots, the predicted *in-situ* densities produced a reasonably spatial coherence to the measured values. All panels made with ND 0.60 g/cm^3 or greater conformed well within the limits, with declining conformity towards lower RC panels.

For each composite type made of different particle sizes, the equilibrium moisture content showed a decreasing trend toward smaller particle panels. The attenuation and RMS were good indicators for moisture change and densification level for each composite type. The velocity, sensitive to physical resistance of

particle sizes, increased with increasing IB strength and sample density, manifesting the positive influence of layering, resin content, and the negative effect of bark as a constituent.

The results of the creep rupture tests on commercial OSB using an acoustic emission (AE) technique indicated that the cumulative AE event count parameter was highly correlated with deflection parameter and appropriately represented the accumulation of incipient damage. Under high stress levels, specimens with high moisture content (MC) sustained the worse damages having the shortest creep rupture time followed by specimens with dynamically rising MC. Defects on the compression-side of the bending specimen were found critical to creep rupture than those on the tension-side. The in-plane fracture patterns tended to follow the defect trenches of low-density valleys, and worsened with greater variability of the horizontal density, indicating the need to measure and control the horizontal density variation within reasonable limits.

CHAPTER 1. INTRODUCTION

1.1. RESEARCH RATIONALE

Oriented strandboard (OSB) is a reconstituted wood composite using wood strands oriented in crisscrossing layers bonded together with an exterior thermosetting resin. In 2000, OSB production in North America exceeded 1.93 billion m^2 (9.5-mm basis) overtaking plywood production (Najera and Spelter 2001). The production gap is expected to widen in the near future. Particularly, the making of mixed hardwood OSB utilizing the abundantly low-grade hardwoods has boosted OSB production over plywood. Since the 1990's, OSB has proven to be an economical and competitive structural panel (Anon. 2003) used as underlayment, sheathing, and I-joist in commercial and residential construction.

Desired mechanical properties of OSB can be improved by modifying resin type and content, strand size, type and alignment, and layering (Wu 1999, Lee and Wu 2002). However, embedded interspatial voids consider an inherent defect occurring in the manufacturing of OSB due to furnish characteristics and imperfections of mat forming processes (Suchsland 1962, Lenth and Kamke 1996). Both random flake deposition in OSB mat forming and processing factors can create uneven vertical and horizontal density distribution (Oudjehane and Lam 1998, Winistorfer et al. 2000, Wolcott et al. 1990). Large in-plane density variation can severely deteriorate the mechanical properties, jeopardizing the structural integrity and durability of the panels.

A waferboard mat model developed by Smith (1982) illustrates the variability of the in-plane density caused by columns of different densities compressed to panel thickness and of lesser-compacted densities consisting of interspatial voids. Mathematical models have been developed to simulate OSB's mat forming and density variations (Suchsland and Xu 1989, Steiner and Dai 1993, Lu and Lam 2001, Kruse et al. 2000). Quality improvement in OSB, thus, depends largely on a fundamental understanding of the density variation. Linville (2000), Wolcott et al. (2000), and Bozo (2002) studied the effect of mechanical degradation due to the spatial horizontal density distribution in OSB. In other composites, strength failure is primarily due to embedded voids (Jeong 1997, Jeong and Hsu 1995). For each one percent of void content, the mechanical strength of the composite is reduced by 7% (Judd and Wright 1978). There is still lack of experimental techniques to actually measure the horizontal density variation in OSB.

Voids in wood composites have been studied by numerous empirical and destructive investigation methods and protocols, such as density determination, fluid/water absorption, photomicrography, microscopic-image analysis, and radiography. These methods are laborious, time-consuming, cost-ineffective, and often hazardous, leading to non-comparable results. The innovation of nondestructive applications in forest products gave impetus to the current research. Nondestructive ultrasonic inspection is an alternative to measure the constitutive impacts of voids in material behavior and horizontal properties distribution of

wood composites without destroying the specimens. This applied research was motivated and conducted to characterize the engineering performance of OSB.

1.2. OSB HISTORY AND UTILIZATION

James d'A Clark developed the first manufacturing facility to produce waferboard at Sand Point, Idaho in 1950 (Huber 2002). A decade later, MacMillan Bloedel operated the first commercial waferboard plant at Hudson Bay, Saskatchewan. Blandin Wood Products of Grands Rapids, Minnesota was the first successful U.S. waferboard producer. Waferboard technology soon gave way to OSB for its superior mechanical properties. Instead of using a flat square wafer, OSB uses wood strands oriented in crisscrossing layers, which gives mechanical properties similar to softwood plywood. Elmendorf Manufacturing Company operated the first OSB facility in Clairemont, New Hampshire in early 1980's (www.apawood.org). By the early 1990's, most waferboard mills had been converted to produce OSB. OSB production continues to grow favorably with consumer acceptance for a cheaper, comparable structural panel over softwood plywood.

Other industrial uses for OSB are formwork panels, recreational vehicles, truck bodies, displays, manufactured housing, pallets-containers, furniture, shelving and cabinets (Juslin and Hansen 2002). Over a decade, the utilization of OSB has doubled its volume in residential and commercial construction (Najera and Spelter 2001). Reconstituted panel industries indeed hold an important

conservational role to forest resources by salvaging low quality or waste resources and converting them into use.

1.3. QUALITY STANDARDS FOR OSB

In the United States, OSB is manufactured conforming to the Performance Standard PS 2-92 of the National Institute of Standards and Technology, and is certified for wall, exterior siding and roof sheathing, structural insulated panels, sub-flooring, I-joist, and underlayment in building construction. In Canada, panels must comply with the Canadian Standards Association's CSA 0325 Construction Sheathing or its CSA 0437 OSB and Waferboard. All three standards set the maximum values for deflection under load, thickness swell, linear expansion, and minimum values for strength, stiffness, and lateral nail loads (Smulski 1997).

Under the PS 2-92, a manufacturer is required to maintain an in-plant quality control program demonstrating that its panels conform with the requirements of the chosen standard (Forest Products Laboratory 1999). Concurrently, the finished structural panels are performance-rated by a third party recognized by the National Evaluation Service, Timber Engineering Company (TECO), PFS Corporation or other private companies operating closely in each state. Therefore, a continuing effort to improve and monitor the panel properties in a different way, such as nondestructive and non-intrusively online techniques, would assure product quality and growth while guaranteeing consumer safety and product satisfaction, and conserving the natural resources.

1.4. NONDESTRUCTIVE EVALUATION OF WOOD COMPOSITES

Nondestructive evaluation (NDE) of wood composites has surpassed the benefits of conventional methodologies in the field of wood science and technology. Variants of nondestructive techniques have successful applications in the forest product sector in the areas of defect and decay detection in solid wood, sorting or grading of structural wood products (machine stress rating), *in-situ* structural evaluation of wooden members, health monitoring of living trees, detection of termites, and online monitoring of resin curing (Beall 2002). Most frequently used nondestructive testing methods are the stress wave, ultrasonic, acoustic emission, and acousto-ultrasonic methods. Other conventional methods are the drill resistography, screw withdrawal, pilodyn, x-ray, isotope technologies, or sniffing dogs to identify dry fungus rot.

The effectiveness of the nondestructive testing techniques depends on the correlation of certain parameters to the mechanical properties of wood products. The characterization of the properties can be done with a through-thickness ultrasonic transmission (UT) method. In this study, an ultrasonic wave was transmitted through the panel thickness to characterize the internal structure of a particular panel. Knowing the process variables and material constituents of the panels, the internal structure drives the ultrasonic responses forming a basis for property correlation and hence, a characterization algorithm can be obtained. The UT technique, either direct-contact or non-contact, is a feasible tool for optimization of strength properties based on densification level particular to the

composite panels. Manufacturing OSB at the densification level would minimize, if not eliminate, the adverse impact of voids on the product quality.

Many material scientists acknowledged the technical problems in the use of ultrasound with wood-flake panels. The application of ultrasound in wood composites research was beset with high signal attenuation, wood anisotropy and growth properties, and interfacial boundaries in the wood composites (Ermolov 1998). These problems pose a technical challenge to push developmental nondestructive technology into forest products. Both the interfacial boundaries and interspatial voids form strong scatters of the elastic waves as a response to the balance of the material constituents and processing variables (fiber, flake geometry, particle size, impurities, moisture content, resin content and type) in panel fabrication.

1.5. DISSERTATION OUTLINES

The dissertation is arranged based on the following general objectives of the research.

1. To develop Direct Contact (DC) & Non-Contact (NC) UT techniques for characterizing OSB engineering properties;
2. To apply the UT techniques for mapping the horizontal density variation in OSB;
3. To study the UT responses in bio-based composites made of different particle sizes; and

4. To explore the acoustic emission technique for assessing creep rupture and critical defect locations in OSB.

The objectives were accomplished during the course of research and the results are presented as in the following chapters. This chapter (**Chapter 1**) provides an overall introduction to the dissertation. **Chapter 2** shows the development of the DC and NC ultrasonic techniques to inspect the internal structures of OSB as influenced by the processing variables. Inspection of the horizontal density variation over whole panels using the DC method is described in **Chapter 3**. The NC ultrasonic mapping methodology is presented in **Chapter 4**. In **Chapter 5**, the technique of using DC method to compare the UT responses of various bio-based composite panels made with different particle sizes is described. **Chapter 6** presents an acoustic emission methodology to evaluate location of critical defects in bending and monitor creep rupture behaviors of commercial OSB specimens under high stress levels in different equilibrium moisture content regimens.

1.6. REFERENCES

Anon. 2003. OSB fast facts. *In* http://www.osbguide.com/osbfacts.html, Structural Board Associations, Toronto, Ontario, Canada.

Beall, F.C. 2002. Overview of the use of ultrasonic technologies in research on wood properties. Wood Sci. Technol. (36): 197-212.

Bozo, Alejandro M. 2002. Spatial variation of wood composites. Ph.D Dissertation, Department of Civil and Environmental Engineering, Washington State University, Pullman, WA.

Ermolov, I.N. 1998. Major ultrasonic inspection problem. Russian Journal of Nondestructive Testing 34(1):35-37. Plenum Publishing, New York.

Forest Products Laboratory. 1999. Wood handbook – wood as an engineering material. Gen. Tech. Rep FPL-GTR-113, Madison, WI: U.S. Department of Agriculture, Forest Service, Forest Products Laboratory. 463p.

Huber, Dean W. 2002. Wood technology award for excellence: a history of what, why, and who. *In* www.woodwideweb.com/PDFs/FIAWARDhistoryarticle11.pdf

Jeong, H. 1997. Effects of voids on the mechanical strength and ultrasonics attenuation of laminated composites. Journal of Composite Materials 31(3): 276-292.

Jeong, H., and D.K. Hsu. 1995. Experimental analysis of porosity-induced ultrasonic attenuation and velocity change in carbon composites. Ultrasonics 33(3): 195-203.

Judd, N.C.W., and W.W. Wright. 1978. Voids and their effects on the mechanical properties of composites-An appraisal. SAMPE Journal, January/February:10-14.

Juslin, Heikki, and Eric Hansen. Strategic marketing in the global forest industries. Authors Academic Press, Corvallis, OR. 607p.

Kruse, K., C. Dai, and A. Pielasch. 2000. An analysis of strand and horizontal density distributions in oriented strand board. Holz Roh-Werkstoff 58(4):270-277.

Najera, J., and H. Spelter. 2001. Wood-based panels – supply, trade, and consumption. In: UN – ECE/FAO Forest Products Annual Market Review, 2000-2001, Geneva, Switzerland: United Nations Publications, 83-100.

National Institute of Standards and Technology. 1992. Voluntary Products Standard PS 2-92 Performance Standard for wood-base structural-use panels. United States Department of Commerce, Guithersburg, Maryland.

Lang, E., and M.P. Wolcott. 1996. A model for viscoelastic consolidation of wood-strand mats Part I: Structural characterization of the mat via Monte Carlo simulation. Wood Fiber Sci. 28(1):100-109.

Lee, N.J., and Q. Wu. 2002. In-plane dimensional stability of three-layer oriented strandboard. Wood Fiber Sci. 34(1): 77-95.

Lenth, C.A., and F.A. Kamke. 1996. Investigations of flakeboard mat consolidation. Part I. Characterization the cellular structure. Wood Fiber Sci. 28(2): 153-167.

Linville, Jeffrey D. 2000. The influence of a horizontal density distribution on moisture-related mechanical degradation on oriented strand composites. Master of science thesis, Department of Civil and Environmental Engineering, Washington State University, Pullman, WA.

Lu, C., and F. Lam. 2001. Random field representation of horizontal density distribution: I. partially oriented strandboard mat. Wood Fiber Sci. 33(3):437-449.

Lu, C., and F. Lam. 2001. Relationship between thickness swelling and mat structures in robot-formed flakeboard mats. Holz Roh Werkstoff 59:201-210.

Oudjehane, A., and F. Lam. 1998. On the density profile within random and oriented wood-based composite panels: horizontal distribution. Composites part B 29B: 687-694.

Smith, C. D. 1982. Waferboard press closing strategies. Forest Prod. J. 32(3):40-45.

Smulski, Stephen. 1997. Engineering Wood Products: A guide for specifiers, designers and users. PFS Research Foundation, Madison, Wisconsin.

Steiner, P.R., and C. Dai. 1993. Spatial structure of wood composites in relation to processing and performance characteristics: Part 1. Rationale for model development. Wood Sci. Technol. (28):45-51.

Suchsland, O. 1962. The density distribution in flakeboard. Q. Bull., Michigan Agric. Expt. Sta., Michigan State Univ. 45(1):104-121.

Suchsland, O., and H. Xu. 1989. A simulation of the horizontal density distribution in a flakeboard. Forest Prod. J. 39(5): 29-33.

Wu, Qinglin. 1999. In-plane dimensional stability of oriented strand panel: Effect of processing variables. Wood Fiber Sci. 31(1): 28-40.

Winistorfer, P.M., W.W. Jr. Moschler, S. Wang, E. DePaula, and B.L. Bledsoe. 2000. Fundamentals of vertical density profile formation in wood composites. Part 1. In-situ density measurement of consolidated process. Wood Fiber Sci. 32(2):209-219.

Wolcott, M.P., A. Bozo, and J.D. Linville. 2001. Spatial variation in wood composites. *In* Proc. Of the Ibero-American Forest Products Conference. Univ. Bio-Bio, Conception, Chile.

Wolcott, M.P., F.A. Kamke, and D.A. Dillard. 1990. Fundamentals of flakeboard manufacture: viscoelastic behavior of the wood component. Wood Fiber Sci. 22(4):345-361.

CHAPTER 2. USING DIRECT-CONTACT AND NON-CONTACT ULTRASONIC METHODS TO CHARACTERIZE THE STRUCTURAL PROPERTIES OF ORIENTED STRANDBOARD

2.1. INTRODUCTION

Mat layering and alignment of wood flakes are used to improve mechanical properties of the Oriented strandboard (OSB). The mat formation by depositing resin-coated flakes results in relatively loosely packed mats. Although mat density increases during hot pressing, the final product still contains a substantial volume of voids (Furuno et al. 1983). Understanding the void structure created by the interactions of raw material and mat formation parameters has many important implications for evolution of the optimal properties into a quality product. In particular, the presence of voids in OSB reduces its elastic moduli and affects its dimensional stability (Lenth and Kamke 1996, Wu 1999). Therefore, attention must be given to the void distribution and its effects on product performance.

Voids are strong scatters of elastic waves. Various nondestructive techniques have been used to quantify voids and their effects on panel properties in polymer composites (Judd and Wright 1978). Among these methods, ultrasonic transmission (UT) is the most generally useful technique at present (Chen and Beall 2000, Vun et al. 2000, Jeong 1997, Jeong and Hsu 1995). The method involves transmitting a short pulse of ultrasonic energy through the specimen, measuring the attenuation caused by passage through the material, and defining

the maximum acceptable void content in terms of ultrasonic attenuation (Judd and Wright 1978). This method has an advantage over conventional approaches in that it can be used to assess the whole panel rather than only a small portion.

The need for application of nondestructive evaluation (NDE) technologies to improve the understanding of material characteristics (i.e., defects, basic properties, geometry, bonding quality, etc.) for wood composites has been overwhelmingly driven from technology push to market pull (Beall 1996a, Han and Bender 1991). However, effective application of the technologies in the necessary operating conditions with reasonable accuracy should be supported with knowledge of material responses obtained from system calibration. In studying wood composites, the NDE is beset with intrinsic material problems such as high attenuation and dispersion, anisotropy, growth properties, and heterogeneity of boundaries (Beall 1996b, Bucur et al. 1998). In addition, the coupling of transducers to wood-based materials in the direct-contact (DC) system presents the greatest source of variability and the major impediment to on-line implementation of NDE in process control of wood-based manufacturing (Ermolov 1998). The factors that affect coupling efficiency include acoustic impedance match of the transducers to the substrate, type of couplants between the transducer and the substrate, and characteristic of the substrate. Thus, the success of UT techniques depends largely on the couplant types, such as grease/gel couplants, adhesives, elastomerics, or air, and the coupling process.

With the advent of high transduction transducers used in non-contact (NC) ultrasonics, the exorbitant acoustic impedance barriers between air and most materials can be resolved (Bhardwaj 1997). This has resulted in a more sensitive NC air-coupling than the gel-coupling technique. Ultrasound technologies have been widely used today as compared to X-ray and γ-ray methods because of their cost-effectiveness, portability, non-hazardousness, and applicability to all states except plasma and vacuum of matters (Bhardwaj et al. 2000).

For a proper application of the UT techniques in a complex wood composite such as OSB, the effect of void content as influenced by board density on ultrasonic responses and panel properties needs to be investigated. The specific objectives of this work were (1) to investigate the feasibility of using DC and NC ultrasonic systems for measuring OSB properties as influenced by panel density, flake alignment level, and layering structures; and (2) to establish relationships among the processing variables that determine the material behavior of the boards and UT parameters such that calibration models can be developed for both ultrasonic systems.

2.2. EXPERIMENTAL PROCEDURES

2.2.1. Specimen Preparation

Using aspen (*Populus tremuloides*) flakes and liquid phenol-formaldehyde resin, single- and three-layer OSB panels were fabricated for the study (Wu 1999, Lee and Wu 2002). Panels in each type were made with 0.5% wax at the 4% RC level (based on ovendry weight of the wood flakes) in two replicates. The single-

layer boards had four nominal densities (ND) at 450, 650, 850, and 1150 kg/m^3, and three alignment levels. The three-layer boards had four shelling ratios (represented by face weight ratio (FWR) between the face layers and the entire panel), and two alignment levels. The single-layer panels (610x610x13 mm) were prepressed to thickness prior to heating of the mats for resin curing at 190^{o}C for 6 min. The three-layer panels (610x610x13 mm) were made with a conventional pressing procedure (one minute closing and 6 minutes pressing time at 190^{o}C). After hot pressing, the panels were conditioned and edge-trimmed. From the machine direction of the panel faces, the panel flake alignment level was quantified by

$$\text{Alignment \%} = (45-\theta)/45\ \% \qquad \textbf{(2.1)}$$

where $\theta = \sum |\text{measured angle}| / n$, given the n measurements (Geimer 1979, Harris and Johnson 1982). The flake alignment level was classified into three categories: (1) high alignment level (HAL), which ranged from 76 to 85%, (2) low alignment level (LAL), from 56 to 59%, and (3) random alignment level (RAL), from 22 to 29%. Ten base specimens (51x51x13 mm) were randomly selected and cut from each panel replicate, giving a total of twenty samples at each condition. The major flake alignment direction of the panel was marked on the top surface of each sample. Prior to the UT testing, the specimens were conditioned at 24^{o}C and 65% relative humidity (reaching an average equilibrium moisture content of 7.2% for all panels) and their density values measured. Thereafter, the specimens were destructively evaluated for the mechanical properties.

2.2.2. Direct-Contact Transmission

Direct-contact UT measurements were taken in a through-transmission mode with two Panametrics 100-kHz transducers – coupled on each opposite surface of the specimen using silicon gel (**Fig. 2.1a**) under a constant pressure of 3-kg weight. A Panametrics 5058 Pulser/Receiver was used to generate a 400-volt impulse that excites one transmitting transducer, and the other transducer captures the transmitted signal. Equipment calibration settings, including gain, damping, pulse height, pulser gain, and attenuator, were selected to cover the whole density range of the specimens tested. With a consistent setting of 40-60 dB gain or 0-80 dB attenuator, 30-dB preamplified signals were sampled at a rate of 5 MHz and the signals were digitized by a GageScope 8-bit CS225 card and processed by a signal processing software.

Velocity, impedance, attenuation, and root mean square (RMS) voltage of the DC ultrasound parameters were used to characterize the properties of the OSB (Vun 1998). The transverse shear velocity, V (km/s), is a ratio of the ultrasonic path length (i.e., through-thickness) and signal transit time to travel through the material, as given by

$$V = d / t \qquad \textbf{(2.2)}$$

where d is the sample thickness (mm) and t is the signal transit time (μs) across the thickness.

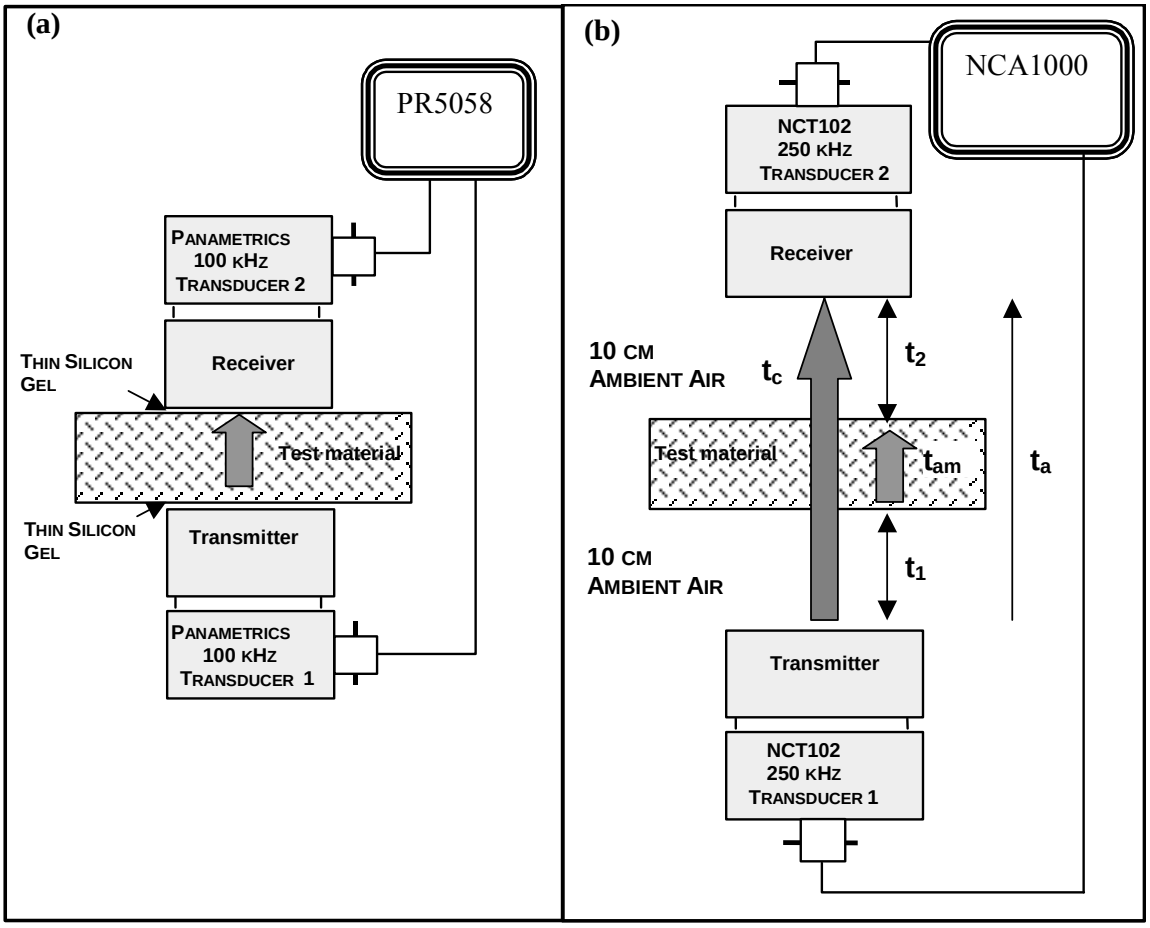

Fig. 2.1. Experimental setup for direct-contact (a) and non-contact (b) ultrasonic systems.

The acoustic impedance, Z ($Ggs^{-1}m^{-2}$), is calculated as

$$Z = V \bullet \rho \qquad \textbf{(2.3)}$$

where ρ is the sample average density (g/cm^3). The impedance of the material determines the alternating current of stress waves that flow through the material. As an analogy to a given alternating current potential difference (Benson 1991), the impedance of the ultrasonic current is affected by density difference in the sample. Attenuation, A (dB), is defined by

$$A = 20Log(A_m / A_{ref}) \quad \textbf{(2.4)}$$

where A_m is the peak amplitude (v), and A_{ref} is the maximum amplitude allowable by the system (i.e., 5.2 v). Attenuation is the energy loss associated with a decrease in the wave amplitude scattered by discontinuity and absorption among the different densities. The RMS voltage represents acquired signal intensity (Beauchamp and Yuen 1979). It is measured on a linear voltage scale and computed by time-averaging rectification as

$$RMS = \left(\frac{1}{\Delta t} \int v^2(t) dt \right)^{½} \quad \textbf{(2.5)}$$

where Δt is the time interval (μs) and v is the voltage (v).

2.2.3. Non-Contact Transmission

A SecondWave NCA1000-2E, non-contact ultrasonic system equipped with two 250-kHz, 25-mm NCT102 transducers was used for the NC through-thickness measurements (**Fig. 2.1b**). The system uses a deconvolved-chirp specially synthesized to characterize the acoustic impedance of the piezoelectric matching layer, which generates a high air-transduction necessary for NC ultrasound propagation in test materials (Bhardwaj et al. 2000).

The system computes sample thickness and ultrasound velocity, defined by

$$d_m = V_a * t_{am} = V_a * [t_a - (t_1 + t_2)/2] \quad \textbf{(2.6)}$$

$$V_m = \frac{d_m}{[t_{am} - (t_a - t_c)]} \quad \textbf{(2.7)}$$

where V_m is the ultrasound velocity through the test material (m/s), V_a is the reference ultrasound velocity in air (m/s), d_m is the material thickness (m), t_{am} is the time of flight (ToF) in air relative to material thickness (s), t_a is the ToF of direct transmission in the air column (s), t_1 is the reflected round trip ToF from transducer 1 to the bottom surface of the material (s), t_2 is the reflected round trip ToF from transducer 2 to the top surface of the material (s), and t_c is the ToF through air column when material is in between transducer 1 and transducer 2 (**Fig. 2.1b**).

The attenuation energy is determined by the integrated response (IR). IR (dB) is the net power of the actual ultrasound energy transmitted through the material as evaluated by

$$IR_m = IR_a - IR_c \qquad \textbf{(2.8)}$$

where IR_m is the integrated response of the peak energy transmitted in the material, IR_a is the IR in air, and IR_c is the IR in air when the material is in between the transducers. Being frequency independent, IR is basically related to the transmission coefficient (T) that measures how ultrasound is transmitted from one medium to another, given by

$$T = \frac{Z_1 Z_2}{(Z_1 + Z_2)^2} \qquad \textbf{(2.9)}$$

where Z_1 and Z_2 are the acoustic impedance of ultrasonic propagation in medium 1 and medium 2, respectively. IR_m is related to T as

$$IR_m = 20Log(T) \qquad \textbf{(2.10)}$$

The variable IR_m provides information on internal material quality such as degree of bonding, nature of the microstructure and texture, absence or presence of phases, and type of inclusions in the material (Bhardwaj 1997; Bhardwaj et al. 2000).

The UT measurement with the NCA1000 analyzer was done as follows. After the transducers were aligned, the equipment was calibrated to a known air ultrasound velocity of 344-346 m/s and a reference specimen, a 25.4 mm transparent polystyrene having 21.75 μs round trip ToF and 2320 m/s material velocity under ambient conditions. From the first peak analysis, gates were created forming four ultrasonic paths of propagation. These paths were P1: transducer 1 to transducer 2, P2: transducer 1 to material bottom surface reflection, P3: transducer 2 to material top surface reflection, and P4: transducer 2 to transducer 1. Then, based on the reference velocity and thickness, the velocity, thickness, and ToF of the test materials were computed and displayed.

2.2.4. Panel Density and Density Profile

Vertical (thickness direction) and horizontal (length or width directions) density profiles of each specimen were mapped using a Quintek Density Profiler (QDP-01X) after UT measurements. The maximum, average, and minimum densities along each direction were evaluated from the measured profiles for each sample.

2.2.5. Mechanical Properties

After UT and density measurements, each base specimen was ripped to obtain two *in-situ* 13x13x51 mm bending samples in the machine direction and a 13x25x51 mm internal bond (IB) sample for mechanical properties evaluation. All tests were conducted with a 4260 Instron machine according to the ASTM-D1037. The IB tests were done at a strain rate of 1 mm/min; whereas, the modulus of elasticity (MOE) and modulus of rupture (MOR) of each sample were measured with a 6 mm/min (0.24 in./min) loading rate. Each failed specimen was oven-dried to determine its moisture content at the testing time. IB (MPa), bending stiffness (E·I, MPa.cm^4), and breaking resistance (R·S, MPa.cm^3) were computed as:

$$IB = \frac{P}{bL} \quad \textbf{(2.11)}$$

$$E \bullet I = MOE\frac{bh^3}{12} \quad \textbf{(2.12)}$$

$$R \bullet S = MOR\frac{bh^2}{6} \quad \textbf{(2.13)}$$

where P is the peak load from the IB test (N), E is the MOE (MPa), I is the moment of inertia given by I=bh^3/12 (cm^4), R is the MOR (MPa), S is the section modulus given by S= bh^2/6 (cm^3), and *b, h,* and *L* are the width, height, and length (cm) of the specimen, respectively.

2.2.6. Statistical Analysis

SAS (2000) software was used to perform analysis of variance (ANOVA) with the Bonferoni adjustment for multiple comparisons of the class groups. The

measured ultrasonic parameters, density, and strength are segregated by resin content, flake alignment, board type (i.e., single layer versus three layers), and UT methods. A backward elimination option was used in the model selection procedure to evaluate the sensitivity of the variables to the high and low densities in both the vertical and horizontal directions. Scatter plots with the appropriate regressions (polynomial or power) were used to establish the correlations among density, strength properties, acoustic velocity, attenuation, and RMS.

2.3. RESULTS AND DISCUSSION

2.3.1. Density Profile and Basic Properties

Typical density profiles for the single- and three-layer boards are shown in **Fig. 2.2**. As expected, the single-layer boards had relatively uniform vertical density profiles with an overall density variation of ± 75 kg/m^3 about the mean. The uniform profile was attributed to the pre-pressing prior to mat heating during hot pressing (Wu 1999). For the single-layer panels (**Table 2.1**), the general trend of the mechanical properties is an increase with density at all flake alignment levels. MOE, MOR, and IB strength increased as the flake alignment level increased from low to high. The same trends were also observed with the DC velocity. For both methods, the UT velocity increased and UT attenuation decreased with an increase in sample density.

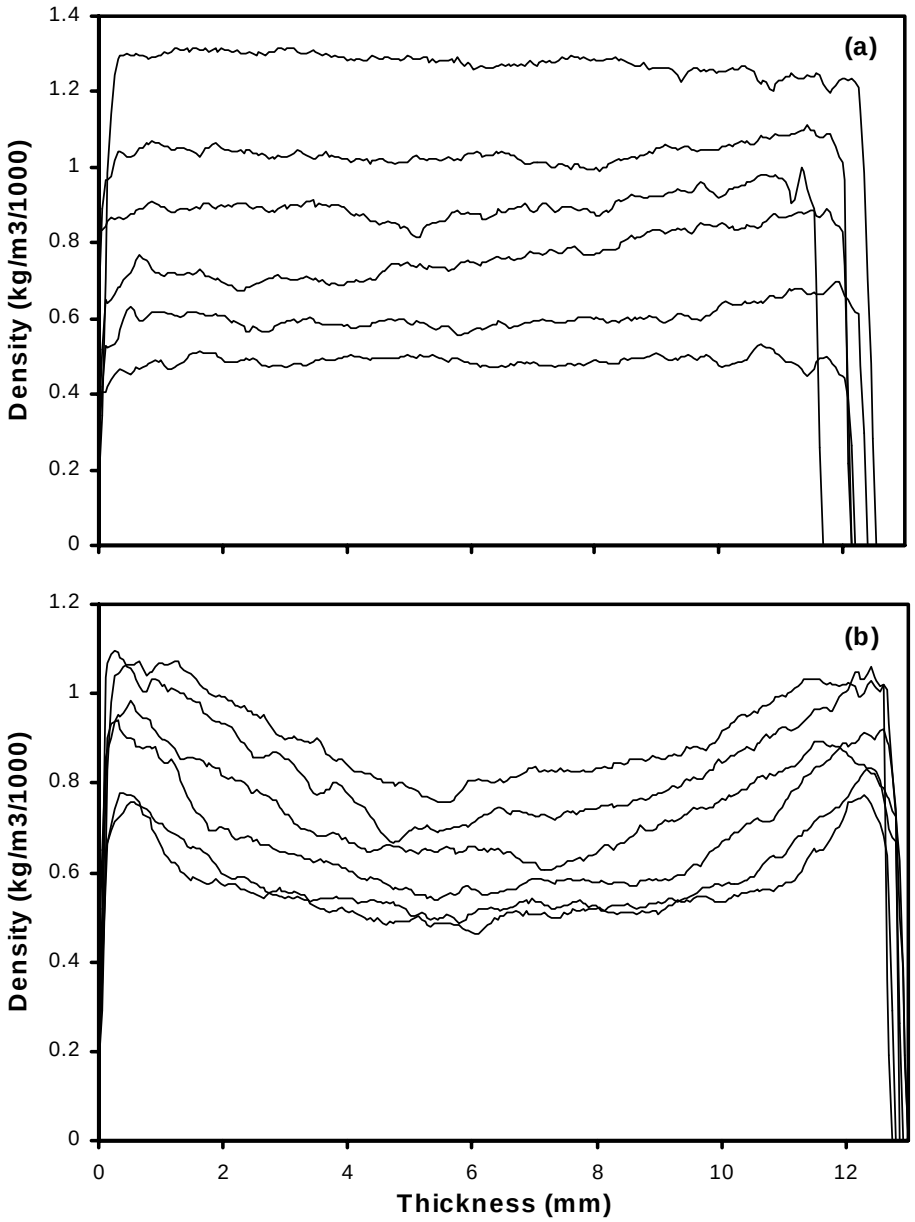

Fig. 2.2. Typical density profiles of single- (a) and three-layer (b) OSB boards used in the study.

Table 2.1. Mechanical and ultrasonic properties for the single-layer boards at the 4% RC level.

		Mechanical Properties[b]					Ultrasonic Properties[d]					
Board[c] Type	Density (kg/m^3)	MOR (MPa)	MOE (MPa)	RS ($MPa.cm^3$)	EI ($MPa.cm^4$)	IB (MPa)	DCV (m/s)	DCA (-dB)	DCR (v)	DCZ ($Mg/s.m^2$)	NCV (m/s)	NCA (-dB)
	594	30.4	243	9.9	51	0.64	810	28.25	0.31	481	610	83.0
	(5)[a]	(2.1)	(20)	(0.6)	(5)	(0.18)	(112)	(5.5)	(0.06)	(67)	(7)	(6.1)
	783	46.0	485	14.2	94	1.12	920	7.11	0.88	709	770	66.7
HAL	(79)	(6.3)	(133)	(2.0)	(26)	(0.18)	(61)	(6.0)	(0.28)	(127)	(66)	(2.2)
	1043	65.1	1056	21.2	213	1.43	1326	1.23	1.11	1222	905	71.3
	(41)	(5.6)	(214)	(2.2)	(46)	(0.05)	(160)	(0.4)	(0.07)	(375)	(83)	(4.1)
	1207	68.4	1296	23.0	275	1.47	1257	0.75	1.23	1426	1075	84.0
	(42)	(1.6)	(160)	(0.5)	(28)	(0.25)	(126)	(0.5)	(0.10)	(228)	(207)	(6.0)
	562	21.0	185	7.0	40	0.57	748	32.13	0.24	421	1046	87.8
	(22)	(1.5)	(12)	(0.7)	(3)	(0.12)	(32)	(7.5)	(0.11)	(22)	(364)	(5.0)
	808	41.4	447	12.9	87	0.85	847	2.30	1.00	684	693	68.7
LAL	(50)	(3.1)	(67)	(0.9)	(13)	(0.14)	(18)	(1.2)	(0.11)	(45)	(39)	(3.6)
	1013	56.7	961	18.1	190	1.16	1270	1.56	1.07	1288	853	79.3
	(55)	(8.0)	(196)	(3.0)	(43)	(0.12)	(47)	(1.7)	(0.17)	(113)	(77)	(2.6)
	1251	64.9	1213	20.3	237	1.28	1308	1.35	1.13	1636	1103	86.7
	(6)	(15)	(406)	(4.5)	(78)	(0.07)	(171)	(0.8)	(0.14)	(210)	(274)	(8.1)
	570	9.9	122	3.2	25	0.48	707	29.03	0.30	407	638	83.0
	(46)	(2.9)	(31)	(1.1)	(8)	(0.04)	(99)	(7.0)	(0.10)	(87)	(56)	(6.0)
RAL	817	30.1	376	9.1	71	1.13	919	3.74	1.01	752	724	72.5
	(57)	(5.7)	(77)	(1.7)	(14)	(0.08)	(108)	(3.5)	(0.17)	(123)	(75)	(3.1)
	925	36.0	509	12.0	106	1.02	950	3.75	0.92	882	721	73.3
	(84)	(8.8)	(264)	(2.6)	(49)	(0.24)	(54)	(2.5)	(0.14)	(125)	(51)	(3.1)

[a] Values in parenthesis are the Standard Deviation.
[b] MOR = Modulus of rupture (MPa), MOE = Modulus of elasticity (MPa), RS = Breaking resistance ($MPa.cm^3$), EI = Bending stiffness ($MPa.cm^4$), IB = Internal bonding strength (MPa).
[c] HAL =High alignment level ~80%, LAL = Low alignment level ~58%, RAL = Random alignment level ~26%.
[d] DC= Direct-Contact Method, NC= Non-Contact Method, -V = Velocity (m/s), -A = Attenuation (-dB), -R = Root Means Square (volt), -Z = Impedance (10^{-3} $Gg/(s.m^2)$).

For the three-layer boards, the U-shape density profiles (**Fig. 2.2b)** showed a high surface density and a low core density that led to an overall density variation of ± 144 kg/m^3 about the mean. From **Table 2.2**, the average MOR (29.4 MPa) of the three-layer panels was significantly lower than that of the single-layer panels (44.5 MPa, excluding the random panels). This was caused by the low-

density core layer in the three-layer panels. Both MOR and MOE values increase with increasing panel shelling ratio, particularly in the high alignment level. However, its effect on all ultrasonic variables in the three-layer panels was insignificant, an indication of invariant responses to the different thickness of the face and core layers. Also, the ultrasonic variables were not affected by differences in flake alignment levels for the boards.

Table 2.2. Mechanical and ultrasonic properties for the three-layer boards at 4% RC level.

FWR[a]	Density (kg/m^3)	Mechanical Properties				Ultrasonic Properties					
		MOR (MPa)	MOE (MPa)	RS (MPa $.cm^3$)	EI (MPa $.cm^4$)	DCV (m/s)	DCA (-dB)	DCR (v)	DCZ ($g/(s.m^2)$)	NCV (m/s)	NCA (-dB)
High Alignment Level											
0.3	744	26.5	395	9.0	87	701	4.26	0.93	518	571	79.0
	(48)	(3.0)	(23)	(1.3)	(2)	(90)	(4.3)	(0.19)	(41)	(27)	(4.9)
0.4	725	30.5	414	10.1	89	710	5.91	0.84	514	608	77.0
	(18)	(3.1)	(19)	(1.1)	(4)	(35)	(4.2)	(0.21)	(24)	(48)	(2.8)
0.5	751	31.0	489	10.3	105	719	0.91	1.18	539	615	78.8
	(43)	(2.5)	(48)	(0.8)	(10)	(24)	(0.7)	(0.10)	(21)	(22)	(3.8)
0.6	748	33.2	514	11.0	109	736	2.46	1.08	549	603	78.2
	(31)	(3.1)	(49)	(0.7)	(7)	(65)	(3.0)	(0.24)	(46)	(32)	(1.3)
Low Alignment Level											
0.3	718	26.9	413	9.5	96	753	6.52	0.91	542	652	78.8
	(46)	(3.3)	(56)	(1.3)	(14)	(60)	(8.7)	(0.37)	(75)	(38)	(2.9)
0.4	767	30.1	493	10.8	113	792	1.69	1.16	607	650	77.2
	(49)	(3.2)	(73)	(1.8)	(8)	(46)	(2.6)	(0.26)	(49)	(19)	(6.5)
0.5	722	28.1	421	9.8	95	747	8.16	0.83	540	653	79.2
	(82)	(6.7)	(117)	(2.2)	(25)	(53)	(11)	(0.30)	(78)	(77)	(2.6)
0.6	700	26.2	383	9.2	88	731	10.0	0.75	512	637	79.8
	(23)	(3.3)	(33)	(1.2)	(8)	(46)	(14)	(0.35)	(42)	(61)	(5.3)

[a] Flake weight ratio between the face layers and the entire panel.
Other notations are the same as shown in Table 1.

2.3.2. Velocity versus Density Correlation

The UT velocity in the single-layer boards (**Table 2.1**) was generally higher than that of the three-layer boards (**Table 2.2**) at a similar density. This was due to difference in the density profile and layering structure between the board types. With a wider density range (465-1400 kg/m^3), the single-layer panels had a higher correlation between the UT velocity and density than the three-layer panels (**Table 2.3**). The velocity from both methods responded poorly in the three-layer panels with a narrow density range (600-825 kg/m^3) among the boards.

The DC method had consistently higher velocity than the NC method (**Tables 2.1** and **2.2**) for a given board type. This was probably because of the impedance and frequency mismatch in the interface caused by pressurized gel coupling process as in the DC method. Such effects are absent in the NC method. The maximum amplitude of the transmitted wave occurs when the "acoustic impedances" of the media are matched. This kind of matching is required for a wave to be transmitted from one medium to another, for example, from liquid to solid (Benson 1991). This is consistent with observations made by Bhardwaj (1997) and Bhardwaj et al. (2000) that DC ultrasonic velocities are always higher when working with viscoelastic, cellular, and powder-compact materials – particularly when liquids or gels are used as couplants. Under the current setup, the NC system produced a maximum velocity of 1270 m/s, compared with 1670 m/s from the DC system for the same board type. The average impedance (a product of velocity and density) in the DC method had higher values than those

from the NC method. For both methods, the impedance was significantly affected by layering in the boards.

Table 2.3. Model for ultrasonic DC and NC properties and panel density at the combined alignment level. Model $Y = A + B\rho + C\rho^2 + D\rho^3 + \varepsilon$, where Y = Velocity, Attenuation or RMS and density ρ in kg/m^3. Parameters were evaluated by the backward elimination procedure at the 10% significance level.

UT [a] Parameter	Panel Type [b]	Regression Coefficient [c] (Combined Value[d]) A	B	C	D	R^2
Velocity (m/s)						
DC – Vel	1L4%RC	3909.46	-13.03615	1.67E-02	-6.42E-06	0.70
	3L4%RC	736.04	ns	ns	ns	0.00
NC – Vel	1L4%RC	511.55	ns	3.30E-04	ns	0.64
	3L4%RC	624.4	ns	ns	ns	0.00
Attenuation (-dB)						
DC-A	1L4%RC	251.23	-0.6785	6.08E-04	-1.80E-07	0.86
	3L4%RC	594.85	-1.5416	1.00E-03	ns	0.47
NC – A	1L4%RC	173.53	-0.23536	1.34E-04	ns	0.61
	3L4%RC	146.57	ns	-4.06E-04	3.80E-07	0.12
Root means square (volt)						
DC – RMS	1L4%RC	-2.46	0.006518	-2.93E-06	Ns	0.83
	3L4%RC	-4.41	ns	2.57E-05	-2.00E-08	0.37

[a] NC and DC denote non-contact and direct-contact methods, respectively.
[b] 1L and 3L denote one- and three-layer boards, and 4%RC denotes 4% resin content.
[c] ns denotes eliminated non-significant coefficients.
[d] Combined alignment and flake weight ratio for the 1L and 3L, respectively.

Fig. 2.3a shows a general nonlinear relationship between UT velocity and density. The regression curves between UT velocity and density (**Fig. 2.3**) showed the distinctive trends segregated by alignment levels for both methods. Particularly, the NC velocity models seemed effective in segregating the random, low, and high alignment levels in the high-density range. Meanwhile, the DC velocity models segregated the alignments well in the mid-density range. This observation suggested that both methods could produce a viable velocity-density model, if flake alignment parameter of the test material is known.

2.3.3. Attenuation/RMS versus Density Correlation

Typical non-linear attenuation- and RMS-density relationships in the single-layer panels are shown in **Fig. 2.3b**. The NC attenuation decreased as the density increased, and reached a minimum at about 900 kg/m^3 – so-called the "zero void" densification level for the OSB mat. Similarly, the DC attenuation decreased and the DC RMS voltage increased as the density increased. Both attenuation and RMS curves reached the minimum and maximum, respectively, at this density before leveling off. Both the minimum attenuation and maximum RMS voltage at this density signify the greatest transmissivity of the ultrasonic stress wave energy in the material. Above the 900 kg/m^3 density level, the NC attenuation increased as the density increased further. This indicates that wood-surface modification had occurred as a result of densification under high heat and pressure during hot pressing (Zavarin 1989). This density is the transition between the diminishing physical impediments of the interspatial voids in the lower density half and the increasing plastic-strain hardening densifications in the higher density half (Courtney 2000, Dowling 1998, Hertzberg 1996). Similar to those of single-layer panels, the three-layer panels had similar patterns of attenuation and RMS responses (**Fig. 2.4**).

For both panel types, the DC attenuation-density models had consistently higher R^2 values than the NC attenuation-density models (**Table 2.3**). The predicted DC attenuation and RMS were invariant to flake alignment changes. This indicated that the DC attenuation and DC RMS were effective in detecting

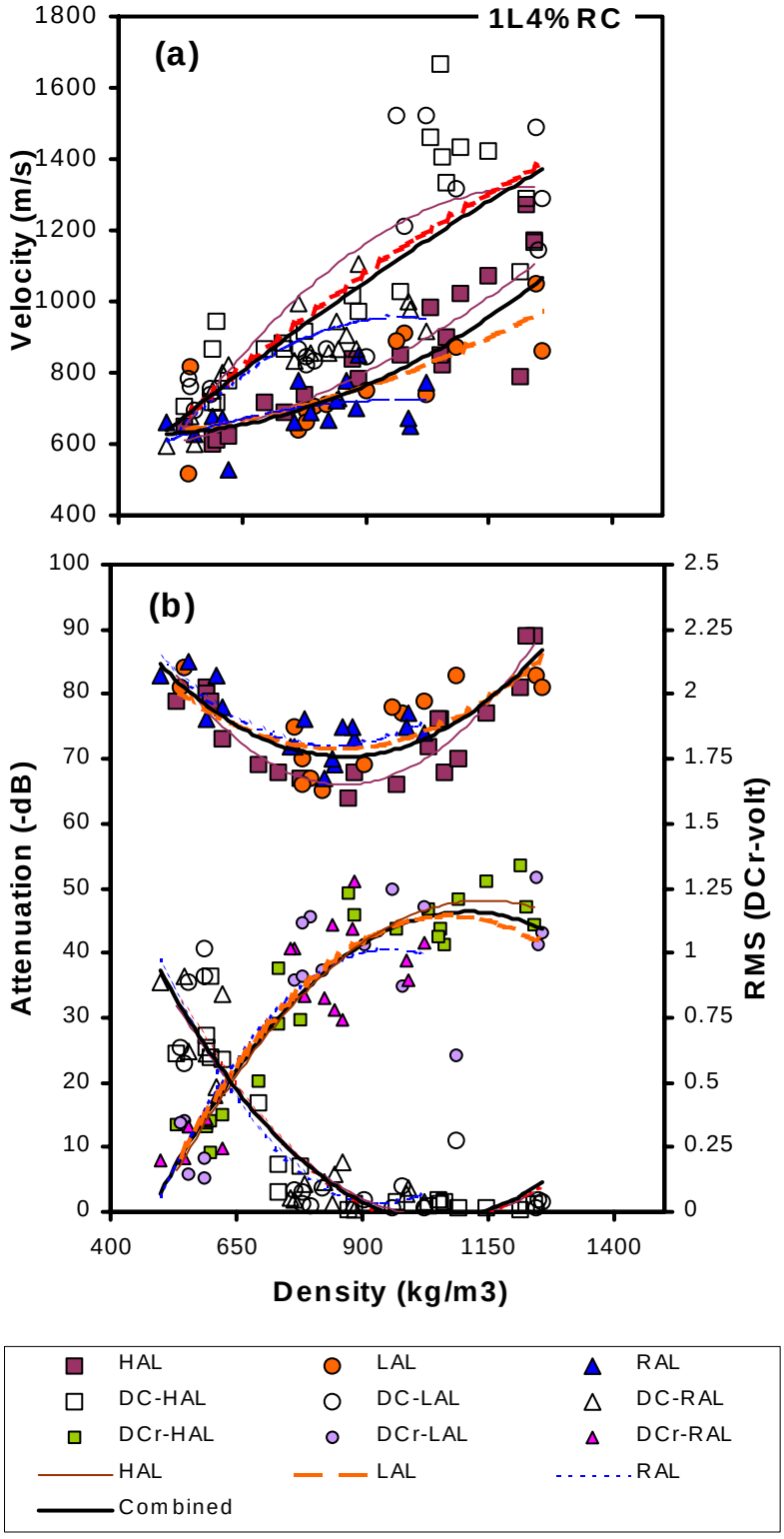

Fig. 2.3. Scatter plots of the UT variables velocity, attenuation, and RMS voltage (r) as a function of average panel density for 4% RC single-layer (1L) panels, segregated by DC and NC methods.

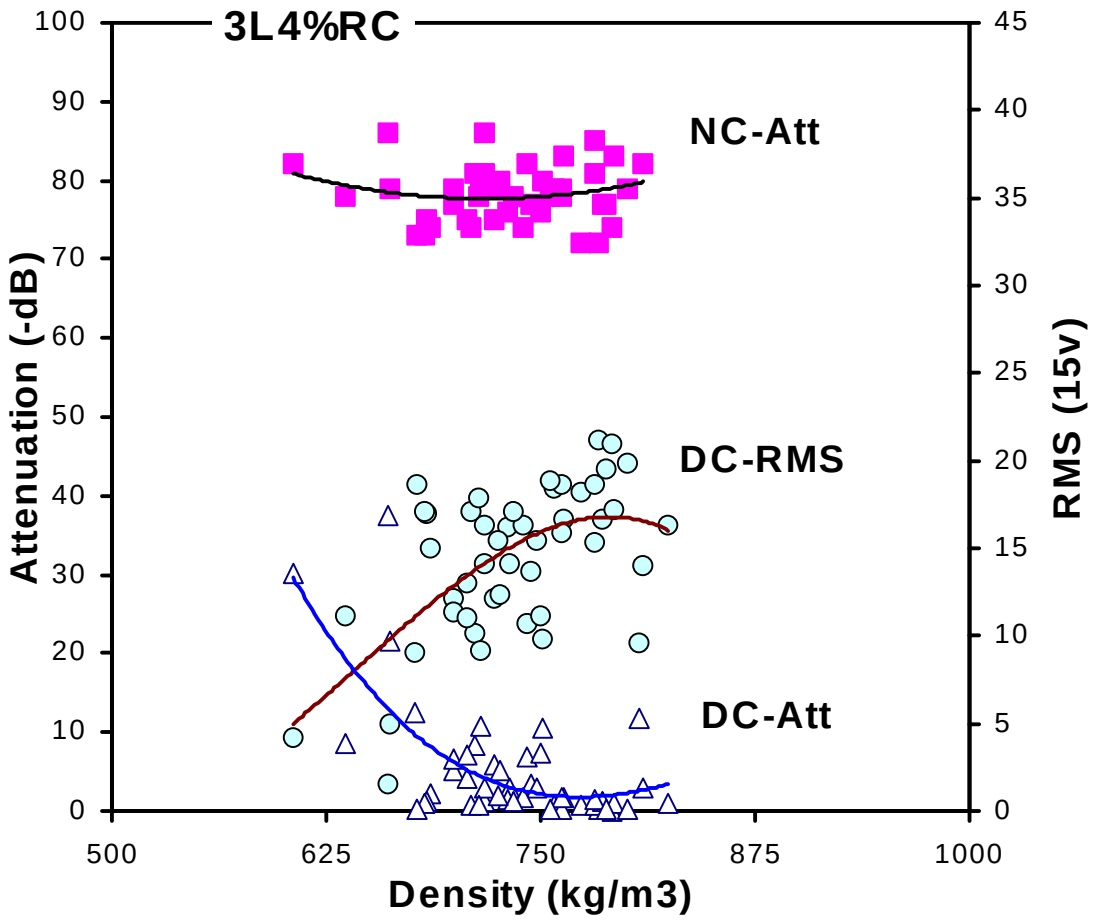

Fig. 2.4. Scatter plots of the DC and NC, attenuation (Att) and DC RMS voltage against density for combined shelling ratio in the three-layer (3L) panels at 4% RC level.

internal properties beyond physical impediments of interfacial boundary of the material. The DC attenuation models, approximately inverse of the DC RMS, showed a slightly better correlation ($R^2 = 0.86$) with density for 1L4%RC panels.

2.3.4. Strength versus Density Correlation

IB strength, bending stiffness (E·I), and breaking resistance (R·S) were highly correlated with average density for all panels (**Table 2.4**). **Fig. 2.5** shows that the strength-density models fitted well with the experimental data at various

alignment levels. Rising IB-density curves (combined alignment level) are seen in the panels. This shows a potential for IB improvement in the 1L4%RC panels by increasing resin content and/or density of the panel. Furthermore, a significant improvement of the IB strength can be realized by increasing alignment level from random to high (**Fig. 2.5** and **Table 2.1**) at a given density level.

Table 2.4. Parameters for the polynomial model between mechanical properties and density for the single-layer 4%RC panels [a].

Panel Alignment	Internal Bond Strength				Bending Stiffness				Breaking Resistance			
	A	B	C	R^2	A	B	C	R^2	A	B	C	R^2
Random	-0.000002	0.0044	-1.4204	0.76	0.0005	-0.5673	174.2	0.89	8E-06	0.0125	-6.5543	0.97
Low	-3E-08	0.0013	-0.1555	0.85	0.00008	0.1654	.82889	0.82	-0.00001	0.0463	-14.601	0.87
High	-0.000003	0.0073	-2.4965	0.88	0.0003	-0.1057	14.682	0.96	-0.00001	0.0467	-13.486	0.96
Combined	-0.000001	0.0037	-1.1138	0.78	0.0003	-0.1681	34.335	0.87	-2E-06	0.0283	-9.1633	0.79

[a] Model $Y = AX^2 + BX + C + \varepsilon$, where Y = internal bond (IB, MPa), bending stiffness (E.I., $MPa.cm^4$), or breaking resistance (R.S., $MPa.cm^3$), and X = average density (kg/m^3).

From **Table 2.4**, both E·I and R·S were highly correlated to the average sample density ($R^2 \geq 0.79$). The E·I-density correlations improved from random to high alignment boards. The increasing E·I slopes with alignments (**Fig. 2.5**) indicate that higher bending stiffness could be achieved with higher flake alignments regardless of density level. However, the R·S-density curves have similar slopes and different intercepts for the different alignment levels, indicating that the intrinsic material strength rather than the flake alignment influences the breaking ruptures for all panel types.

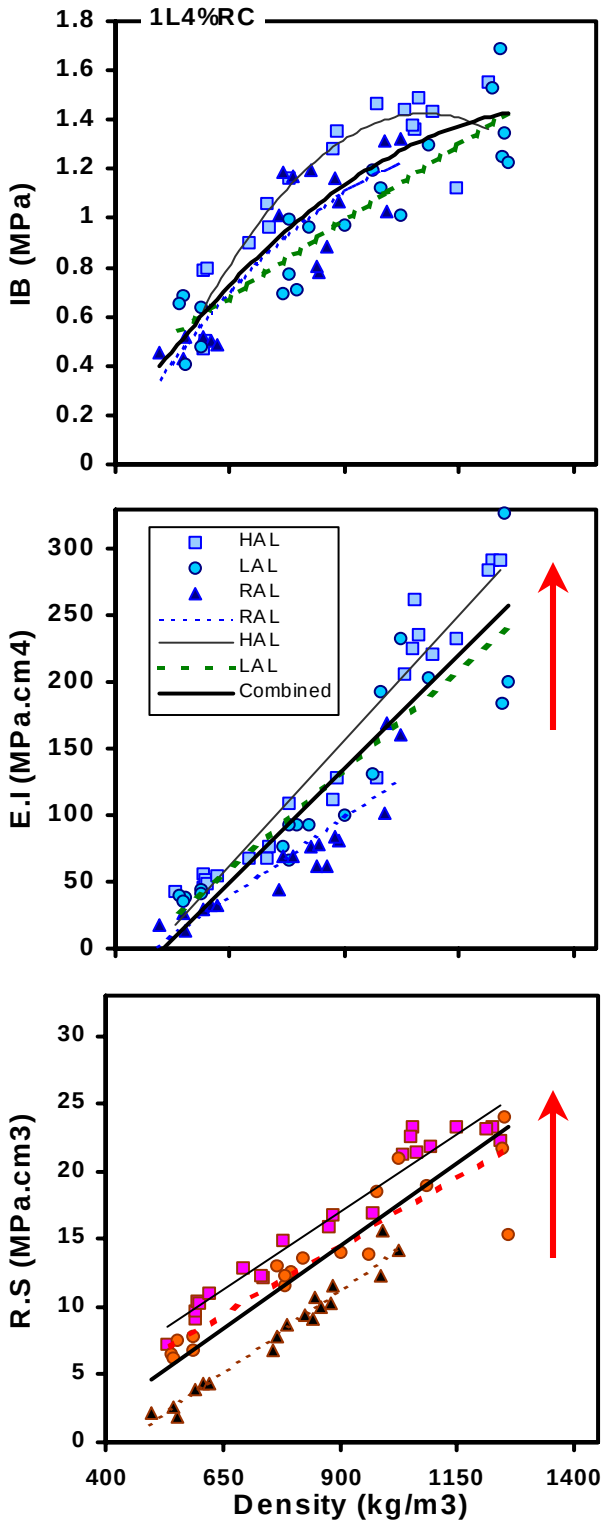

Fig. 2.5. Scatter plots of internal bond (IB), bending stiffness (E·I), and breaking resistance (R·S) versus density for 4% and 6% RC single-layer boards, segregated by high (HAL), low (LAL), and random (RAL) alignment levels.

2.3.5. Panel Strength versus UT Property Correlation

A quadratic polynomial regression was done to establish correlation between panel strength properties (i.e., IB, EI, and RS) and UT parameters (i.e., velocity, attenuation, and RMS). The model parameters are summarized in **Table 2.5**. The models plotted in **Figures 2.6** and **2.7** were well fitted with the experimental data. As shown in **Table 2.5**, all three strength properties correlated better to the DC parameters (velocity, attenuation, and RMS) as compared with the NC parameters. This indicates that strength prediction based on DC measurements would be more accurate than the NC measurements.

It can be seen from plots in **Fig. 2.6** that the relationships between the IB strength, EI, or RS and the UT velocity formed a similar trend as the strength-density relationship. There was a general linear relationship for velocity up to about 1250 m/s for both methods. Beyond that velocity, the DC curves leveled off significantly indicating that all strength properties became independent of the UT velocity in the density range. The flake alignment levels showed little effects on the relationship. There was also a similar general trend for the NC data.

All three mechanical properties (IB, EI, and RS) showed an increasing trend with DC RMS and a decreasing trend with DC attenuation (**Fig. 2.7**). The relationship is generally non-linear (**Table 2.5**). The mechanical properties showed an inconsistent trend with NC attenuation for boards at all flake alignment levels. Flake alignment levels, however, do not significantly affect the UT measurements from both DC and NC methods. Under the current NC settings,

Table 2.5. Parameters for panel strength and UT property models for the single-layer 4%RC boards [a].

Y	Align. Level	DC – Velocity (m/s)				NC – Velocity (m/s)				DC – Attenuation (dB)				NC – Attenuation (dB)				DC – RMS (v)			
		A	B	C	R^2	A	B	C	R^2	A	B	C	R^2	A	B	C	R^2	A	B	C	R^2
IB	Random	-2.E-06	0.0044	-1.6712	0.55	-6.E-06	0.0097	-3.1715	0.24	0.0006	-0.044	1.2006	0.81	-0.0033	0.4664	-15.394	0.45	-0.7664	1.8303	0.0329	0.79
	Low	-3.E-06	0.0065	-2.8514	0.88	-6.E-07	0.0022	-0.3998	0.63	-0.0002	-0.0077	1.0558	0.53	-0.0005	0.0888	-2.7437	0.12	-0.4449	1.1318	0.3565	0.53
	High	-2.E-06	0.0054	-2.1862	0.61	-4.E-06	0.0083	-2.9333	0.78	0.0005	-0.0436	1.4392	0.84	0.0031	-0.4798	19.323	0.24	-0.6341	1.8352	0.1276	0.84
	Combined	-2.E-06	0.0052	-2.1413	0.65	-2.E-06	0.0053	-1.6737	0.57	0.0004	-0.0342	1.2511	0.66	0.0017	-0.2628	11.105	0.06	-0.3256	1.218	0.2659	0.67
EI	Random	-2.E-04	0.5357	-246.76	0.46	-5.E-04	0.8508	-293.85	0.12	0.0712	-4.7309	101.12	0.49	-0.572	83.914	-2992.7	0.28	-105.22	223.64	-28.434	0.47
	Low	-7.E-04	1.7473	-886.85	0.79	-3.E-04	0.7144	-267.94	0.42	0.0417	-4.9312	162.35	0.34	-0.35	55.617	-2064.2	0.16	-92.287	245.65	-2.2581	0.34
	High	-4.E-04	1.1565	-615.66	0.77	-5.E-04	1.3426	-579.53	0.74	0.2998	-14.82	220.79	0.64	0.4091	-58.047	2188.7	0.18	118.97	14.777	31.077	0.68
	Combined	-3.E-04	0.831	-433.95	0.71	-1.E-04	0.6371	-287.61	0.61	0.1659	-9.6383	171.02	0.42	0.3457	-49.991	1909.7	0.07	74.356	41.141	22.96	0.45
RS	Random	-2.E-05	0.0581	-26.673	0.69	-2.E-05	0.0605	-21.69	0.23	0.0054	-0.4483	11.726	0.71	-0.0532	7.6543	-265.28	0.46	-10.586	23.827	-2.5095	0.70
	Low	-4.E-05	0.1064	-48.538	0.78	-1.E-06	0.0244	-3.752	0.42	0.0048	-0.4519	17.052	0.52	-0.024	3.696	-126.74	0.05	-5.4168	17.237	4.0763	0.52
	High	-2.E-05	0.0693	-30.055	0.87	-6.E-05	0.1256	-46.393	0.82	0.0181	-0.9359	21.279	0.77	0.0217	-3.206	134.26	0.06	3.6106	7.5363	6.8702	0.79
	Combined	-2.E-05	0.0687	-31.565	0.76	-3.E-05	0.0753	-28.095	0.58	0.0103	-0.6775	17.336	0.49	0.024	-3.6606	151.87	0.03	3.408	7.0564	4.6268	0.53

[a] Model $Y = AX^2 + BX + C + \varepsilon$, where Y = internal bond strength (IB, MPa), bending stiffness (E.I., MPa.cm^4), or breaking resistance (R.S., MPa.cm^3); X = Velocity (m/s), Attenuation (-dB), or RMS (v).

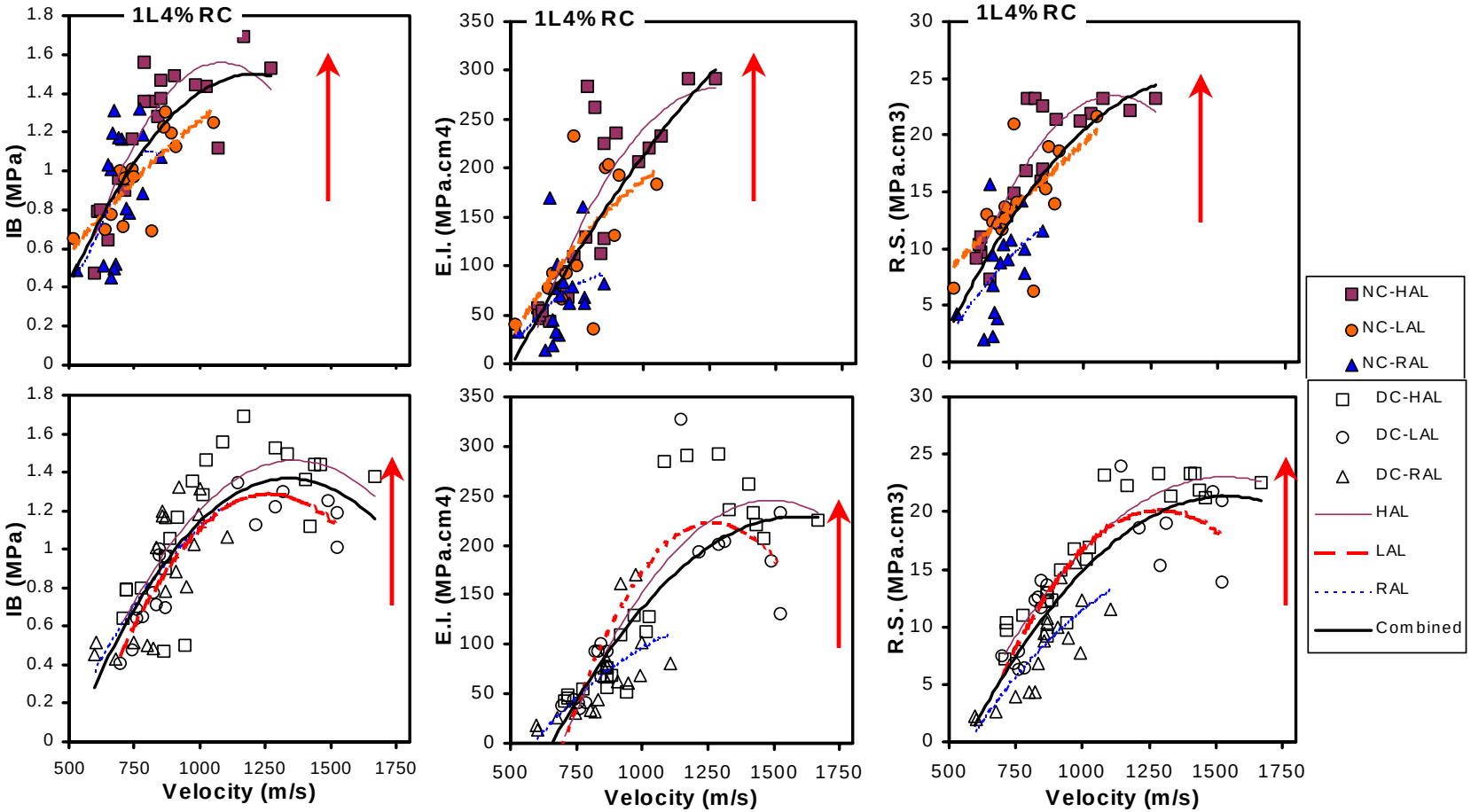

Fig. 2.6. Scatter plots of DC and NC velocities versus IB, E.I. and R.S. for 4% RC boards, segregated by high (HAL), low (LAL), and random (RAL) alignment levels.

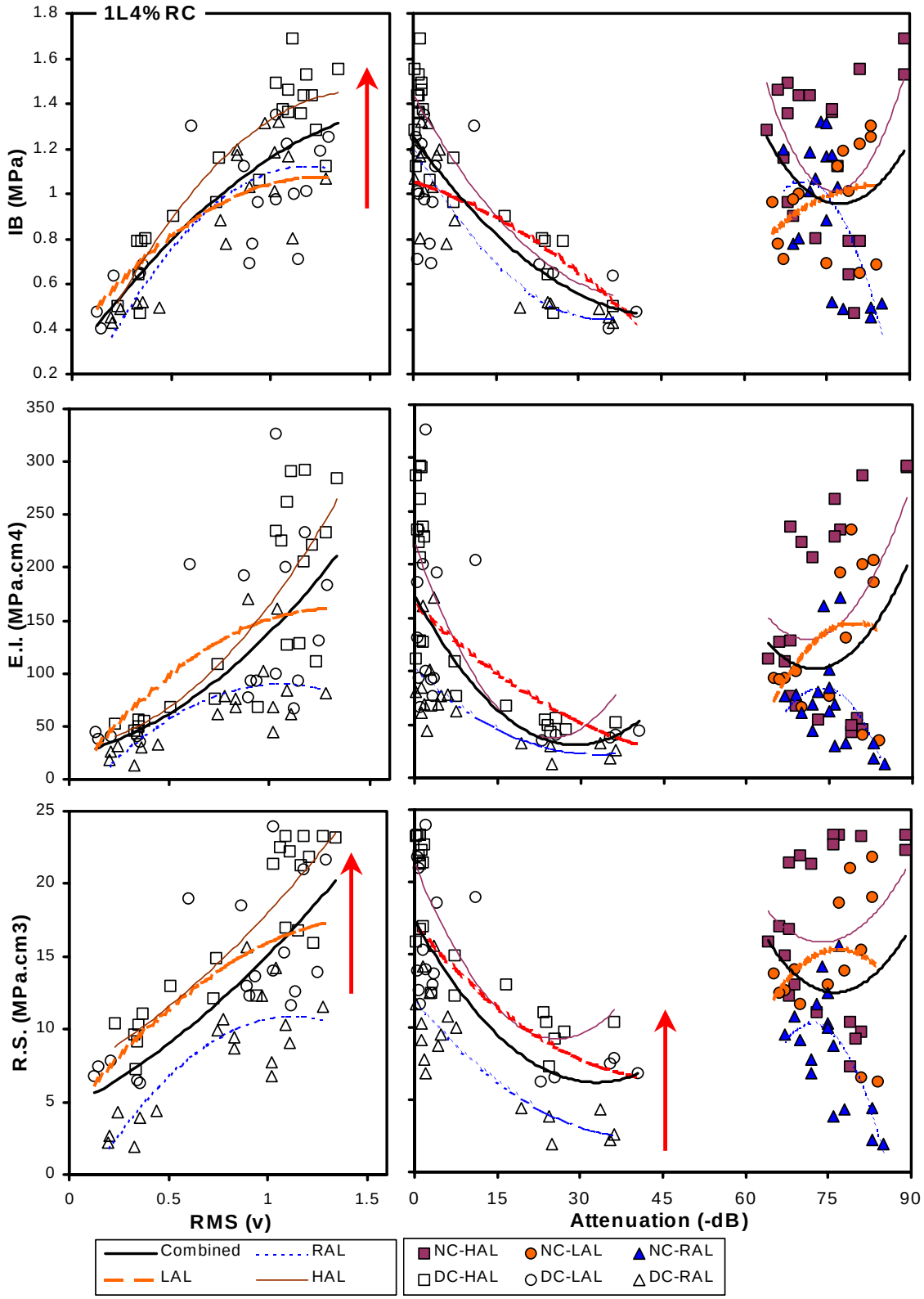

Fig. 2.7. Scatter plots of NC-attenuation, DC-RMS and DC-attenuation versus IB, E.I. and R.S. for single-layer, 4% RC boards, segregated by high (HAL), low (LAL), and random (RAL) alignment levels.

strength prediction based on NC attenuation needs further calibration for OSB products. For the three layer boards, the NC attenuation showed invariant responses to the panel shelling ratio (FWR as in **Table 2.2**). However, the DC attenuation had a minimum value at FWR=0.5 for the high alignment boards; whereas, the DC RMS had a maximum value.

2.3.6. UT Parameter versus Panel Property Interactions

Table 2.6 shows the results of the sensitivity analysis using the backward elimination procedure that indicate the significance of the interactions between the panel properties and UT parameters to the alignment levels. These interactions were segregated by the high and low density values in the thickness and horizontal planes of each sample. The average density was found to be strongly correlated to both the high and low densities in the thickness direction. The low density in both planes significantly affected the bending stiffness of the high alignment panels. This implied that the high stress concentration was formed in the low density ranges, leading to bending fracture and reducing stiffness. The high density in both planes has significant effect on breaking resistance of the high alignment panels.

Velocity, in general, was significantly restrained by the low-density points in the thickness direction, especially for the high alignment panels. Velocity was also significantly dependent on the high-density area in the horizontal plane for its transmission in the material. Particularly, the low-vertical and high-horizontal densities restrained the velocity transmission as in the NC method. This suggests that the high-alignment in the horizontal density facilitated the tortuosity of

Table 2.6. Sensitivity test (in p-values) using the backward elimination procedure to evaluate levels of interactions and influences among the structural properties and UT parameters in the high and low densities areas along the thickness and horizontal planes for 4% RC panels.

Variables	Alignment Level	Vertical-Thickness		Horizontal-plane	
		Density High	Density Low	Density High	Density Low
Stiffness (E.I.)	Combined	0.0929	NS	NS	0.0001
	Random	NS	NS	NS	0.0001
	Low	NS	NS	NS	0.0001
	High	NS	0.0001	NS	NS
Breaking (R.S.)	Combined	NS	NS	NS	0.0001
	Random	0.0001	NS	NS	NS
	Low	NS	NS	NS	0.0001
	High	NS	NS	0.0001	NS
Ave_Density	Combined	0.0001	0.0001	NS	0.0018
	Random	0.0001	0.002	NS	NS
	Low	0.0036	0.0001	NS	0.0401
	High	0.017	0.0413	0.0012	0.0099
DC_Velocity	Combined	NS	0.0001	NS	NS
	Random	0.0001	NS	NS	NS
	Low	0.018	NS	0.001	NS
	High	NS	0.0001	NS	NS
DC_Attenuation	Combined	0.0022	0.0005	0.01	NS
	Random	NS	0.0001	NS	0.0156
	Low	0.0003	0.0038	NS	NS
	High	NS	NS	0.0001	NS
DC_RMS	Combined	0.0058	0.0161	0.0722	NS
	Random	NS	0.0001	NS	NS
	Low	0.0036	0.038	NS	NS
	High	NS	NS	0.0001	NS
NC_Velocity	Combined	NS	0.0001	0.0132	NS
	Random	NS	0.0397	NS	NS
	Low	NS	NS	0.0016	NS
	High	NS	0.0001	NS	NS
NC_Attenuation	Combined	0.0012	0.0001	0.0958	NS
	Random	0.0006	NS	NS	0.0098
	Low	0.0001	0.0001	NS	NS
	High	NS	0.0088	0.0105	NS

NS denotes insignificant p-values of greater than 0.10 level.

velocity flux through the material, taking the meandering paths hindered by bottle-necking of the low density in the thickness direction. It appeared to present a "path of the least resistance" for the ultrasonic wave propagation regardless of the

original direction of the wave (also observed by Dickens et al. 1996). The DC attenuation and RMS behaved in a similar manner. The energy loss in attenuation for both methods was caused by reflections along the high- and low-density boundaries in the thickness direction, and by lateral scattering along the horizontal density plane.

2.4. CONCLUSIONS

Through-thickness DC and NC ultrasonic transmission responses were used successfully to characterize OSB's basic properties as influenced by processing variables. All UT responses in relation to the sample density were distributed nonlinearly. DC velocity was higher than the NC velocity, presumably because of the transducer or liquid couplant compression effects in the DC method and the agglomeration of the surfaces as affected by heat and pressure treatments. Generally good models in the single-layer boards were attributed to the nature of the internal structure defined by the uniform density profile and the larger density range. The ultrasonic measurements were not affected by the different panel shelling ratios for the three-layer boards.

The unique responses of the DC velocity and both the DC and NC attenuation approaching the inflection (minimum) at density (900 kg/m^3) level indicated the greatest transmissivity of the stress wave energy, a point of zero-void densification level. This is due to the diminishing effects of the physical voids in the low density and the strain hardening in the high density. The strength properties of the boards generally increased with density and flake alignment

levels. Viable density models devised in either method were board-specific. Attenuation and RMS were an effective predictor of density if flake alignment level was not known; otherwise, velocity could be used.

Density–strength correlations were high for all board types. The bending stiffness correlated highly to the low density in both thickness and horizontal directions; whereas, the breaking resistance correlated well to the high density. For both methods, velocity is significantly dependent on the low thickness density; whereas, the attenuation/RMS was significantly affected by high and low density boundaries in the thickness direction. The high correlations in both UT–strength and UT–density relationships indicated that UT techniques can provide a quick effective assessment of OSB's internal characteristics.

Although the NC system does provide a convenient remote measurement, we recommend that the instrumentation setup and UT calibration considerations need to match the natural frequency of the test material. With a proper calibration technique, the ultrasonic method is an effective tool for wood composite research and for on-line quality monitoring in fiber-based facilities.

2.5. REFERENCES

American Society for Testing and Materials (ASTM). 1996. Annual Book of ASTM Standard D1037-96, American Society for Testing and Materials, Philadelphia, PA.

Beall, C. F. 1996a. Application of ultrasonic technology to wood and wood-based materials. *In* Ferenc Divos, ed. Proc. 2nd University of Western Hungary International Conference on the Wood Science/Technology and Forestry. Sopron, Hungary.

Beall, C. F. 1996b. Future of nondestructive evaluation of wood and wood-based materials. Keynote pages 409-413 *in* Proc. 10th International Conference on NDE of Civil Structures & Materials, Boulder, CO.

Beauchamp, K.G., and C.K. Yuen. 1979. Digital methods for signal analysis. George Allen & Unwin Ltd., Boston, MA.

Benson, H. 1991. University physics. John Wiley & Sons, New York, NY: 663-672, 926p.

Bhardwaj, M.C. 1997. Innovation in non-contact ultrasonic analysis: applications for hidden objects detection. Mat. Res. Innovation 1:188-196.

Bhardwaj, M.C., I. Neeson, and G. Stead. 2000. Introduction to contact-free ultrasonic characterization and analysis of consolidated materials. Technical report at the Application of Nondestructive Evaluation in Powder Metals Seminar. Iowa State Univ., Ames, IA: 13p.

Bucur, V., M.P. Ansell, C.Y. Barlow, J. Pritchard, S. Carros, and X. Deglise. 1998. Physical methods for characterizing wood composite panel products. Holzforschung 52(5):553-561.

Chen, L-H, and F.C. Beall. 2000. Monitoring bond strength development in particleboard during pressing, using acousto-ultrasonics. Wood Fiber Sci. 32(4): 466-477.

Zavarin, E. 1989. Surface chemistry. *In* pages 261-266 of Concise Encylopedia of Wood & Wood-based Materials, A.P. Schniewind, R.W. Cahn, M.B. Bever editors. Pergamon Press, Oxford.

Courtney, Thomas H. 2000. Mechanical behavior of materials, 2 ed. Mc Graw Hill, New York: 162-168.

Dickens, J.R., D.A. Bender, and D.E. Bray. 1996. A critical-angle ultrasonic technique for inspection of wood parallel-to-grain. Wood Fiber Sci. 28(3): 380-388.

Dowling, Norman E. 1998. Mechanical behavior of materials: engineering methods for deformation, fracture, and fatigue. Prentice Hall, New Jersey.

Ermolov, I.N. 1998. Major ultrasonic inspection problem. Russian Journal of Nondestructive Testing 34(1):35-37. Plenum Publishing, New York.

Furuno, T., C-Y Hse, and W.A Cote. 1983. Observation of microscopic factors affecting strength and dimensional properties of hardwood flakeboard. Pages 297-312 *in* T.M. Maloney, ed. Proc. 17th. Washington State University International Symposium on Particleboard-Composite Materials. Pullman, WA.

Geimer, R.L. 1979. Data basic to engineering design of reconstituted flakeboard. Pages 105-125 *in* T.M. Maloney, ed. Proc. 13th. Washington State University International Symposium on particleboard/composite materials. Pullman, WA.

Han, M-B, and D.A. Bender. 1991. Ultrasonic characteristics in solid and reconstituted wood. Paper No. 914541 in the 1991 International Winter Meeting, December 17-20, American Society of Agricultural Engineers, Chicago, Illinois.

Hertzberg, Richard W. 1996. Deformation and fracture mechanics of engineering materials. John Wiley & Sons, New York.

Jeong, H. 1997. Effects of voids on the mechanical strength and ultrasonics attenuation of laminated composites. Journal of Composite Materials 31(3): 276-292.

Jeong, H, and D.K. Hsu. 1995. Experimental analysis of porosity-induced ultrasonic attenuation and velocity change in carbon composites. Ultrasonics 33(3): 195-203.

Judd, N.C.W., and W.W. Wright. 1978. Voids and their effects on the mechanical properties of composites-An appraisal. SAMPE Journal, January/February: 10-14.

Lee, N.J., and Q. Wu. 2002. In-plane dimensional stability of three-layer oriented strandboard. Wood Fiber Sci. 34(1): 77-95.

Lenth, C.A., and F.A. Kamke. 1996. Investigations of flakeboard mat consolidation. Part I. Characterization the cellular structure. Wood Fiber Sci. 28(2): 153-167.

Sas Institute Inc. 2000. SAS User's guide version 8.0. SAS Institute Inc., Cary, NC.

Vun, R.Y, Q. Wu, M.C. Bhardwaj, and G. Stead. 2000. Through-thickness ultrasonic transmission properties of oriented strandboard. Pages 77-86 *in* Ferenc Divos, ed. Proc. 12th University of Western Hungary International Symposium on Nondestructive Testing of Wood. Sopron, Hungary.

Wu, Q. 1999. In-plane dimensional stability of oriented strand panel: Effect of processing variables. Wood Fiber Sci. 31(1): 28-40.

CHAPTER 3. DIRECT-CONTACT ULTRASONIC CHARACTERIZATION OF HORIZONTAL DENSITY VARIATIONS IN ORIENTED STRANDBOARD

3.1. INTRODUCTION

Strength properties of wood-based composites are related to the mean panel density and the density distribution (both in-plane and across panel thickness). In-plane or horizontal density variation in flakeboards is due to the location and presence of voids in the low density range and discrete consolidated particle structure in the high density range, created from the random particle deposition in the mat forming process (Suchsland 1962, Suchsland and Xu 1989, Vun et al. 2003). Process and raw material attributes, including strand type and geometry, amount of fines, and strand dimension and configuration, are the main factors contributing to the density variation. In-plane density variation is a precursor to crack formation and propagation during creep rupture of oriented strandboard (OSB), as noted by Vun and Beall (2002). The critical crack was initiated from the weakest point of the lowest density zones in the boards. The fracture was seen to propagate and follow the valleys of low-density zones. The magnitude of density variation, therefore, determines the creep resistance and durability properties of OSB.

The European EN300 standard for panel manufacturing requires the horizontal density distribution in a panel to be within ±10% variation of the average panel density (Kruse et al. 2000). Modeling for the spatial structure of

wood composites respective to processing and performance characteristics has been done using theoretical models and also by gravimetric destructive methods (Lu and Lam 2001, Oudjehane and Lam 1998, Steiner and Dai 1993). There is, however, lack of nondestructive techniques for determining the level of in-plane density variation in wood composites.

Nondestructive evaluation technologies have been utilized to study internal material properties such as defects and bonding quality for composite materials (Beall 2002, Bucur et al 1998). The available techniques include the forced vibration (Suddarth 1965), impact stress wave (Ross and Pellerin 1988, Vogt 1986), acousto-ultrasonics (Chen and Beall 2000), and acoustic emission (Vun and Beall 2002). Among these techniques, ultrasonic transmission (UT) is a test that involves transmission of ultrasonic pulses through a specimen and capture of the material response signatures (Jeong and Hsu 1995). Energy absorption and scatter of elastic waves due to discontinuities in interfacial boundaries result in an attenuated signal that characterizes the internal structure and material properties (Judd and Wright 1978). The advantage of being able to scan a relatively large sample area makes UT technique an appropriate and safe tool for studying the spatial variation of various material properties.

In an earlier study (Vun et al. 2003), direct-contact and non-contact techniques were applied to relate structural properties of OSB to such UT variables as velocity and attenuation. It was shown that the attenuation and root mean square (RMS) voltage variables are suitable as density predictors if the panel

flake alignment level is not known; otherwise, the velocity could be used. A "zero-void" densification point of OSB was identified by ultrasonic characterization, the distinguishing the diminishing effect of existence of macrovoids at the low density and the increasing plastic-strain hardening flow in the interfaces at high density ranges. The existence of reasonably good correlations among the UT parameters and the structural properties of OSB is an avenue for nondestructively predicting and examining spatial properties of the board.

In this study, horizontal density distributions in OSB were obtained using a direct-contact UT technique. Individual density values were measured on the respective scanning areas. The objectives were (1) to establish relationships between the UT variables and resin content (RC)/nominal density (ND) combinations; (2) to develop models for predicting UT variables from measured density; (3) to develop calibration models for predicting measured density from the UT variables; (4) to compare predicted values from various models to the control limits obtained using the EN300 standard; and (5) to map and compare the spatial distribution of predicted and measured densities.

This chapter discusses the descriptive statistics of the variables and their relationships to the RC and ND levels, the UT variable regressions on the average density, the density prediction models, and the validation of the predicted to measured average density by percent out-of-limits and spatial graphics. Recommendations for future research are also discussed.

3.2. EXPERIMENTAL PROCEDURES

3.2.1. Specimen Preparation

Loblolly pine (*P. taeda*) trees of about 46 cm in diameter were harvested from Lee Memorial Forest, located near Bogalusa, Louisiana. The logs were flat-sawn into about 25 mm thick boards. At the Louisiana Forest Products Development Center, the boards were flaked using a disc flaker to produce about 76 mm long flakes. The flakes were dried and screened. Eighteen random, single-layer (13x510x560 mm) OSB panels were manufactured using liquid phenol-formaldehyde resin. Each board was made with 0.5% wax at one of three resin contents (RC), either 2%, 4%, or 6%, and one of three nominal densities (ND), either 0.4, 0.6, or 0.8 g/cm^3; two replicates of each board type were made. The platens of 13x560x610 mm (0.5x22x24 in.) containing the blended mat were hot-pressed to thickness regulated by 13 mm thick iron stoppers. The mats were hot-pressed for 7 minutes at 190^{o}C under 4.44 MPa to cure the resin. After pressing, the boards were cooled to ambient conditions and then trimmed to reduce edge effects on test specimens. Each panel was conditioned at 24^{o}C and 60% relative humidity to reach equilibrium. A 10x9 grid was then drawn on each board (**Fig. 3.1b**). Ninety individual specimens were obtained from the grid and were UT measured. Each board was then sawn into 13x51x51 mm specimens for the Average Density (AD) measurements, in g/cm^3.

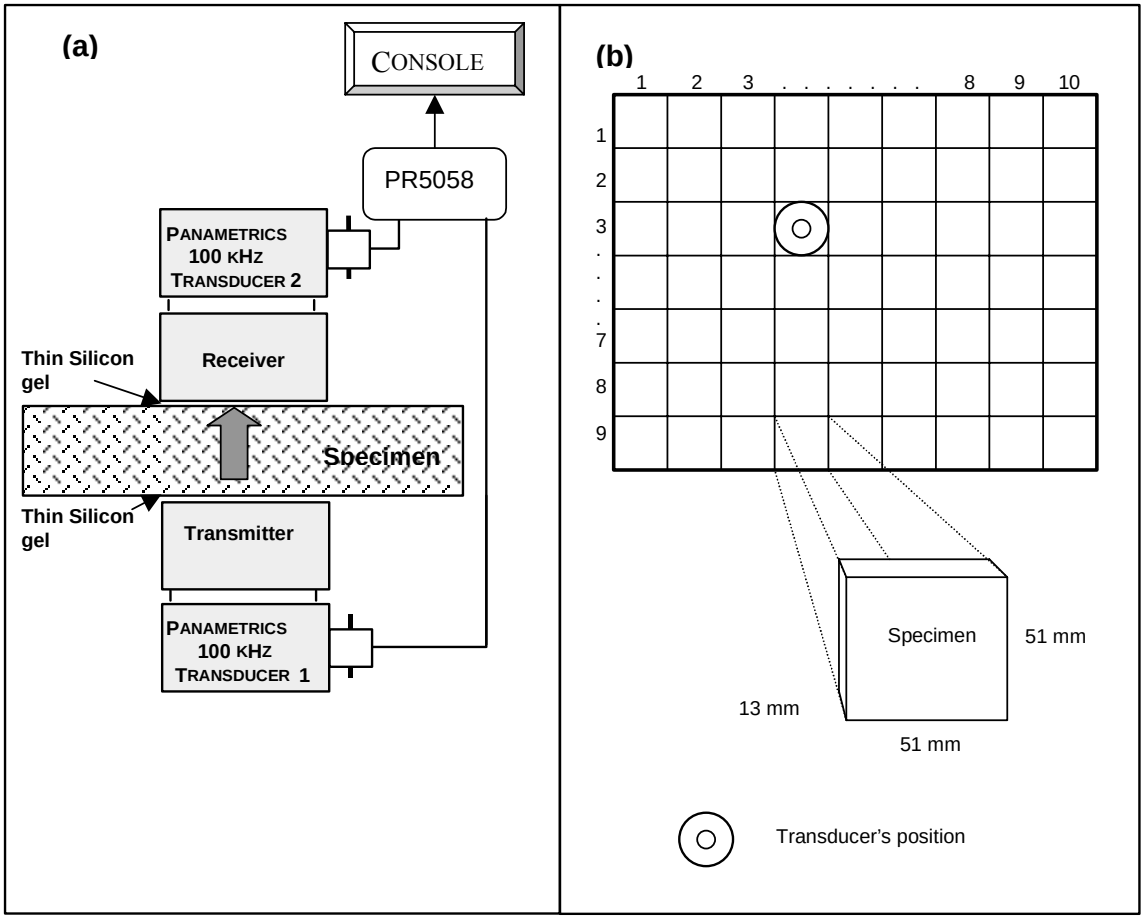

Fig. 3.1. Experimental setup for contact ultrasonic system (a) and test boards configuration (b).

3.2.2. Direct-Contact Transmission

UT measurements were taken in a through-transmission mode with two Panametrics 100-kHz transducers attached to opposite surfaces of the specimens (coupled using silicon gel) under a constant pressure of 3 kg weight. A Panametrics 5058 Pulser/Receiver was used to generate a 400-volt impulse that excited the transmitting transducer; the receiving transducer captured the transmitted signal (**Fig. 3.1a**). With a consistent setting of 40-60 dB gain or 0-80

dB attenuator, the signal was 30 dB preamplified, sampled at 5 MHz, digitized using a GageScope 8-bit CS225 card, and signal processed. Velocity, impedance, attenuation, and RMS voltage of the ultrasound variables were used to characterize the properties (Refer to Equations 2.2, 2.3, 2.4, and 2.5, respectively).

For each board, the basic direct contact UT measurements of velocity (km/s), attenuation (-dB), and RMS voltage were taken for each of the ninety specimens defined by the grid. From these three variables and AD, five other measurements were also obtained: impedance, attenuation corrected to thickness (AT), attenuation corrected to thickness and density (ATD), RMS voltage corrected to thickness (RT), and RMS voltage corrected to thickness and density (RTD).

3.2.3. Density Profile

Density profiles across thickness and width for each specimen were obtained using a Quintek X-ray Density Profiler (QDP-01X). For each panel, the maximum, average, and minimum densities for each of the ninety test specimens were determined.

3.2.4. Data

One of the two boards created at each RC/ND combination was randomly selected, giving a total of nine boards. The AD and UT measurements used in all of the analyses came from the 90•9= 810 specimens obtained from the nine boards that were selected.

3.3. RESULTS AND DISCUSSION

3.3.1. Average Density and UT Properties

In this section, we shall examine the descriptive statistics of panel and UT properties segregated by the nine RC/ND combinations (**Tables 3.1** and **3.2**). The coefficient of variation, or CV (defined as the sample standard deviation of the group divided by the average for the group, in percent) was calculated for each variable in these tables. For the variable AD, CV's decreased as ND levels increased for each RC level. This pattern of decreasing CV values as ND levels increased for each RC level was also observed for the UT variables velocity, impedance, and RMS voltage. The CV values for attenuation did not follow this pattern.

For each RC level, the vertical density profiles for the six specimens exhibited the typical M-shape of **Fig. 3.2** (two profiles of each ND were chosen to exhibit the variability within the ND, and also to demonstrate the basic nature of the profiles for that ND). Note that variability of the density profiles in the low density specimens is higher than those in the high density specimens. The low density specimens had smaller differential heat transfer from the surface to core during hot pressing, leading to a less pronounced dip and rise in the density profile. The high density specimens tended to have a sharper density contrast between face and core layers, since high-density elements at the surface decreased more rapidly following the exponential decreasing rate of differential heat transfer towards the core (Smith 1982). The conspicuous high-face and low-core density

layers can also be attributed to the elevated low-density areas in orthogonal flake boundaries (Lenth and Kamke 1996), causing physical hindrance to heat transfer necessarily for resin curing.

Table 3.1. Average values of the specimen mean densities and ultrasonic measurements.

Resin Content (%)	Nominal Density (g/cm^3)	Average Density (g/cm^3)	Ultrasonic variables				
			Z ($Gg/(s.m^2)$)	ATD ($dB.cm^3/mm.g$)	RTD ($v.cm^3/mm.g$)	AT (dB/mm)	RT (v/mm)
2%	0.40	0.476 (8)	0.331 (23)	3.288 (37)	0.046 (77)	1.552 (36)	0.022 (79)
	0.60	0.686 (7)	0.642 (17)	1.298 (40)	0.063 a (40)	0.890 (40)	0.043 (41)
	0.80	0.894 (4)	0.879 (12)	0.419 (68)	0.069 a (24)	0.371 (66)	0.062 (25)
4%	0.40	0.483 (7)	0.427 (48)	2.516 (30)	0.068 (167)	1.237 (26)	0.025 (69)
	0.60	0.691 (7)	0.810 (15)	0.463 (68)	0.080 b (34)	0.313 (65)	0.056 (36)
	0.80	0.887 (5)	1.008 (12)	0.184 (61)	0.086 b (88)	0.165 (58)	0.065 (24)
6%	0.40	0.479 (9)	0.450 (35)	1.910 (42)	0.053 (65)	0.900 (41)	0.026 (69)
	0.60	0.699 (5)	0.995 (10)	0.347 (76)	0.084 (24)	0.237 (71)	0.059 c (26)
	0.80	0.899 (4)	0.922 (7)	0.124 (76)	0.069 (20)	0.110 (73)	0.063 c (22)

For each RC level, reject Ho: $\mu_{.4}=\mu_{.6}=\mu_{.8}$ ($p < 0.01$ for $F(2, 267)$) for each UT variable.
a, b, c = p-value > 0.12 not significantly different by F(1, 267) test.
( ) = Coefficient of Variation (CV%) of 90 specimens within a board, rounded to nearest integer.
Z = Acoustic impedance ($Gg./(s.m^2)$).
AT = Attenuation coefficient (dB/mm) corrected for thickness.
RT = RMS coefficient (v/mm) corrected for thickness.
ATD = Attenuation coefficient ($dB.cm^3/mm.g$) corrected for density and thickness.
RTD = RMS coefficient ($v.cm^3/mm.g$) corrected for density and thickness.

Table 3.2. Comparisons of resin content (RC) and nominal density (ND) to ultrasonic measurements.

RC %	ND (g/cm^3)	LS Mean	CV (%)	P-VALUE *							
---- Velocity (km/s) ----------											
2	0.4	0.693	(21)	2; 0.4	<.0001	<.0001	<.0001			<.0001	
	0.6	0.936	(16)		2; 0.6	0.0342		<.0001			<.0001	
	0.8	0.985	(12)			2; 0.8			<.0001			0.0731
4	0.4	0.830	(30)	2%//4%	0.4	***	4; 0.4	<.0001	<.0001	<.0001		
	0.6	1.169	(12)		0.0032	0.6		4; 0.6	0.5597		<.0001	
	0.8	1.156	(19)			0.0561	0.8		4; 0.8			<.0001
6	0.4	0.924	(29)	2%	**			0.4	**	6; 0.4	<.0001	<.0001
	0.6	1.422	(8)	0.0114	4%			<.0001	0.6		6; 0.6	<.0001
	0.8	1.026	(7)	<.0001	<.0001	6%		<.0001	<.0001	0.8		6; 0.8
--- Attenuation (-dB) --------												
2	0.4	19.19	(36)	2; 0.4	<.0001	<.0001	<.0001			<.0001		
	0.6	10.83	(41)		2; 0.6	<.0001		<.0001			<.0001	
	0.8	4.49	(66)			2; 0.8			<.0001			<.0001
4	0.4	14.86	(29)				4; 0.4	<.0001	<.0001	<.0001		
	0.6	3.78	(65)					4; 0.6	0.0013		0.0816	
	0.8	2.02	(61)						4; 0.8			0.2341
6	0.4	10.79	(41)	2%	**			0.4	**	6; 0.4	<.0001	<.0001
	0.6	2.83	(72)	<.0001	4%			<.0001	0.6		6; 0.6	0.0077
	0.8	1.36	(72)	<.0001	<.0001	6%		<.0001	<.0001	0.8		6; 0.8
---- RMS-Voltage (v) --------												
2	0.4	0.272	(79)	2; 0.4	<.0001	<.0001	0.2783			0.1900		
	0.6	0.528	(41)		2; 0.6	<.0001		<.0001			<.0001	
	0.8	0.754	(25)			2; 0.8			0.1927			0.4609
4	0.4	0.305	(72)				4; 0.4	<.0001	<.0001	0.8207		
	0.6	0.672	(36)					4; 0.6	<.0001		0.3254	
	0.8	0.794	(30)						4; 0.8			0.5716
6	0.4	0.312	(69)	2%	**			0.4	**	6; 0.4	<.0001	<.0001
	0.6	0.702	(26)	0.0165	4%			0.0043	0.6		6; 0.6	0.0149
	0.8	0.777	(22)	0.0007	0.5486	6%		0.8457	0.0017	0.8		6; 0.8

( ) = Coefficient of Variation (CV%) of 90 specimens in a board, rounded to nearest integer.

* p-values for pairwise comparisons of the RC [ND] at each ND [RC] level using a two-factor analysis of variance with 801 error degrees of freedom.

** Within the bordered are p-values for pairwise F(2, 801) tests for RC curves and ND curves parallel.

*** F(1,801) test for part of RC 2% and 4% parallel.

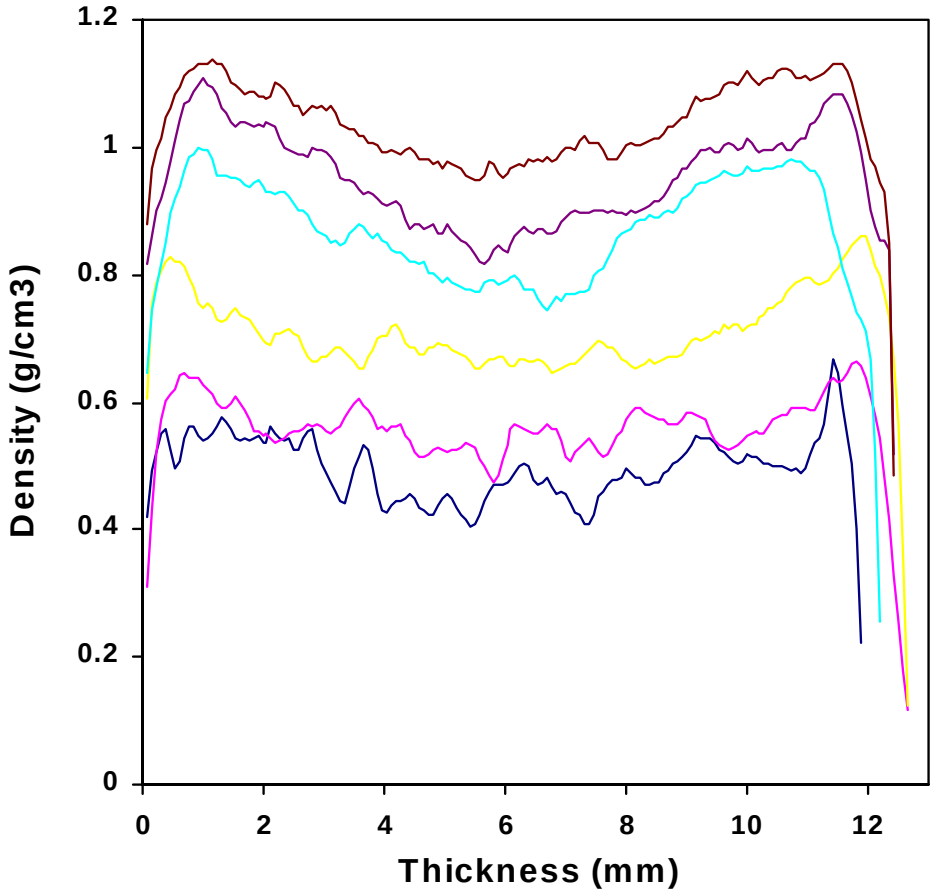

Fig. 3.2. Measured vertical density profiles representing the density range tested in the single-layer panel (Two profiles per nominal density – same basic shapes for all RC's).

The existence of a larger density fluctuation in the density profile for the low-density specimens led to higher attenuation, lower velocity, and lower RMS voltage values. This is consistent with the finding that the high attenuation and dispersion of the ultrasonic energy was caused by discontinuities arising from interfacial flakes in the low-density core for wood composites (Chen and Beall 2000). In addition, the impedance (Z) increased with increasing ND in the 2% and 4% RC panels, but peaked and decreased slightly in the 6% RC panels (see **Table**

3.1). The maximum value of impedance of 1.008 Gg/s.m^2 occurred for boards at ND 0.8 RC 4%. Note the similar trend for the variables RTD and RT. For each RC level, the variables RT and RTD increased with increasing average density, the lone exception being the RTD at 6% RC. However, the variables ATD and AT consistently decreased with increasing density for each RC (in a greater magnitude for the low-density panels).

3.3.2. Two-Factor UT ANOVA Models

With RC and ND as the factors, a two-factor analysis of variance, having 801 error degrees of freedom, was performed on each of the basic UT variables, as in **Table 3.2**. All RC and ND main effects were highly significant ($p<0.0001$) for each UT variable, as were all RC*ND interactions ($p<0.0001$), except for the variable RMS Voltage ($p=0.0031$). Graphical evidence of these findings appears in **Figures 3.3a** and **3.3b**, in which the group averages of **Table 3.2** are plotted versus the ND (RC) levels by the RC (ND) levels, respectively.

Although the three RMS voltage curves in **Fig. 3.3a** are not parallel (due to significant RC*ND interaction), the 4% and 6% RC curves are parallel ($p=0.5486$ from **Table 3.2**). In addition, the RMS voltage ND 0.4 and 0.8 curves in **Fig. 3.3b** are parallel ($p=0.8457$). Although the entire velocity RC 2% and 4% curves are marginally not parallel ($p=0.0114$), the portion of these two curves between ND 0.6 and 0.8 curves are marginally parallel ($p=0.0561$). All attenuation curves for all RC and ND levels are not parallel ($p<0.0001$).

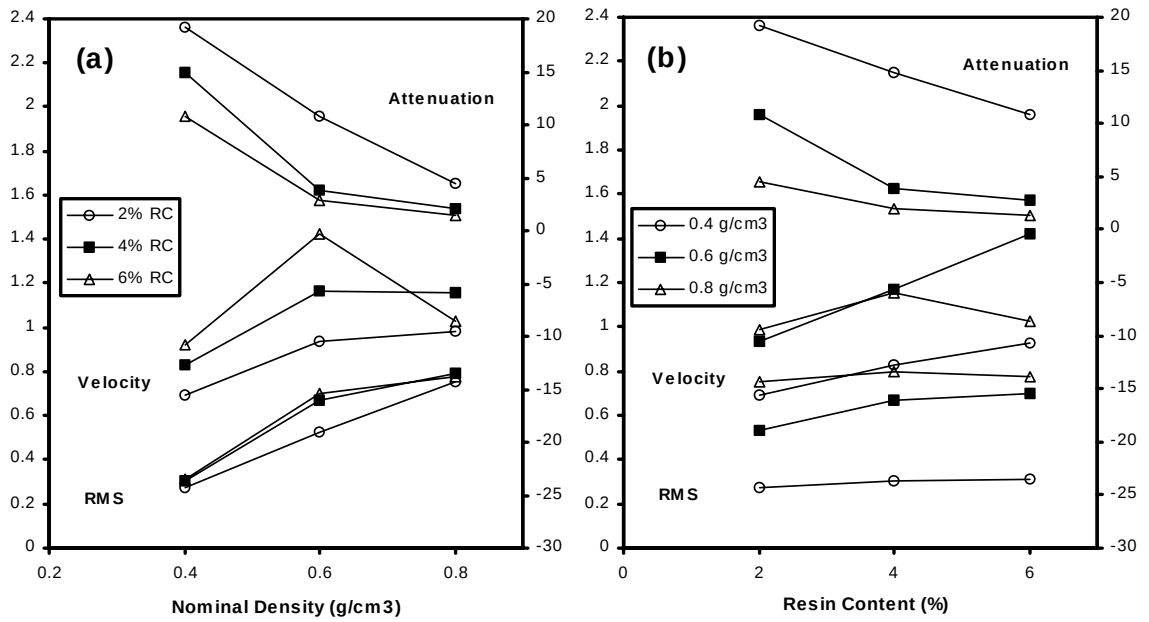

Fig. 3.3. Scatter plots for the group averages of UT variables velocity, attenuation, and RMS voltage as a function of Nominal Density (a) and Resin Content (b) levels.

Results of the pairwise comparisons of the three RC (ND) levels at each ND (RC) level for all UT variables appear in **Table 3.2**. For the UT variable velocity, the pairwise comparisons of the three ND levels for each RC level were highly significant, with two exceptions: for RC 4%, there is no difference between ND 0.6 and 0.8 ($p=0.5597$); for RC 2%, there is only marginal evidence of a difference between ND 0.6 and 0.8 ($p=0.0342$). Again, for velocity, the pairwise comparisons of the three RC levels for each ND level were highly significant, except for RC 2% and 6% at ND 0.8 ($p=0.0731$).

For the UT variable attenuation, all pairwise comparisons of the ND levels at each RC level were highly significant; while the pairwise comparisons of the RC levels at each ND level were highly significant, except for RC levels 4% and

6% at ND 0.6 and, again, at ND 0.8 ($p=0.0816$ and $p=0.2341$, respectively). As for the UT variable RMS voltage, all of the pairwise comparisons of the three ND levels for each RC level were highly significant, the lone exception being the marginal significance ($p=0.0149$) of ND 0.6 versus ND 0.8 for RC 6% level. However, all of the pairwise comparisons of the three RC levels for each ND level were not significantly different, with two exceptions: for ND 0.6, RC 2% is highly significantly different from both 4% and 6% ($p<0.0001$).

3.3.3. UT Regressions on Average Density

Scatter plots of the UT measurements versus AD in **Fig. 3.4** reveal a quadratic relationship for each RC (as was the case in an earlier study on aspen OSB by Vun et al. 2003). Accordingly, a simultaneous regression model with 810-9=801 degrees of freedom for error, allowing different least squares quadratic functions for the three RC's, was fit to each UT variable. For each UT variable, all three quadratic coefficients were highly significant ($p<0.0001$), and the quadratic curves were found not to be parallel ($p<0.0001$). Thus, inherently different quadratics are required to describe the relationship of each UT variable to AD at the three RC's (**Table 3.3**). The three inherently different least squares quadratic curves from the simultaneous regression model are superimposed on the scatter plots of the data for the UT variables velocity, attenuation, and RMS voltage in **Fig. 3.4**.

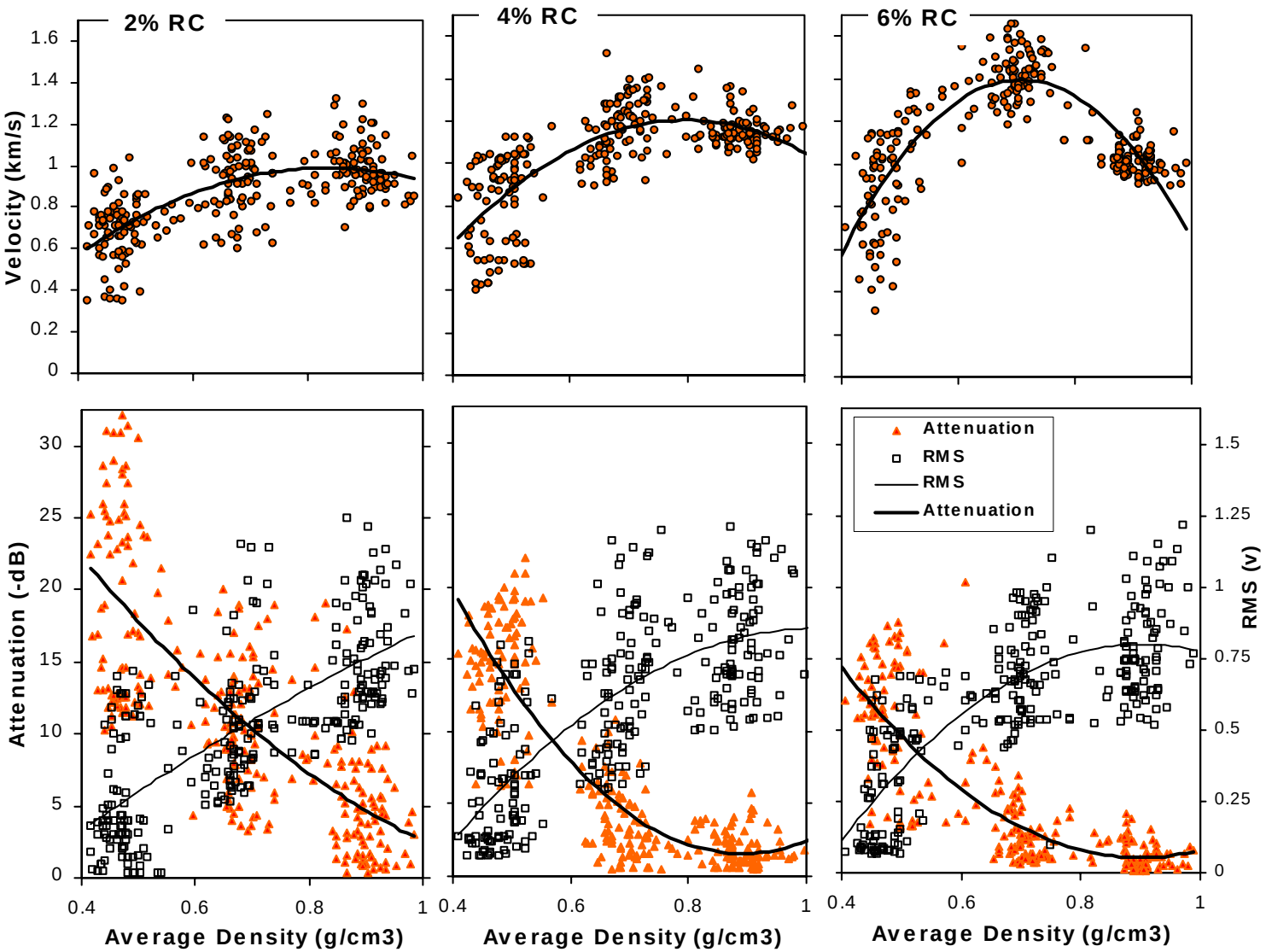

Fig. 3.4. Regressions of UT variables velocity, attenuation, and RMS voltage as a function of average density for boards at RC 2%, 4%, and 6% levels.

Table 3.3. Least squares quadratic curves
$UT = B_2(AD)^2 + B_1(AD) + B_0 + \varepsilon$
and points of intersection (by RC levels).

UT variable	RC	B_2	B_1	B_0	R^2
(a) Least Squares Curves Quadratic Function					
Velocity	2%	-2.24	3.74	-0.57	0.46
	4%	-3.71	5.91	-1.15	0.55
	6%	-8.69	12.27	-2.94	0.68
Attenuation	2%	23.12	-65.23	44.65	0.57
	4%	75.73	-134.9	61.59	0.77
	6%	53.20	-95.71	44.12	0.70
RMS Voltage	2%	-0.40	1.71	-0.46	0.51
	4%	-1.90	3.89	-1.13	0.55
	6%	-2.74	4.94	-1.42	0.61

*(b) AD points of Intersection of Least Squares Curves** *(corresponding UT values appear in brackets).*

Velocity	2%	1.13[0.79]	0.93[0.97]
	0.35[0.47]	4%	0.86[1.19]
	0.40[0.56]	0.42[0.67]	6%
Attenuation	2%	0.32[26.1]	-0.02[45.8]
	1.00[2.50]	4%	##
	1.03[1.98]	##	6%
RMS Voltage	2%	1.00[0.86]	0.94[0.80]
	0.45[0.23]	4%	0.82[0.78]
	0.44[0.22]	0.43[0.19]	6%

* $AD = (-D_1 \pm SQRT(D_1^2 - 4*D_2*D_0))/2*D_2$
where $D_i = (B_{i,RC} - B_{i',RC'})$ $i = 0, 1, 2$

Attenuation RC 4% and 6% quadratics do not intersect; minimum attenuation occurs at AD value of approximately 0.89 for each.

3.3.3.1. Velocity versus AD

For each RC level, the least squares quadratic curve rises to its apex and then falls (**Fig. 3.4**). The fall is more pronounced as RC increases, since velocity is sensitive to density changes caused by diminishing void volume as void spaces are "filled up"; moreover, better bonding occurs at higher RC levels. Particularly in the RC

2% panels, the low value for the coefficient of determination (R^2=0.46 from **Table 3.3**) was due to high variability of the UT variable velocity caused by poor interfacial flake bonding in the panels. Comparing intersection points of the least squares curves across the RC levels (**Table 3.3**), the velocity RC 2% curve intersects the RC 4% (6%) curve at the AD values 0.35 and 1.13 g/cm^3 (0.40 and 0.93 g/cm^3). Note that both 0.35 and 1.13 g/cm^3 are outside the observed data range, while 0.40 and 0.93 are both within. The velocity RC 4% curve intersects the RC 6% curve at the AD values 0.42 (at 0.67 km/s) and 0.86 (at 1.19 km/s), again, both values being within the observed data range. Clearly, maximum velocity occurs at RC 6% ND 0.6. These suggest that velocity is subject to the physical integrity of the interfacial bonding between flakes.

3.3.3.2. Attenuation/RMS Voltage versus AD

For each RC level, the least squares quadratic curve for attenuation decreases with increasing density, with only a slight increase for the RC levels 4% and 6% (**Fig. 3.4**). The least squares curves for the RMS voltage increase with increasing density, with only a slight decrease for RC 6% level. Comparing intersection points of the curves across the RC levels (**Table 3.3b**), the attenuation RC 2% curve intersects the RC 4% (6%) curve at the AD values 0.32 and 1.00 g/cm^3 (-0.02 and 1.03 g/cm^3). The attenuation values of 26.1 dB and 2.50 dB correspond to the AD values 0.32 and 1.00 g/cm^3, respectively. The attenuation RC 4% curve does not intersect the RC 6% curve; instead, the minimum attenuation for both of these curves occurs at AD value of 0.89 g/cm^3 (footnote of

Table 3.3). This density marks the transitional density separating the stage of diminishing void volume (at low density) and the stage of increasing plastic-strain hardening (at high density), which is in close agreement with that of 0.90 g/cm^3 found from the previous aspen OSB. The RMS voltage RC 2% curve intersects the RC 4% (6%) curve at the AD values 0.45 and 1.00 (0.44 and 0.94), while RC 4% intersects RC 6% curve at 0.43 and 0.82 g/cm^3. All these values are within the observed data range. In general, velocity and RMS voltage increase with increasing AD; whereas, Attenuation decreases with increasing AD. These facts also show that both attenuation and RMS voltage are invariant to interfacial boundary impediments, making them a reliable energy gauge to diagnose internal structure of materials.

3.3.4. Density Prediction

A calibration procedure was developed to predict the AD from each of the UT measurements. For each RC level, the plot of AD versus the UT variables reveals a quadratic relationship. Accordingly, a quadratic regression was performed for each of the nine data sets of **Fig. 3.5**. (Note that only data for ND 0.4 and 0.6 are plotted for the UT variable velocity at RC levels 4% and 6%). R^2 values for velocity increase with increasing RC levels, while R^2 values for RMS voltage are basically constant across RC levels. R^2 values for attenuation increase as RC increases from 2% to 4%, and decrease slightly from RC 4% to 6%.

Percent out-of-limits (POFL) of the predicted values (i.e., the predicted values within a panel that are not within 10% of the average of the measured AD's

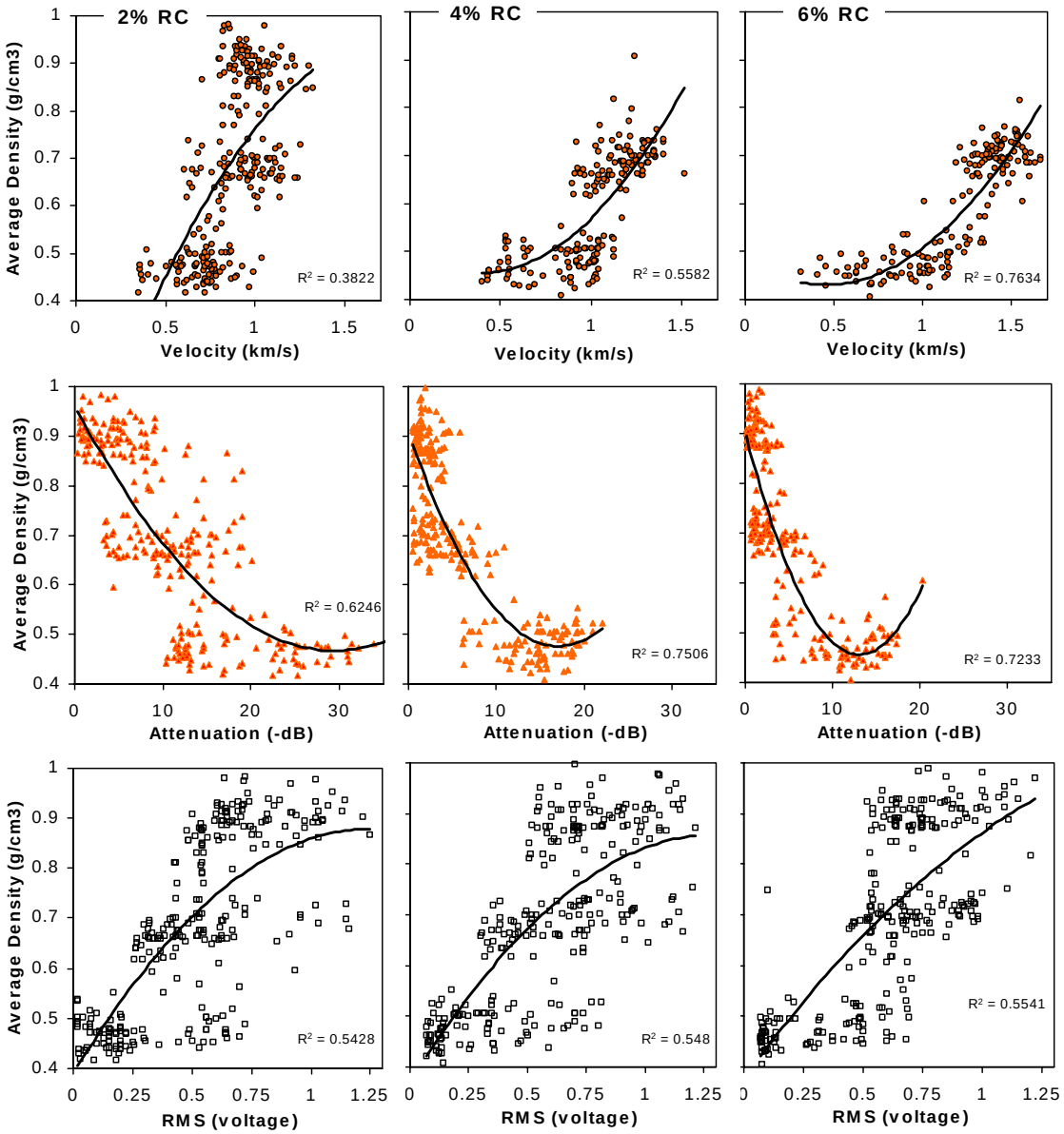

Fig. 3.5. Calibration regressions of measured density as a function of UT predictors velocity, attenuation, and RMS voltage for boards at RC 2%, 4%, and 6% levels.

for the panel) for these simple regression models were, in general, high (e.g., when the quadratic model for velocity was fit to all of the data, the out-of-limits predicted values for all RC and ND combinations exceeded 68%, the lone exception being RC 6% with ND 0.60). To improve on the POFL predicted values, logarithmic, power,

and/or product functions of the original UT variables were included to form new models.

The General Model having 18 predictors for any given RC level is

$$Y_{ij} = B_0 + \sum_{k=1}^{3} A_k Ln(X_{ijk}) + \sum_{k=1}^{3} C_k X_{ijk} + \sum_{k=1}^{3} D_k X_{ijk}^2 + \sum_{k=1}^{3} E_k Ln(X_{ijk}) * X_{ijk} + \sum_{k \neq k'} \sum F_k Ln(X_{ijk}) * X_{ijk'} + \varepsilon_{ij} \quad \textbf{(3.5)}$$

where Y_{ij} is the AD measurement for specimen *ij* obtained from the grid *i* and *j*, X_{ijk} is the UT measurement (k=1, 2, 3; for Velocity, Attenuation, RMS voltage) for specimen *ij*, ε_{ij} is the random error term, B_o is the intercept, and A_k, C_k, D_k, E_k, F_k are the coefficients.

An alternative Polynomial Model for the density, also with 18 predictors, for any given RC level is

$$Y_{ij} = B_0 + \sum_{k=1}^{3} A_k X_{ijk} + \sum_{k=1}^{3} C_k X_{ijk}^2 + \sum_{k=1}^{3} D_k X_{ijk}^3 + \sum_{k \neq k'} \sum E_k X_{ijk} * X_{ijk'} + \sum_{k \neq k'} \sum F_k X_{ijk} * X_{ijk'}^2 + \varepsilon_{ij} \quad \textbf{(3.6)}$$

For each of three data sets (Data1 composed of all ND's data sets, Data2 composed of ND 0.4 and 0.6 data only, Data3 composed of ND's 0.6 and 0.8 data only), final models were obtained from the backward elimination procedure using least squares regression. Backward elimination starts with the full model and removes variables one at a time until all variables remaining are significant at 0.10 level in order to capture the data natural variability. All of the final models obtained had significant variable coefficients. For example, all coefficients in the

General Model when applied to Data3 for RC 4% are significant with $p \leq 0.0013$ as in **Table 3.4**.

Judging from the standardized coefficient values, the velocity (RMS voltage and/or attenuation) terms contribute more profoundly to both the General and Polynomial Models for the higher density specimens of Data3 at the higher (lower) RC levels (see **Table 3.4** for the standardized coefficients of the General Model). As is the case for Data3, velocity and the RMS voltage/attenuation combination form complementary terms in influencing the AD estimation for Data2. Again, this suggests that the velocity predictor is affected by weak bonding or physical impediments in the interfacial boundaries; whereas, both the attenuation and RMS voltage predictors provide good measures of ultrasonic energy transmissivity.

For both the General and Polynomial final models, R^2 values increase with increasing RC levels for Data1 and Data2. For Data3, however, R^2 values decrease from RC 2% to 4%, before increasing to its maximum value at RC 6%. For the same Data and RC levels, R^2 values for the General and Polynomial final models are very similar (**Table 3.5**).

Predicted Residual Sum of Squares (PRESS), a measure of prediction error, was obtained for each of the final regression models. PRESS is calculated as Σd_i^2, where $d_i = Y_i - \hat{Y}_{i(i)}$ for $\hat{Y}_{i(i)}$ the predicted value for the *i*th observation using the coefficient estimates obtained when the *i*th observation is deleted; d_i also equals

Table 3.4. General and Polynomial Models for predicting density (AD) as a function of the UT variables: V, A, R = Velocity (km/s), Attenuation (-dB), RMS voltage for Data3. Std. Est is the standardized coefficient estimate.

	General Model: $AD = B_o + Ln(V) + Ln(A) + Ln(R) + V + A + R + V^2 + A^2 + R^2 + Ln(V)*V + Ln(V)*A + Ln(V)*R + Ln(A)*V + Ln(A)*A + Ln(A)*R + Ln(R)*V + Ln(R)*A + Ln(R)*R$					Polynomial Model: $AD = B_o + V + V^2 + V^3 + A + A^2 + A^3 + R + R^2 + R^3 + VA + VR + AR + V^2A + VA^2 + V^2R + VR^2 + A^2R + AR^2$				
RC	Variable	Est.	Std.Err	Pr>|t|	Std. Est.	Variable	Est.	Std.Err	Pr>|t|	Std. Est.
2%	B_o	-28.70	7.65	0.0002	0.0	B_o	-0.10	0.12	0.4171	0.0
	Ln(V)	-1.09	0.37	0.004	-1.4	A^2	0.00	0.00	0.0835	-0.6
	Ln(R)	-8.97	2.47	0.0004	-29.6	R	4.97	0.80	<.0001	10.2
	R	16.00	4.32	0.0003	32.8	R^2	-3.77	0.84	<.0001	-11.1
	V^2	0.42	0.16	0.0111	1.0	VR	-2.39	1.06	0.0258	-5.7
	R^2	13.19	3.49	0.0002	38.7	AR	-0.05	0.01	<.0001	-0.9
	Ln(V)*A	0.08	0.02	<.0001	1.3	R^3	1.24	0.38	0.0012	4.4
	Ln(A)*V	-0.27	0.09	0.0021	-1.9	VA^2	0.00	0.00	0.0007	1.1
	Ln(A)*R	0.15	0.09	0.0928	0.6	V^2R	0.99	0.51	0.0526	2.8
	Ln(R)*A	-0.03	0.01	0.0006	-1.3					
	Ln(R)*R	-33.97	8.60	0.0001	-44.2					
4%	B_o	-37.46	6.68	<.0001	0.0	B_o	-8.56	3.40	0.0128	0.0
	Ln(A)	-3.29	0.54	<.0001	-22.8	V	29.68	8.60	0.0007	30.7
	A	0.36	0.08	<.0001	7.0	V^2	-24.26	7.28	0.0011	-59.0
	V^2	20.37	5.02	<.0001	49.6	A	-1.01	0.21	<.0001	-19.8
	A^2	-0.02	0.01	0.0003	-3.6	A^2	0.10	0.02	<.0001	18.6
	R^2	17.44	2.66	<.0001	54.8	R	-3.43	0.67	<.0001	-7.2
	Ln(V)*V	-47.48	10.99	<.0001	-56.8	AR	1.17	0.29	<.0001	9.2
	Ln(V)*A	-0.35	0.10	0.0008	-1.3	V^3	6.51	2.04	0.0017	28.4
	Ln(V)*R	8.81	1.44	<.0001	6.6	A^3	0.00	0.00	0.0003	-5.5
	Ln(A)*V	0.96	0.29	0.0013	7.4	R^3	0.94	0.20	<.0001	3.6
	Ln(A)*R	1.85	0.27	<.0001	7.6	A^2R	-0.06	0.02	0.0005	-5.0
	Ln(R)*V	-4.46	0.58	<.0001	-15.3	AR^2	-0.28	0.11	0.0115	-1.4
	Ln(R)*A	-0.18	0.05	0.0007	-3.6					
	Ln(R)*R	-31.03	4.82	<.0001	-44.6					
6%	B_o	388.21	124.30	0.0021	0.0	B_o	-2.72	0.71	0.0002	0.0
	Ln(V)	174.81	54.00	0.0015	293.3	V	9.79	1.72	<.0001	20.1
	Ln(A)	0.16	0.07	0.0248	1.3	V^2	-7.75	1.38	<.0001	-39.6
	Ln(R)	-0.62	0.15	.0001	-1.6	A	0.25	0.11	0.0289	4.0
	V	-342.43	106.66	0.0016	-701.6	A^2	0.01	0.00	0.0045	1.7
	V^2	-48.49	17.83	0.0072	-247.7	VA	-0.68	0.16	<.0001	-15.5
	R^2	3.67	0.75	<.0001	9.6	VR	-0.99	0.19	<.0001	-2.5
	Ln(V)*V	264.13	88.30	0.0032	655.8	AR	0.21	0.05	<.0001	1.9
	Ln(V)*A	0.16	0.04	<.0001	1.0	V^3	1.89	0.36	<.0001	18.4
	Ln(A)*V	-0.23	0.06	0.0002	-2.3	R^3	0.22	0.04	<.0001	0.7
	Ln(A)*A	-0.02	0.00	<.0001	-0.7	V^2A	0.29	0.06	<.0001	9.5
	Ln(A)*R	0.13	0.03	<.0001	0.7	V^2R	0.45	0.10	<.0001	2.1
	Ln(R)*V	-0.23	0.10	0.0202	-0.8	A^2R	-0.02	0.01	0.0033	-1.7
	Ln(R)*R		1.29	<.0001	-7.5					

$(Y_i - \hat{Y}_i)/(1-h_{ii})$, when $\hat{Y}_i$ is the predicted value for the *i*th observation using all of the data, and h_{ii} is the *i*th diagonal element of the Hat matrix using all of the data (Neter et al. 1996).

Both the Polynomial and General Models exhibit a decreasing trend in square root PRESS as RC levels increase for Data1. For Data2, root PRESS decreases as RC increases from 2% to 4% and then remains basically constant as RC increases from 4% to 6%. For Data3, root PRESS increases and then drops to its minimum value as RC levels increase (see **Table 3.3**). Trends also exist in the R^2 values as RC increases. These trends are more complementary (as opposed to similar) in nature to the root PRESS trends.

3.3.5. Average Density Validation

The EN300 panel standard allows for a 10% variation from the average of the measured AD's within a panel. Accordingly, the control lower (upper) limit for a panel is 0.90•panel average measured AD's (1.10•panel average measured AD's). Control limits for the measured AD's were evaluated for each of the nine panels included in this study (see **Table 3.5**). Note that for the ND 0.40 panels, POFL increased as RC increased, all three POFL's exceeding the allowed 10%. For the ND 0.60 panels, POFL decreased as RC increased, with only the RC 2% panel marginally out-of-limits (10%). For the ND 0.80 panels, all RC levels had POFL less than 10%. Using our nine sets of control limits, it appears necessary to manufacture at least 0.60 g/cm^3 panels to conform to the EN300 standard.

Table 3.5. Summary of the out-of-limits percentages for AD measured and predicted values.

Test Panels			Control	Out-of-Limits						
RC	ND	AD	Limits	Measured	General Model			Polynomial Model		
(%)	g/cm^3)	(g/cm^3)	±10%	Data	Data1	Data2	Data3	Data1	Data2	Data3
2%	0.40	0.476	[.429, .524]	12.2%	46.7%	53.3%		51.1%	52.2%	
	0.60	0.686	[.618, .755]	10.0%	35.6%	28.9%	36.7%	34.4%	27.8%	44.4%
	0.80	0.894	[.805, .984]	4.4%	33.3%		18.9%	31.1%		24.4%
				R^2	0.72	0.56	0.64	0.74	0.58	0.60
				√PRESS	(1.58)	(1.09)	(0.96)	(1.54)	(1.06)	(1.00)
4%	0.40	0.482	[.434, .531]	14.4%	24.4%	11.1%		18.9%	13.3%	
	0.60	0.691	[.622, .760]	8.9%	43.3%	12.2%	40.0%	51.1%	8.9%	46.7%
	0.80	0.887	[.798, .976]	7.8%	20.0%		18.9%	17.8%		16.7%
				R^2	0.83	0.83	0.56	0.81	0.82	0.49
				√PRESS	(1.23)	(0.63)	(1.09)	(1.27)	(0.65)	(1.27)
6%	0.40	0.479	[.432, .527]	18.9%	44.4%	41.1%		47.8%	40.0%	
	0.60	0.699	[.629, .769]	5.6%	21.1%	11.1%	3.3%	17.8%	12.2%	5.6%
	0.80	0.899	[.810, .989]	4.4%	24.4%		6.7%	21.1%		4.4%
				R^2	0.86	0.84	0.91	0.86	0.85	0.90
				√PRESS	(1.15)	(0.67)	(0.57)	(1.15)	(0.65)	(0.47)

Control Limits: within 10% deviation from individual measured AD's in each test panel.
Out-of-limits: percent of 90 specimens not within Control Limits.
Data1: fit to ND's 0.4, 0.6, and 0.8 (270 specimens total).
Data2: fit to ND's 0.4 and 0.6 only (180 specimens total).
Data3: fit to ND's 0.6 and 0.8 only (180 specimens total).

For all final models, the predicted AD's were *in situ* matched with the measured AD's as points (**Fig. 3.6** showing the control charts for each test panel). The POFL for the predicted values in each panel using the EN300 panel control limits was computed for each model and is reported in **Table 3.5** for each data set. Generally, the models for Data1 produce greater overall prediction error than those for Data2 or Data3 (the root PRESS values exhibit the same tendencies). For the

Polynomial Model using Data1, the smallest POFL was 17.8%, attained at both RC 4% ND 0.80 and RC 6% ND 0.60. Generally using Data1, predictions at the RC 2% level did not agree with their measured counterparts, producing POFL's ≥ 31.1%.

For the General Model applied to Data2, the minimum POFL of 11.1% was attained at both RC 4% ND 0.40 and RC 6% ND 0.60. For the Polynomial Model applied to Data2, the minimum POFL of 8.9% was attained at RC 4% and ND 0.60. When restricted to Data3, both the General and Polynomial Models were within the 10% control limits for RC 6%. This suggests that the models required at least 0.60 g/cm^3 targeted nominal density for ultrasonic monitoring of OSB horizontal density variation.

The dispersion of the predicted out-of-limits points was similar to the spatial dispersion of the measured out-of-limits points, as is seen in **Fig. 3.6**. Inasmuch as we want to replicate the natural fluctuation of the density variations, the smoothing effects of the regressions result in some discrepancies in the *in situ* locations of the predicted AD's. **Fig. 3.7** compares a typical spatial color contour of the measured to predicted AD's in the RC 2% and 6% panels. There is a reasonable spatial resemblance of the horizontal density to the measured AD's as predicted by the General Models. The General Models are spatially cohesive to the measured AD's, shown by the out-of-limits points (the Polynomial Models are not especially cohesive). Again, by visual comparisons, the prediction of the density improves with increasing ND and RC levels.

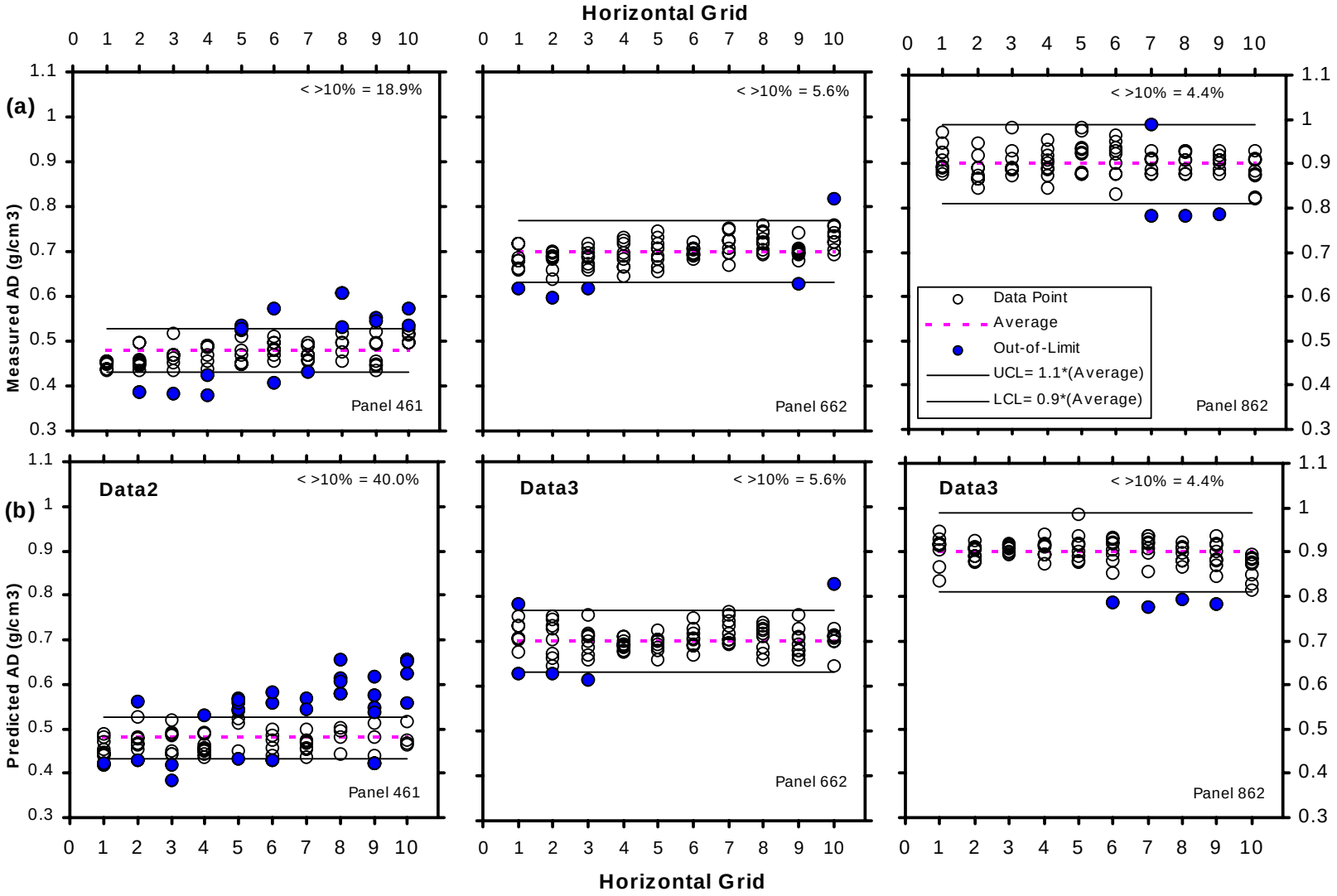

Fig. 3.6. Control charts for AD's measured (a) and Polynomial-predicted (b) for the ND 0.40, 0.60, 0.80 RC 6% panels.

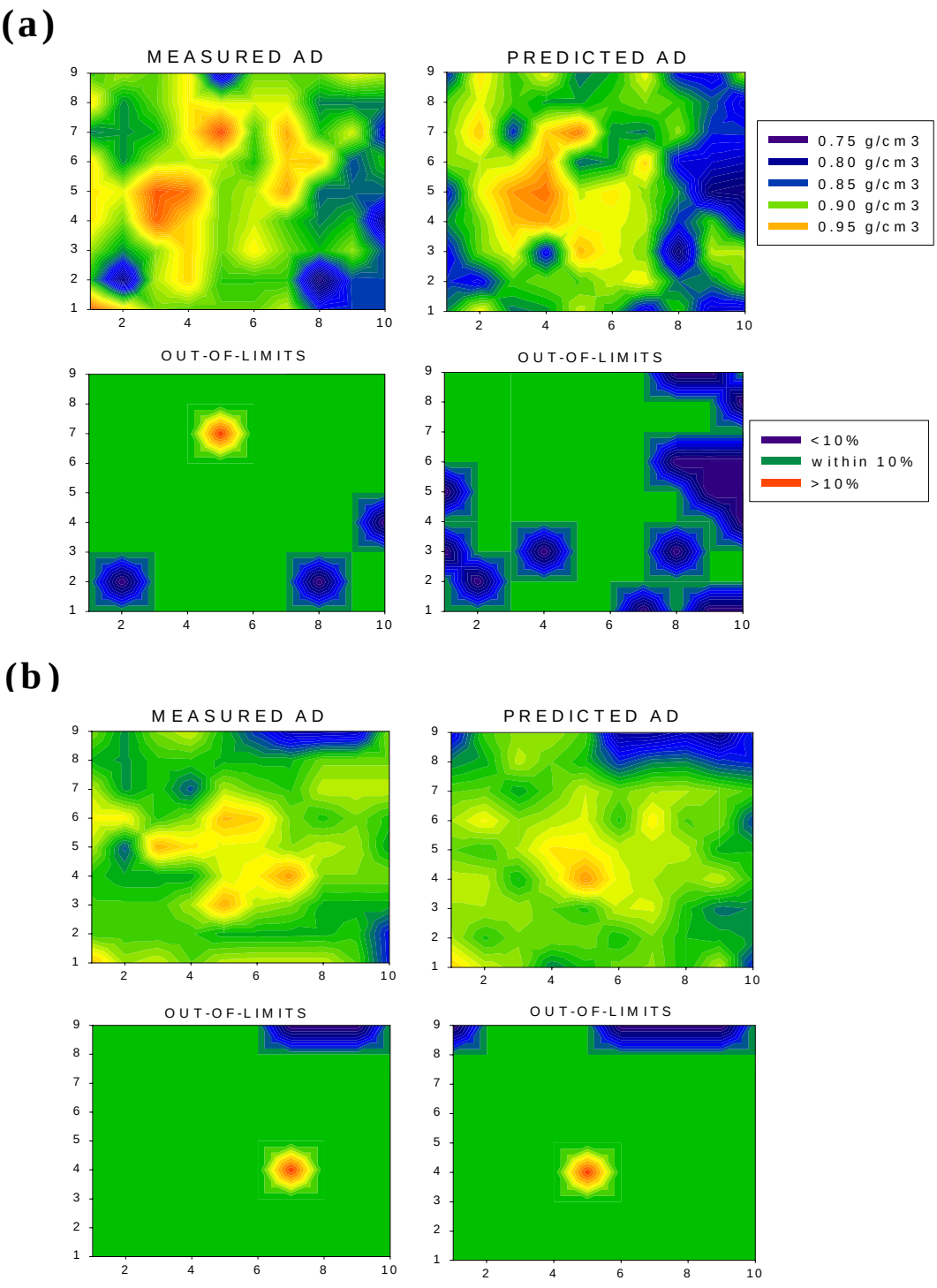

Fig. 3.7. Contour and out-of-limit plots comparing the spatial AD's measured and General model-predicted for RC 2% (a) and RC 6% (b) for ND 0.80 g/cm^3 fitting Data3.

Sampling effects of this contact ultrasonic technique may contribute to the AD measurement errors. For example, the corners of the 51x51 mm^2 specimen (contributing to the additional density measure) are not accounted for in the ultrasonic readings as limited by the circular transducer size. Smaller transducers may provide different resolution (i.e., sampling size) to capture the representative material characteristics (determined by flake dimension, resin content and distribution, and prevalence of fines and/or macrovoids) that are contained within the specimen. Optimal sampling size for capturing ultrasonic information still remains unknown.

3.4. CONCLUSIONS AND RECOMMENDATION

Horizontal density variation is inherent in OSB, because of random particle deposition in the mat formation process resulting in inevitable embedded voids (of low-density range) and discrete consolidated particle structures (of high-density range). Having consistent horizontal density distribution within a flakeboard is important in determining its creep resistance and durability in service.

Ultrasonic nondestructive techniques provide valuable tools in product design and property characterizing and monitoring. Mechanical properties of OSB can be approximated using the UT variable responses. Particularly, velocity is sensitive to density changes caused by the mechano-chemical process of panel densification in the hot press. The attenuation vs average density (AD) quadratic curves for RC 4% and 6% have their minimum at the AD value 0.89 g/cm^3, which marks the transitional density separating the stage of diminishing void volume (at

low density) and the stage of increasing plastic-strain hardening (at high density). This density is in close agreement with that of 0.90 g/cm^3 found from the aspen OSB by Vun et al. (2003).

For the low RC and ND levels, the existence of high variability in the UT responses also corresponds to the high variability in the measured AD, attributed to the existence of low-density elements and discontinuities arising from poorly bonded interfacial flake zones in the panels. As discussed earlier, velocity was validated to be an influential AD predictor when nominal density exceeds 0.60 g/cm^3. An influential velocity variable coincides with higher density (i.e., fewer voids and therefore, less physical impediment in the propagation path); whereas, influential attenuation and RMS voltage variables coincide with a high level of ultrasonic energy transmission through a low density medium. The different responses of the UT variables to density across the RC and ND levels, therefore, form excellent complementary predictors of density. The General Models produced spatially cohesive AD's predicted to measured resulting in smaller percent out-of-limits. Visual resemblance of the predicted density improves with increasing ND and RC levels. From the control limits of ± 10% of the panel average density, it is necessary to manufacture at least 0.60 g/cm^3 panels to conform to the EN300 standard.

UT investigation of the horizontal density is convenient and appropriate for monitoring structural quality of a large panel. This study acknowledges the challenging problems in wood composite studies that can cause grossly attenuated

UT signal responses due to coupling contact systems, surface-quality, anisotropy, basic growth properties of wood flakes, presence of interfacial macrovoids, and the nature of discrete consolidated particle structures. UT responses may also be adversely affected by the medium composition and the transducer size (or the corresponding sampling area). We recommend further studies (1) to explore other orthoregression, partial least squares, nonlinear and geostatistic approaches to spatial modeling, (2) to explore other coupling systems, and (3) to investigate the effects of sampling/transducer size on the density and ultrasonic measurements.

3.5. REFERENCES

Beall, C. F. 2002. Overview of the use of ultrasonic technologies in research on wood properties. Wood Sci. Technol. (36): 197-212.

Bucur, V., M.P. Ansell, C.Y. Barlow, J. Pritchard, S. Garros, and X. Deglise. 1998. Physical methods for characterizing wood composite. Holzforschung (52):553-561.

Chen, L-H, and F.C. Beall. 2000. Monitoring bond strength development in particleboard during pressing, using acousto-ultrasonics. Wood Fiber Sci. 32(4): 466-477.

Dai, C. and P.R. Steiner. 1994. Spatial structure of wood composites in relation to processing and performance characteristics: Part 2. Modeling and simulation of a randomly-formed flake layer network. Wood Sci. Technol. (28):135-146.

Dai, C. and P.R. Steiner. 1994. Spatial structure of wood composites in relation to processing and performance characteristics: Part 3. Modeling the formation of multi-layered random flake mats. Wood Sci. Technol. (28):229-239.

Kruse, K., C. Dai, and A. Pielasch. 2000. An analysis of strand and horizontal density distributions in oriented strand board. Holz Roh-Werkstoff 58(4):270-277.

Jeong, H., and D.K. Hsu. 1995. Experimental analysis of porosity-induced ultrasonic attenuation and velocity change in carbon composites. Ultrasonics 33(3): 195-203.

Judd, N.C.W., W.W. Wright. 1978. Voids and their effects on the mechanical properties of composites-An appraisal. SAMPE Journal, Jan./Feb.: 10-14.

Lenth, C.A., and F.A. Kamke. 1996. Investigations of flakeboard mat consolidation. Part I. Characterization the cellular structure. Wood Fiber Sci. 28(2): 153-167.

Linville, Jeffrey D. 2000. The influence of horizontal density distribution on moisture-related mechanical degradation of oriented strand composites. M.Sc. thesis, Department of Civil and Environmental Engineering, Washington State University, Pullman, WA.

Lu, C., and F. Lam. 1999. Study on the X-ray calibration and overlap measurements in robot formed flakeboard mats. Wood Fiber Sci. 33:85-95.

Lu, C., and F. Lam. 2001. Random field representation of horizontal density distribution: I. partially oriented strandboard mat. Wood Fiber Sci. 33(3):437-449.

Lu, C., and F. Lam. 2001. Relationship between thickness swelling and mat structures in robot-formed flakeboard mats. Holz als Roh- und Werkstoff 59:201-210.

Neter, J., M.H. Kutner, C.J. Nachtsheim, and W. Wasserman. 1996. Applied Linear Statistical Models. 4th Ed. Irwin McGraw-Hill, Chicago:345-373.

Oudjehane, A., and F. Lam. 1998. On the density profile within random and oriented wood-based composite panels: horizontal distribution. Composites part B 29B: 687-694.

Oudjehane, A., F. Lam, and S. Avramidis. 1998. A continuum model of the interaction between manufacturing variables and consolidation of wood composite mats. Wood Sci Techn 32:381-391.

Ross, R.J. and R.F. Pellerin. 1988. NDE of wood-based composites with longitudinal stress waves. Forest Prod. J. 38(5): 38-45.

Smith, C.D. 1982. Waferboard press closing strategies. Forest Prod.J. 32(3):40-45.

Shi, Q. Sheldon, and D.J. Gardner. 1999. An evaluation of analysis methods to eliminate the effect of density variation in property comparisons of wood composites. Wood Fiber Sci. 31(2):164-172.

Steiner, P.R., and C. Dai. 1993. Spatial structure of wood composites in relation to processing and performance characteristics: Part 1. Rationale for model development. Wood Sci. Technol. (28):45-51.

Suchsland, O. 1962. The density distribution in flakeboard. Q. Bull., Michigan Agric. Expt. Sta., Michigan State Univ. 45(1):104-121.

Suchsland, O, and H. Xu. 1989. A simulation of the horizontal density distribution in a flakeboard. Forest Prod. J. 39(5): 29-33.

Suchsland, O, and H. Xu. 1991. Model analysis of flakeboard variables. Forest Prod. J. 41(11/12):55-60.

Suddarth, S.K. 1965. Detection of adhesive bond defects in the Polaris missile nose firing through mechanical impedance measurements. Pages 267-285 i*n* 2nd Nondestructive Testing of Wood Symposium, April 1965. Washington State University, Pullman, WA.

Vogt, J.J. 1986. Longitudinal stress waves as predictors of internal bonding strength. *In* 12th. Particleboard/Composite Materials Symposium, March 1986. Washington State University, Pullman, WA.

Vun, R.Y, and F.C. Beall. 2002. Monitoring creep rupture in oriented strandboard using acoustic emission. *In* International NDT2002 Symposium, 19-21 August 2002. University of California, Berkeley, CA.

Vun, R.Y, Q. Wu, M.C. Bhardwaj, and G. Stead. 2003. Ultrasonic Characterization of Structural Properties of Oriented Strandboard: Direct-Contact vs. Non-Contact methods. Wood Fiber Sci. 35(3).

Winistorfer, P.M., W.W. Jr. Moschler, S. Wang, E. DePaula, and B.L. Bledsoe. 2000. Fundamentals of vertical density profile formation in wood composites. Part 1. In-situ density measurement of consolidated process. Wood Fiber Sci. 32(2):209-219.

Wolcott, M.P., F.A. Kamke, and D.A. Dillard. 1990. Fundamentals of flakeboard manufacture: viscoelastic behavior of the wood component. Wood Fiber Sci. 22(4):345-361.

CHAPTER 4. NON-CONTACT ULTRASONIC CHARACTERIZATION OF PROPERTIES IN ORIENTED STRANDBOARD

4.1. INTRODUCTION

Nondestructive evaluation technologies have been utilized to study internal material properties such as defects and bonding quality for composite materials (Beall 2002, Bucur et al. 1998). Among various scanning methods (Szymani 1985), only ultrasonics and electromagnetic have the potential to reveal defects that are not visible on the surface. Because the propagation of stress wave is essentially a mechanical phenomenon, there are commonly used techniques in wood-related research such as forced vibration (Suddarth 1965), impact stress wave (Ross and Pellerin 1988, Vogt 1986), acousto-ultrasonics (Chen and Beall 2000), and acoustic emission (Vun and Beall 2002). In addition to these techniques, the ultrasonic through-transmission (UT) is simply done by transmitting ultrasonic pulses on one side through a specimen and capturing the response signals on the opposite side (Bhardwaj 2002). Energy absorption and scattering of elastic waves on discontinuity in interfacial boundaries result in an attenuated signal – that defines the internal structure and material properties (Judd and Wright 1978). The ability to continuously scan a relatively large surface area makes UT technique an appropriate tool for studying the characteristics of material properties and evaluating the mechanical behavior over spatial distribution in the horizontal plane of the panels.

The mechanical strength of oriented strandboard (OSB) is strongly related to mean panel density and in-plane density distribution. In-plane density variation exists due to random particle deposition in mat forming process (Suchland 1962, Suchsland and Xu 1989). Contributing directly to density variation, intrinsic raw material attributes, such as strand type and geometry, amount of fines, strand dimension and configuration, form the basic modeling factors for spatial structure of wood composite (Steiner and Dai 1993). Expensive γ-ray system was successfully used to diagnose density variation in laboratory experiments (Wolcott et al. (2001). However, there is no low cost tool which is safe enough for an online application. Both the direct-contact and non-contact ultrasonic techniques have been shown to be a feasible nondestructive and non-invasive tool to evaluate density and mechanical properties of OSB (Vun et al. 2003a). The direct-contact UT adopted by Vun et al. (2003b) produces an acceptable spatial imaging of the density distribution over the whole boards. The industry standard of the European EN300 for controlling density variation in panel manufacturing requires the horizontal density to conform within ±10% of the panel average density (Kruse et al. 2000).

Online applications of the UT technology as a diagnostic system are often beset with the need of physical coupling of transducers onto the materials using gels, grease, water, etc. Thus, the elimination of contact will facilitate evaluation and tests of green, unpolymerized, liquid-sensitive, and porous materials, in-process materials that are continuously formed or rolled on a production line, food

and pharmaceutical products; and non-invasive diagnostics of human skin (Bhardwaj 2002). With the availability of the high transduction air-coupling transducers, the non-contact ultrasound (NCU) is, therefore, highly desirable as a characterizing tool for wood-related research and online process inspection for a variety of bio-based panels. In addition, NCU offers a cost-effective alternative to direct-contact ultrasound, hazardous expensive X-ray, γ-ray, neutron, infrared, laser, electromagnetic acoustics, and nuclear magnetic resonance methods.

In this part of the study, the horizontal density distributions in OSB were evaluated using the NCU technology. The objectives were (1) to establish relationships between the ultrasonic parameters and sample density; (2) to develop a calibration technique of ultrasonic measurements for spatial density distribution and mapping; and (3) to validate the models by comparing the measured and predicted densities for each large panel based on the EN300 standard.

4.2. EXPERIMENTAL PROCEDURES

4.2.1. Specimen Preparation

Loblolly pine (*P. taeda*) trees of about 46 cm in diameter were harvested from Lee Memorial Forest, located near Bogalusa, Louisiana. The logs were band-sawn into boards in the field. The boards were flaked in the laboratory to produce 0.635x13x76-mm flakes using a disc flaker. The flakes were dried and screened. Eighteen random single-layer (13x510x560 mm) OSB panels were manufactured using liquid phenol-formaldehyde resin. Each board was made with 0.5% wax at each of three resin content (RC) – 2%, 4%, or 6%, and each of three nominal

density (ND) levels – 0.4, 0.6, or 0.8 g/cm^3. Two replicates of each board were made. The mats were hot pressed for 7 minutes at 190^{o}C under 4.44 MPa pressure to cure the resin. After pressing, the boards were cooled at 24^{o}C and 60% relative humidity and then trimmed to reduce edge effects on test specimens. A 10x9 grid was then drawn on each board (**Fig. 4.1b**), of which each grid was subjected to nondestructive ultrasonic evaluations.

4.2.2. Non-Contact Transmission

For each board, NCU measurements (including velocity and attenuation) were taken for each specimen as defined by the grid. A SecondWave NCA1000-2E, non-contact ultrasonic system equipped with two 100-kHz 25-mm NCT101 transducers, was used in a through-thickness measurement (**Figures 4.1a** and **4.1c**). The details of the system and NCU parameters used are described in Section 2.2.3. The X-Y platform equipped with movement computer-controlled transducers system provided the raster scanning and displays of the whole specimens (**Fig. 4.1d**).

4.2.3. Density Profile

After NCU testing, each test panel was ripped according to the grid to obtain ninety 13x51x51 mm specimens. Each specimen was measured for the average density (AD). Density profiles across the specimen thickness and width were also obtained using a Quintek X-ray Density Profiler (QDP-01X). For each panel, the maximum, average, and minimum densities for each of the test specimens were determined using the profiles.

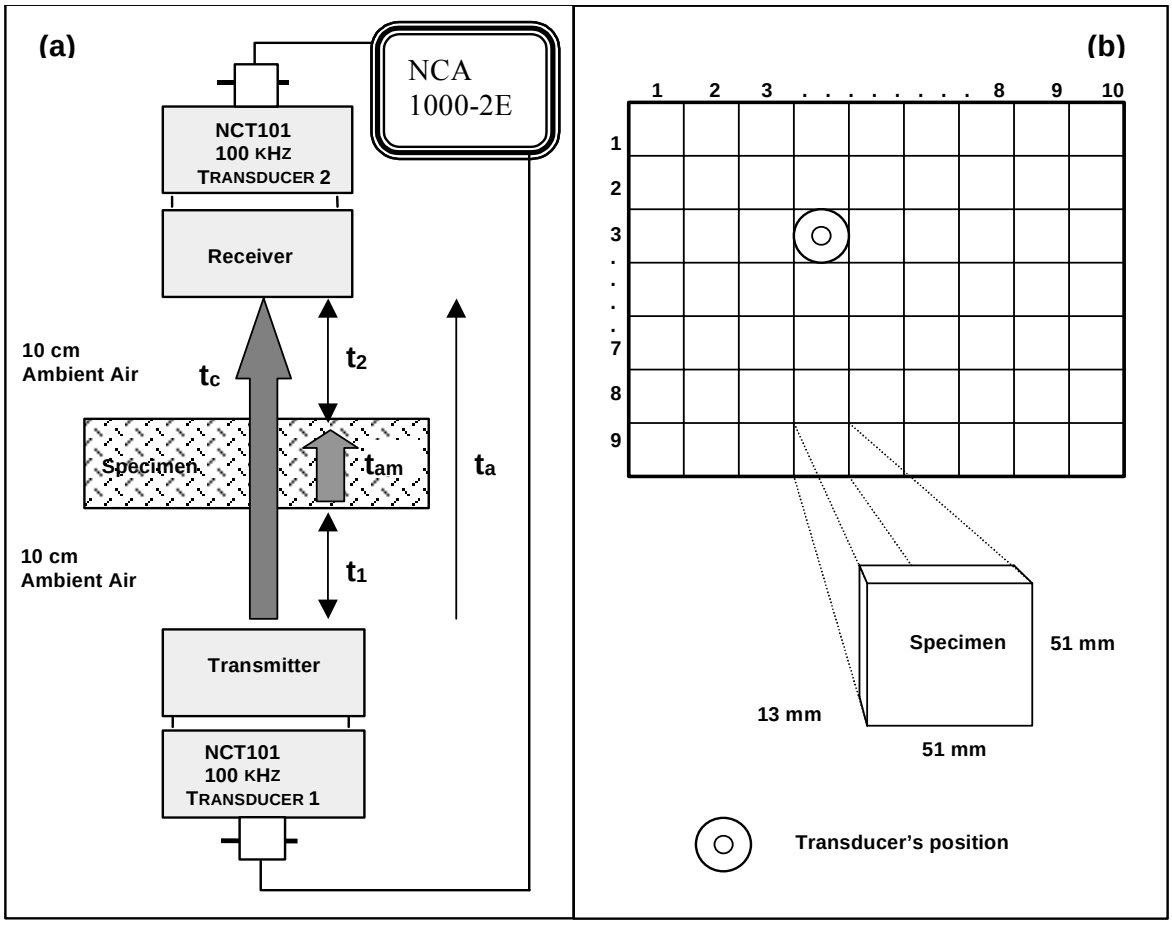

Fig. 4.1ab. Setup for non-contact ultrasonic system (a) and test panel configuration (b).

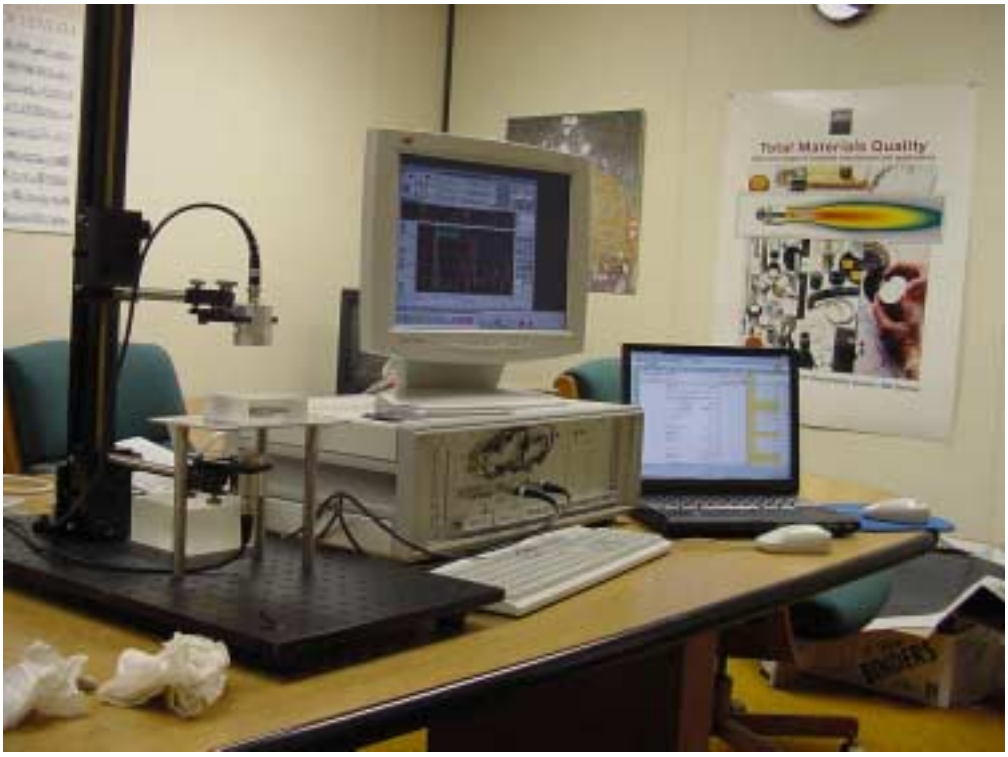

Fig. 4.1c. Non-contact Analyzer NCA1000E for small specimens scanning.

Fig. 4.1d. Non-contact Analyzer NCA1000E with transducers mounted on movable arm for dynamic scanning of laboratory size test panels.

4.2.4. Statistical Analyses

SAS (2000) software was used to perform the necessary analyses of variance for all NCU variables and specimen ADs by RC and ND levels. The regression models were generated to correlate the ultrasonic measurements and predict *in situ* densities across the three ND (0.4, 0.6, and 0.8 g/cm^3) and three RC (2%, 4%, and 6%) levels.

4.3. RESULTS AND DISCUSSION

4.3.1. Basic Panel and NCU Properties

Descriptive statistics for the panel and NCU variables segregated by RC and ND levels are given in **Table 4.1**. The coefficient of variation, or CV, was calculated for each property. The CV values for variable AD in ND 0.4 panels were always the highest (9.3% or less). For all other NCU variables, CV values decreased with increasing nominal densities and increasing RC levels. However, the attenuation, transmissivity coefficient, and attenuation corrected to thickness (AT) tended to have low CV values at ND 0.60 level (Particularly for the RC 6%, both ND 0.6 and 0.8 values were insignificantly different, $p \geq 0.12$).

The NCU group averages by ND and RC levels are plotted in **Fig. 4.2**. For both RC 4% and 6%, the NCU velocity values reached a peak at ND 0.60. For RC 2% level, the velocity values increased with increasing density. The impedance (Z) – the product of velocity and AD – values showed a trend of reaching an asymptote for each RC 4% and 6% level with increasing density. For all RC levels, the variables attenuation and its related terms showed an abrupt drop in

values at ND 0.60. The variables IRm, IRc, and Z (AT and ATD were approaching constant) tended to level off beyond ND 0.60 and 0.80 levels, and also beyond RC 4% level. This suggests that the nature of a better bond and material compactness existed beyond ND 0.60 enhances the transmissivity of the NCU parameters.

Table 4.1. Average values of the specimen mean densities and NCU measurements.

Resin Content RC (%)	Nominal Density ND (g/cm^3)	Average Density AD (g/cm^3)	Noncontact Ultrasonic variables V (km/s)	A (-dB)	Ac (-dB)	Transm. Coef.	Z ($Gg/s.m^2$)	ATD ($dB.cm^3$/ mm.g)	AT (dB/mm)
2%	0.40	0.476	0.389	132.9	47.2	1011.8	0.186	22.7	10.75
		(7.7)	(54.1)	(11.9)	(34.8)	(70.2)	(56.0)	(13.4)	(11.9)
	0.60	0.686	0.494	76.8	23.6	50.1c	0.339	9.3	6.32
		(7.2)	(24.6)	(9.9)	(29.9)	(40.7)	(25.0)	(12.6)	(9.9)
	0.80	0.894	0.673	61.2	8.5	21.5c	0.603	5.6	5.04
		(4.5)	(8.3)	(4.2)	(27.8)	(13.5)	(10.7)	(5.2)	(4.5)
4%	0.40	0.482	0.447	113.8	37.9	350.4	0.216	19.7	9.47
		(6.9)	(49.2)	(10.7)	(24.8)	(54.9)	(50.5)	(13.1)	(11.0)
	0.60	0.691	0.785	61.6	10.2	22.0d	0.544	7.4	5.10
		(6.5)	(10.5)	(4.6)	(28.0)	(14.8)	(13.9)	(7.9)	(4.5)
	0.80	0.887	0.673	58.8	7.3	19.1d	0.597	5.5	4.83
		(5.2)	(10.4)	(4.9)	(39.1)	(15.2)	(12.6)	(6.3)	(5.5)
6%	0.40	0.479	0.567	91.1	37.6	105.5	0.277	16.0	7.59
		(9.3)	(46.7)	(10.4)	(25.4)	(44.6)	(51.6)	(17.5)	(10.8)
	0.60	0.699	0.845	61.7A	10.2b	22.0e	0.592f	7.4	5.19g
		(4.9)	(12.5)	(4.0)	(24.2)	(12.7)	(14.2)	(7.2)	(3.8)
	0.80	0.899	0.638	62.8A	9.5b	23.5e	0.573f	5.6	5.07g
		(4.4)	(9.5)	(5.3)	(35.1)	(17.2)	(9.5)	(4.9)	(5.2)

For each RC level, reject Ho: $\mu_{.4}= \mu_{.6}=\mu_{.8}$ ($p < 0.01$ for $F(2, 267)$) for each UT variable
a, b, c, e, f, g = p-value > 0.12 not significantly different by $F(1, 267)$ test
( ) = Coefficient of Variation (CV%) of 90 specimens within a board
V=Velocity (km/s); A = Attenuation in IRm (-dB); Ac = Attenuation in IRc (-dB);
Transm. Coef. = Transmission coefficient; Z=Acoustic impedance ($Gg/(s.m^2)$);
ATD = Attenuation coefficient ($dB.cm^3/mm.g$) corrected for density and thickness;
AT = Attenuation coefficient (dB/mm) corrected for thickness

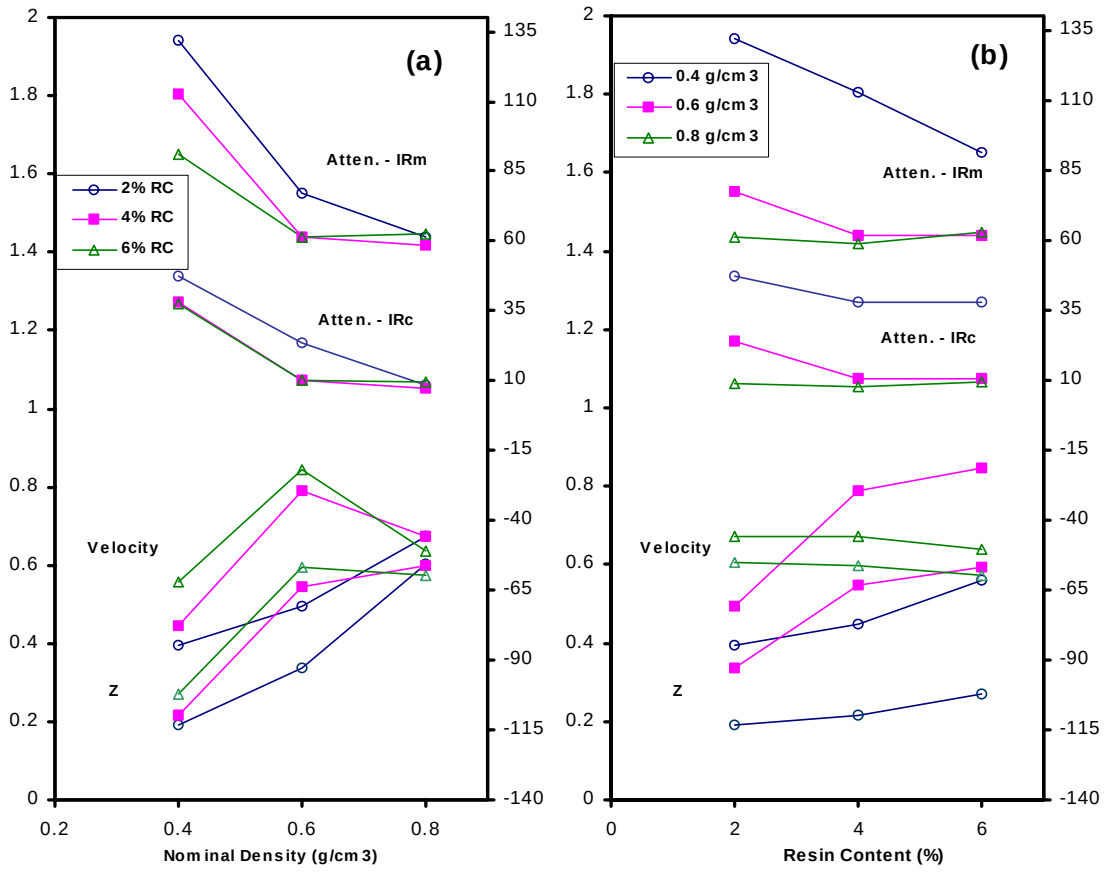

Fig. 4.2. Scatter plots of NCU variables attenuation (IRm and IRc), velocity, and impedance (Z) as a function of Nominal Density (a) and Resin Content (b) levels.

On the other hand, the high density variability in the lower density (ND 0.40) influenced the variability of the NCU measurements. **Fig. 4.3** shows the exponential decay trends of the transmissivity coefficient values that were approaching constant with increasing density and RC levels. The transmissivity coefficient curves are parallel (p=0.8219) in between ND 0.60 and 0.80 for all RC levels (**Table 4.2**). The IRc trend is parallel in between ND 0.40 and 0.80

(p=0.1834) for all RC levels, and in between RC 4% and 6% (p=0.1368) for all ND levels.

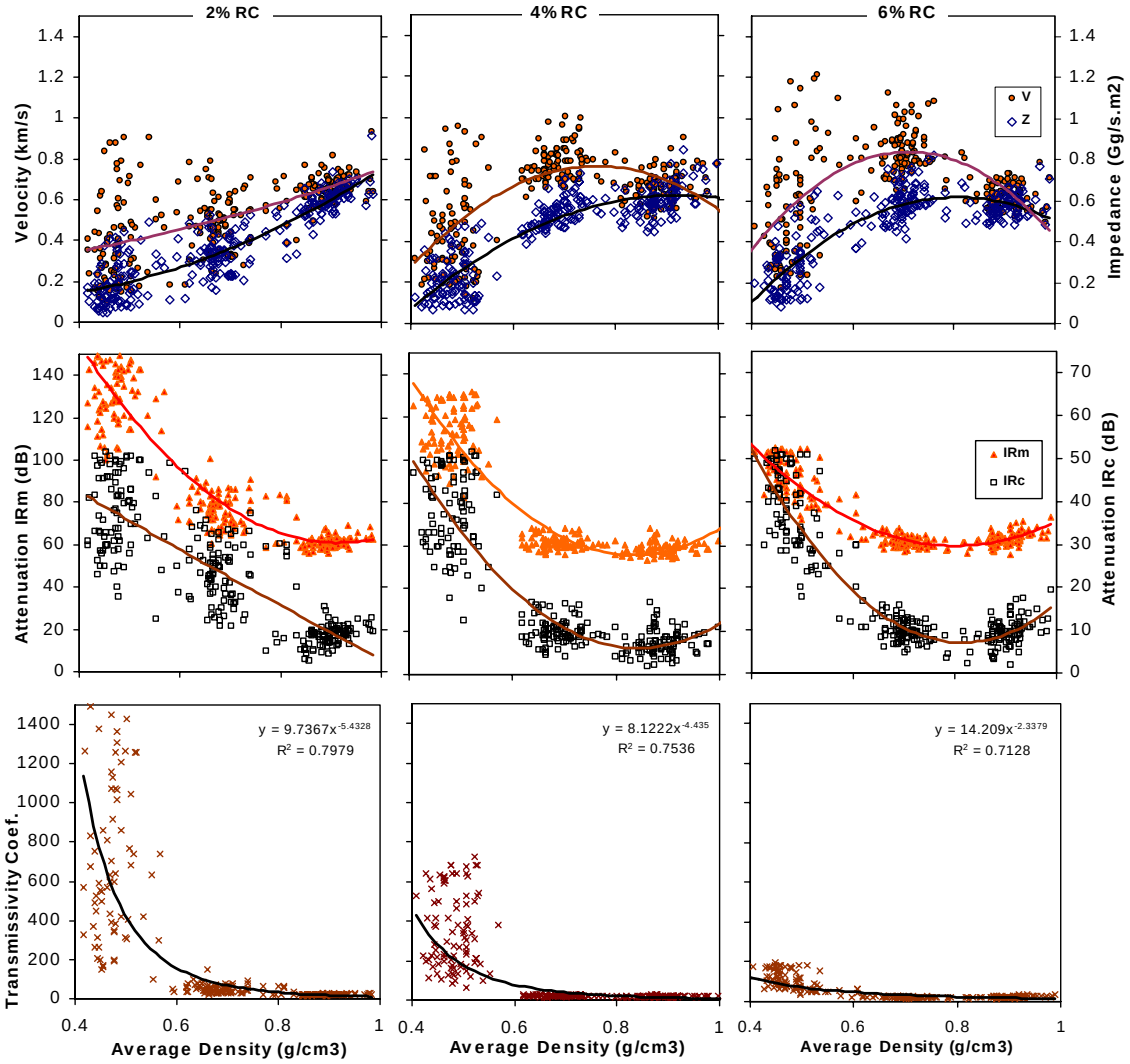

Fig. 4.3. Regressions of NCU variables velocity/impedance, attenuation (IRm, IRc), and transmissivity coefficient as a function of average density for boards at 2%, 4%, and 6% RC levels.

Table 4.2. Comparisons of resin content (RC) and nominal density (ND) to NCU measurements.

RC %	ND (g/cm3)	LSMean	CV(%)	P-VALUE *							
--------- *Velocity (km/s)* ----------											
2	0.4	0.389	(54.1)	2; 0.4	<.0001	<.0001	0.0103			<.0001	
2	0.6	0.494	(24.6)		2; 0.6	<.0001		<.0001			<.0001	
2	0.8	0.673	(8.3)			2; 0.8			0.9717			0.1129
4	0.4	0.447	(49.2)				4; 0.4	<.0001	<.0001	<.0001		
4	0.6	0.785	(10.5)					4; 0.6	<.0001		0.0078	
4	0.8	0.673	(10.4)						4; 0.8			0.1211
6	0.4	0.567	(46.7)	2%	**			0.4	**	6; 0.4	<.0001	0.0051
6	0.6	0.845	(12.5)	<.0001	4%			<.0001	0.6		6; 0.6	<.0001
6	0.8	0.638	(9.5)	<.0001	<.0001	6%		<.0001	<.0001	0.8		6; 0.8
------ *Attenuation IRm (-dB)* -------												
2	0.4	132.9	(11.9)	2; 0.4	<.0001	<.0001	<.0001			<.0001		
2	0.6	76.8	(9.9)		2; 0.6	<.0001		<.0001			<.0001	
2	0.8	61.2	(4.2)			2; 0.8			0.0475			0.1689
4	0.4	113.8	(10.7)				4; 0.4	<.0001	<.0001	<.0001		
4	0.6	61.6	(4.6)					4; 0.6	<.0001		0.9681	
4	0.8	58.8	(4.9)						4; 0.8			0.0008
6	0.4	91.1	(10.4)	2%	**			0.4	**	6; 0.4	<.0001	<.0001
6	0.6	61.7	(4.0)	<.0001	4%			<.0001	0.6		6; 0.6	0.1953
6	0.8	62.8	(5.3)	<.0001	<.0001	6%		<.0001	<.0001	0.8		6; 0.8
------- *Attenuation IRc (-dB)* -------												
2	0.4	47.2	(34.8)	2; 0.4	<.0001	<.0001	<.0001			0.7582		
2	0.6	23.6	(29.9)		2; 0.6	<.0001		<.0001			<.0001	
2	0.8	8.5	(27.8)			2; 0.8			0.2214			0.2831
4	0.4	37.9	(24.8)				4; 0.4	<.0001	<.0001	0.3520		
4	0.6	10.2	(28.0)					4; 0.6	0.0014		0.9590	
4	0.8	7.3	(39.1)						4; 0.8			0.0218
6	0.4	37.6	(25.4)	2%	**			0.4	**	6; 0.4	<.0001	<.0001
6	0.6	10.2	(24.2)	<.0001	4%			<.0001	0.6		6; 0.6	0.4105
6	0.8	9.5	(35.1)	<.0001	0.1368	6%		0.1834	<.0001	0.8		6; 0.8
--------*Transmissivity Coef.*--------												
2	0.4	1011.8	(70.2)	2; 0.4	<.0001	<.0001	<.0001			<.0001		
2	0.6	50.1	(40.7)		2; 0.6	0.6405		0.4441			0.4441	
2	0.8	21.5	(13.5)			2; 0.8			0.9481			0.9568
4	0.4	350.4	(54.9)				4; 0.4	<.0001	<.0001	<.0001		
4	0.6	22.0	(14.8)					4; 0.6	0.8603		0.9999	
4	0.8	19.1	(15.2)						4; 0.8			0.9050
6	0.4	105.5	(44.6)	2%	**			0.4	**	6; 0.4	<.0001	<.0001
6	0.6	22.0	(12.7)	<.0001	4%			<.0001	0.6		6; 0.6	0.7205
6	0.8	23.5	(17.2)	<.0001	<.0001	6%		<.0001	0.8219	0.8		6; 0.8

( ) = Coefficient of Variation (CV%) of 90 specimens within a board.

* p-values for pairwise comparisons F(1, 801) of the RC [ND] at each ND [RC] level using a two-factor ANOVA.

** Within the bordered are p-values for pairwise F(2, 801) tests for parallel RC curves and parallel ND curves.

4.3.2. Regressions on Average Density

Scatter plots of the NCU properties versus AD revealed a quadratic relationship for each RC (as was the case in an earlier study on aspen OSB by Vun et al. 2003a). Accordingly, a simultaneous regression model with 810-9=801 error degrees of freedom, allowing different least squares quadratic functions for the three RC's, was fit to each NCU variable. For each NCU variable (**Table 4.3**), all three quadratic coefficients were highly significant ($p<.0001$), and the quadratic curves were found not to be parallel ($p<.0001$). Thus, inherently different quadratics are required to describe the relationship of each NCU variable to AD at the three RC's. The three quadratic curves were superimposed as scatter plots of the data for the NCU variables velocity, impedance, attenuation (IRm and IRc), and transmissivity coefficient against average density as in **Fig. 4.3**.

4.3.2.1. Velocity/Impedance versus AD

For each RC level, the quadratic curve of each velocity and impedance rose to its apex and then fell (**Fig. 4.3**). The fall was more pronounced as RC increased, since velocity/impedance transmissivity was very sensitive to density changes caused by diminishing void volume as void spaces were "filled up" creating better bonding at higher RC levels. The high variability of the velocity due to interfacial impediments was evidenced by the low R^2 values (≤ 0.42). Across the RC levels (**Table 4.3b**), the impedance followed the similar intersection trends of the velocity. The velocity RC 2% curve intersected the RC 4% (6%) curve at AD values 0.44 and 0.92 g/cm^3 (0.40 and 0.90 g/cm^3). The velocity RC 4% curve

intersected the RC 6% curve at AD values 0.23 and 0.86 g/cm^3. The corresponding velocity ranged from 0.35 to 0.68 km/s, with 0.73 km/s being the maximum for RC 4% and 6% intersection.

Table 4.3. Least squares quadratic curves UT = $B_2(AD)^2 + B_1(AD) + B_0 + \varepsilon$ and points of intersection (by RC levels).

UT variables	RC %	B_2	B_1	B_0	R^2
(a) Least Squares Curves Quadratic Function					
Velocity	2%	0.39	0.12	0.24	0.39
	4%	-3.74	5.71	-1.41	0.42
	6%	-4.93	7.00	-1.65	0.41
Impedance	2%	0.99	-0.4	0.14	0.82
	4%	-2.04	3.8	-1.11	0.79
	6%	-3.08	5.0	-1.39	0.75
Attenuation IRm	2%	356.1	-650.4	357.8	0.83
	4%	444.4	-740.5	364.1	0.85
	6%	292.6	-469.1	247.3	0.88
Attenuation IRc	2%	6.51	-74.94	71.44	0.70
	4%	231.8	-390.7	170.7	0.79
	6%	262.7	-427.7	181.2	0.88

(b) AD points of Intersection of Least Squares Curves*
(corresponding predicted UT values appear in brackets)

Velocity	2%	0.92(0.68)	0.90(0.66)
	0.44(0.37)	4%	0.86(0.73)
	0.40(0.35)	0.23(0.28)	6%
Impedance	2%	0.92(0.62)	0.89(0.59)
	0.45(0.17)	4%	0.85(0.61)
	0.42(0.16)	0.32(0.11)	6%
Attenuation IRm	2%	0.08(311)	1.97(461)
	0.94(61.2)	4%	1.07(79.9)
	0.88(61.2)	0.72(61.2)	6%
Attenuation IRc	2%	0.48(37.2)	0.48(37.3)
	0.92(7.69)	4%	0.46(40.3)
	0.90(9.13)	0.74(8.49)	6%

* $AD = (-D_1 + -SQRT(D_1^2 - 4*D_2*D_0))/2*D_2$
where $D_i = (B_{i,a} - B_{i,b})$ $i = 0, 1, 2$

4.3.2.2. Attenuation versus AD

For each RC level, the least squares quadratic curve for attenuation (both IRm and IRc) decreased with increasing density, with only a slight increase for RC 4% and 6% levels (**Fig. 4.3**). Note the linear trend of attenuation IRc at the RC 2% level. Comparing the intersection points of the curves across RC levels (**Table 4.3b**), the attenuation IRm curves were wider, resulting in out of data range intersections, than the attenuation IRc. The high R^2 values (≥70) for both attenuation IRm and IRc can provide a complementary gauge to diagnose internal structure of materials.

4.3.3. Density Prediction

A calibration procedure was developed to predict the AD from each of the NCU measurements. For each RC level, the plot of each NCU variable versus AD revealed a quadratic relationship as shown in **Fig. 4.4** for each of the six plots. Note that a data scheme was adopted for plotting the NCU variables. For each plot, Data1 consisted of ND 0.4, 0.6, and 0.8 groups; Data2 of 0.4 and 0.6 only; and Data3 of 0.6 and 0.8 only. The R^2 values for Data1 in both velocity and attenuation IRm decreased with increasing RC levels. This is in contrast with Data2, where the R^2 values at RC 4% and 6% were about the same. A univariate regression model, $AD=Bo+Ln(X)+X+X^2+Ln(X)*X+Ln(X)*X^2$, was performed for each NCU X variable (i.e., Velocity, IRm, Tr, IRc) in each data scheme and panel type. For all data scheme, the velocity models had the lowest R^2 values (≥0.24) associated with possibly high prediction errors. The attenuation and its

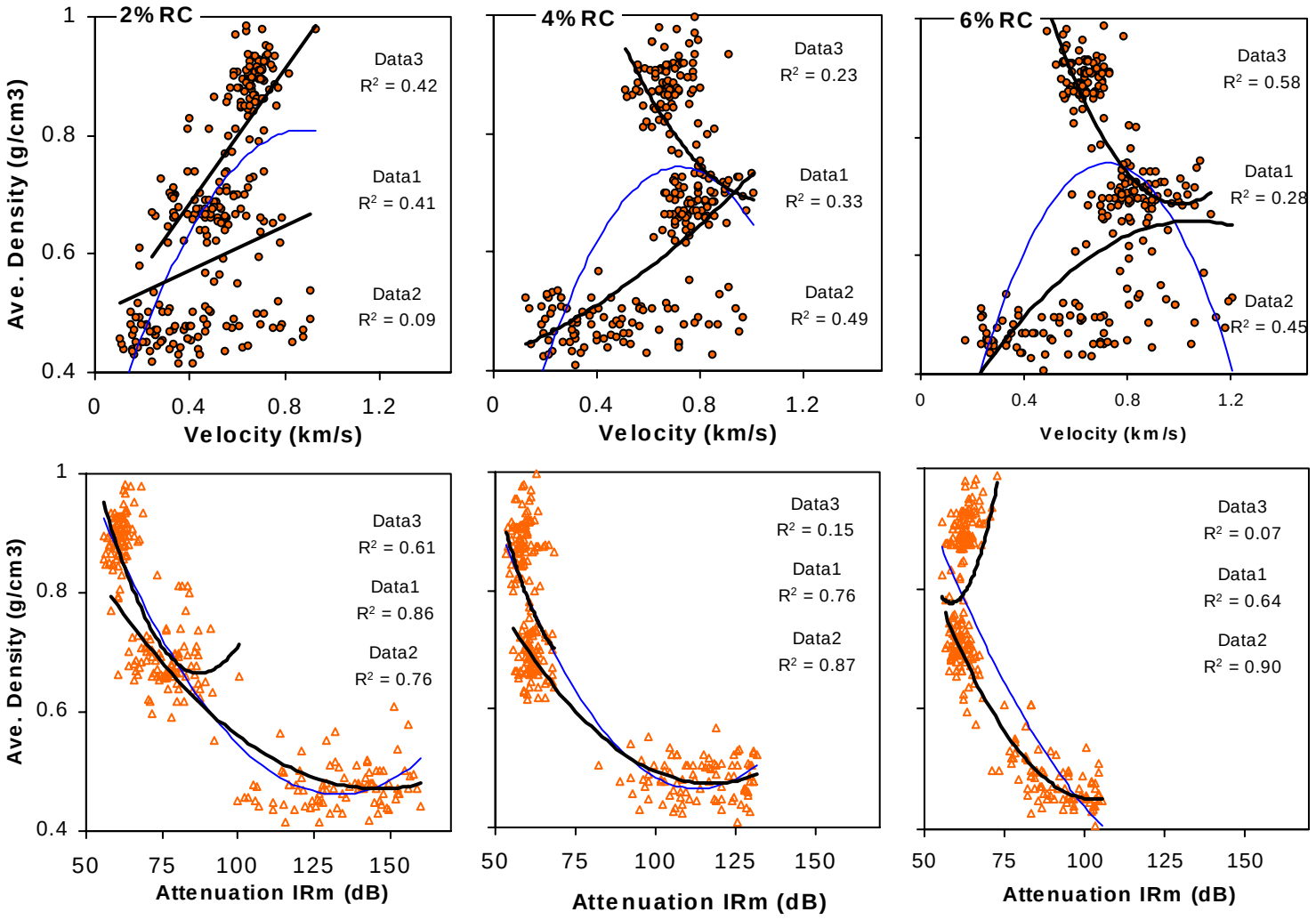

Fig. 4.4. Calibration regressions of measured average density as a function of NCU predictors velocity and attenuation IRm by Data scheme.

related-terms models produced better R^2 values (≥0.69), but were limited to Data1 and Data2. The spatial density prediction using the attenuation variable are discussed in the next section.

In addition, the total percent out-of-limits (POFL) of the predicted values (i.e., the predicted values within a panel that are not within 10% of the panel average of the measured AD's) based on the univariate regression models were generally high. For example, when the model for velocity was fit to all of the data, the POFL for the predicted values exceeded 90% for all panels of RC and ND combinations.

To improve the POFL predicted values, logarithmic, square, and/or product functions of the original NCU variables were included to form new models. The General Model having 10 predictor terms for each of the three RC levels is

$$Y_{ij} = B_0 + \sum_{k=1}^{3} A_k Ln(X_{ijk}) + \sum_{k=1}^{3} C_k X_{ijk} + \sum_{k=1}^{3} D_k X_{ijk}^2 + \sum_{k=1}^{3} E_k Ln(X_{ijk}) * X_{ijk} + \sum_{k \neq k'} \sum F_k Ln(X_{ijk}) * X_{ijk'} + \varepsilon_{ij} \quad \textbf{(4.6)}$$

where Y_{ij} is the AD measurement for specimen *ij* obtained from the grid *i* and *j*, X_{ijk} is the NCU measurement (k=1 Velocity, k=2 Attenuation) for specimen *ij*, ε_{ij} is the random error term, B_o is the intercept, and A_k, C_k, D_k, E_k, F_k are the coefficients.

For each of the three data sets, the final models were obtained from the backward elimination procedure using least squares regression. Backward elimination started with the full model and removed variables one at a time until

all variables remaining are significant at the 0.10 level. All of the final models obtained had significant variable coefficients.

Based on the standardized coefficient values in **Table 4.4**, the velocity-attenuation combination formed complementary terms in estimating the AD and contributed more profoundly to the General Models for Data1 at RC 2%. However, the velocity reduced its influence as the RC levels increased, while attenuation maintained its impact throughout. As is the case for Data2, attenuation was maintaining its significance throughout RC levels. As seen in Data3, velocity contributed profoundly at RC 2% and 4%, while attenuation was dominant only at RC 6% level. This suggests that the velocity predictor was affected by weak bonding or physical impediments as in the low RC level; whereas, the attenuation provided good complementary measures of the transmissivity of ultrasonic energy.

The R^2 values increased with increasing RC levels for Data2. For Data1 and Data3, however, R^2 values are the lowest at RC 4%. The predicted residual sum of squares (PRESS) was obtained as a measure of prediction error for each of the final regression models (Neter et al. 1996). The General Models exhibited a decreasing trend in the square root PRESS as RC levels increased for Data2. For Data1 and Data3, the root PRESS values maximized at RC 4% level (**Table 4.4**). The R^2 trends are more in contrast (rather than similar) to the root PRESS trends.

Table 4.4. General Models for predicting density (AD) as a function of NCU variables: V, A = Velocity (km/s), Attenuation IRm (-dB).

RC	Variable	Est.	SE	Pr>|t|	Std. Est.	R2	RPress	RC	Variable	Est.	SE	Pr>|t|	Std. Est.	R2	RPress
--------Data1---------								--------Data2---------							
2%	Bo	-5.77	2.28	0.0121	0.0	0.89	0.98	2%	Bo	-11.14	2.25	<.0001	0.0	0.80	0.71
	Ln(V)	-0.44	0.17	0.0102	-1.1				Ln(A)	4.01	0.72	<.0001	10.4		
	Ln(A)	1.98	0.67	0.0036	3.8				A	-0.09	0.01	<.0001	-24.5		
	V	5.67	1.30	<.0001	6.0				V2	-0.18	0.11	0.0895	-0.3		
	A	-0.04	0.01	0.0005	-7.9				A2	0.00	0.00	<.0001	13.3		
	A2	0.00	0.00	<.0001	5.0				Ln(A)*V	0.04	0.02	0.0622	0.3		
	Ln(V)*A	0.00	0.00	0.0051	1.4			4%	Bo	0.72	0.11	<.0001	0.0	0.89	0.51
	Ln(A)*V	-1.18	0.27	<.0001	-5.2				V	1.76	0.36	<.0001	3.8		
4%	Bo	0.73	0.86	0.3972	0.0	0.77	1.35		A2	0.00	0.00	0.0007	2.0		
	V	-6.45	2.36	0.0066	-7.5				Ln(A)*V	-0.37	0.08	<.0001	-3.2		
	V2	2.70	1.63	0.0996	3.6				Ln(A)*A	0.00	0.00	0.0034	-2.1		
	A2	0.00	0.00	<.0001	5.8			6%	Bo	1.57	0.08	<.0001	0.0	0.92	0.46
	Ln(V)*V	-4.20	2.39	0.0798	-2.0				Ln(V)	0.26	0.06	<.0001	1.0		
	Ln(V)*A	-0.01	0.00	0.0533	-2.0				A2	0.00	0.00	<.0001	3.1		
	Ln(A)*V	1.34	0.46	0.0041	6.3				Ln(V)*A	0.00	0.00	<.0001	-0.9		
	Ln(A)*A	-0.01	0.00	<.0001	-8.7				Ln(A)*A	-0.01	0.00	<.0001	-4.1		
6%	Bo	-112	9.05	<.0001	0.0	0.84	1.22	--------Data3---------							
	Ln(V)	-5.14	0.62	<.0001	-10			2%	Bo	-1.64	0.83	0.0505	0.0	0.73	0.82
	Ln(A)	34.1	3.29	<.0001	37				Ln(A)	0.76	0.18	<.0001	0.9		
	A	-0.94	0.08	<.0001	-79				V	11.7	2.11	<.0001	13.5		
	V2	11.1	1.74	<.0001	18				V2	-3.57	1.97	0.0723	-4.5		
	A2	0.00	0.00	<.0001	40				Ln(V)*V	3.93	2.08	0.0612	1.8		
	Ln(V)*V	-24.4	3.67	<.0001	-17				Ln(A)*V	-2.10	0.30	<.0001	-9.6		
	Ln(V)*A	-0.01	0.00	0.0164	-1.6			4%	Bo	41.6	21.3	0.053	0.0	0.28	1.26
	Ln(A)*V	1.81	0.29	<.0001	8.7				Ln(V)	19.4	9.42	0.0404	23.3		
									V	-76.6	25.7	0.0033	-67.2		
									A2	0.00	0.00	0.0072	-4.1		
									Ln(V)*V	21.7	12.6	0.0876	13.5		
									Ln(V)*A	-0.07	0.03	0.039	-4.5		
									Ln(A)*V	9.73	3.64	0.0082	37.2		
								6%	Bo	-323	151	0.0339	0.0	0.66	0.87
									Ln(V)	9.37	2.66	0.0005	15.6		
									Ln(A)	132	57.1	0.0226	58.5		
									A	-3.94	1.80	0.0302	-110		
									A2	0.02	0.01	0.0287	55.0		
									Ln(V)*V	21.3	5.36	0.0001	20.1		
									Ln(V)*A	0.08	0.03	0.0027	8.8		
									Ln(A)*V	-8.59	2.25	0.0002	-44.9		

4.3.4. Average Density Validation

The EN300 panel standard allows for a 10% upper and lower variation from the average of the measured AD's within a panel. Control limits for the measured AD's were evaluated and given in **Table 4.5** for each of the nine panels manufactured in this study. Note that for ND 0.40 panels, POFL increased as RC increased with all three POFL's exceeding the allowed 10% level. For the ND

0.60 panels, POFL decreased as RC increased with only the RC 2% panel having marginally out of limits (10%). For the ND 0.80 panels, all RC levels had POFL less than 10%. Using our nine sets of control limits, it appears necessary to manufacture at least 0.60 g/cm^3 panels to conform to the EN300 standard.

Table 4.5. Summary of the out-of-limits percentages for AD measured and predicted values.

Test Panels			Control	Out-of-Limits			
RC	ND	AD	Limits	Measured	General Model		
(%)	(g/cm^3)	(g/cm^3)	±10%	Data	Data1	Data2	Data3
	0.40	0.476	[.429, .524]	12.2%	27.8%	14.1%	
2%	0.60	0.686	[.618, .755]	10.0%	10.0%	10.1%	8.9%
	0.80	0.894	[.805, .984]	4.4%	2.2%		2.2%
				R^2	0.89	0.80	0.73
				√PRESS	0.98	0.71	0.82
	0.40	0.482	[.434, .531]	14.4%	40.0%	22.2%	
4%	0.60	0.691	[.622, .760]	8.9%	33.3%	10.1%	18.9%
	0.80	0.887	[.798, .976]	7.8%	5.6%		16.7%
				R^2	0.77	0.89	0.28
				√PRESS	1.35	0.51	1.26
	0.40	0.479	[.432, .527]	18.9%	47.8%	13.3%	
6%	0.60	0.699	[.629, .769]	5.6%	23.3%	10.1%	9.3%
	0.80	0.899	[.810, .989]	4.4%	15.6%		7.2%
				R^2	0.84	0.92	0.66
				√PRESS	1.22	0.46	0.87

Control Limits: within 10% deviation from individual measured AD's obtained from each test panel.
Out-of-limits: percent of 90 specimens not within Control Limits.
Data1: fit to ND's 0.4, 0.6, and 0.8 (270 specimens total).
Data2: fit to ND's 0.4 and 0.6 only (180 specimens total).
Data3: fit to ND's 0.6 and 0.8 only (180 specimens total).

For all final models, the predicted AD's were *in situ* matched with the measured AD's for each test panel. The POFL for the predicted values in each panel using the EN300 panel control limits was computed for each model and reported in **Table 4.5** for each data set. Generally, the models for Data1 produced greater overall prediction errors (PRESS values) than those for Data2 or Data3. For the model using Data1, the smallest POFL of 2.2% was attained at RC 2% ND 0.80. For the model applied to Data2, the minimum POFL of 10.1% was attained at ND 0.60 for all RC levels. When restricted to Data3, the models were within the 10% control limits for RC 2% and 6%. The conformity towards RC 2% indicates that the models required a velocity and attenuation combined form and at least ND 0.60 g/cm^3 for adequate density estimation using ultrasonic techniques.

The absolute values of the measured densities to the predicted ones were plotted as one-dimensional control charts in **Fig. 4.5** for the out-of-limit points in the three ND levels. The predicted out-of-limit AD points appeared coherently similar through the width dispersion as those measured AD's. The out-of-limit points may also reduce in number due to the relatively larger limits of the ND levels.

In trying to replicate the natural fluctuation of the density variations, the smoothing effects of the regressions may result in some discrepancies. Spatially distributed predicted AD's generated by the different models were investigated and validated over the whole panel. The predicted densities by the General Models for panel RC 6% ND 0.60 applied in Data2 were compared spatially against the

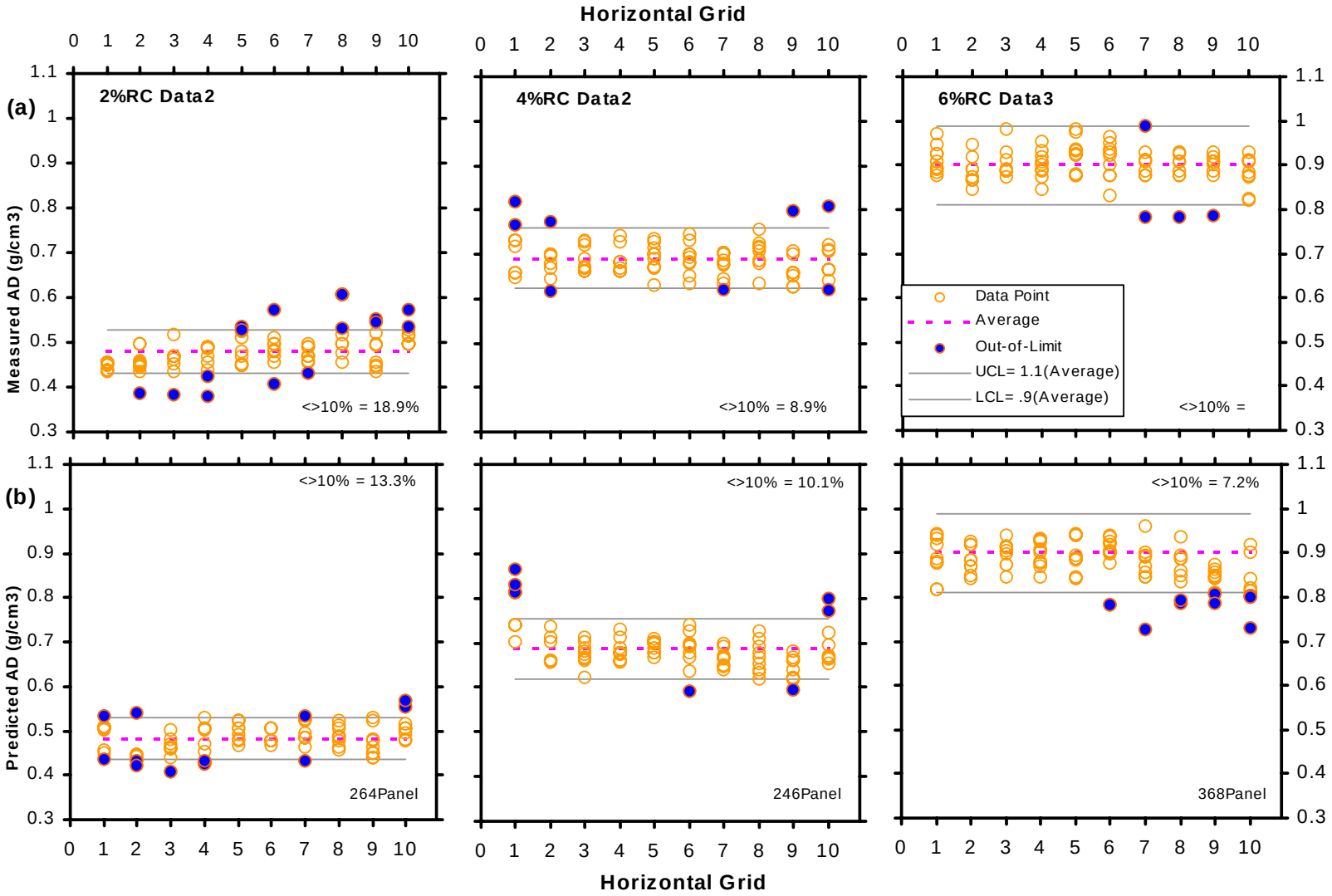

Fig. 4.5. Control charts indicating the out-of-limits points for AD's measured (a) and predicted (b) for NCU method.

measured AD's in three-dimensional, contour, out-of-limit points as plotted in **Fig. 4.6**. The predicted density of the General Model generally appeared reasonably distributed and resembled well to the measured density. As compared to the measured out-of-limit points, the predicted out-of-limit plot appear to capture the extreme lower out-of-limit point, which apparently had the high and low out-of-limit points smoothened out. As compared with the plots in **Fig. 4.7** for panel RC 6% ND 0.80 applied in Data3, the predicted out-of-limit plot appears to capture the lower limit points, eliminated the higher points when compared to the measured out-of limit points. As is the case in Data1 (**Fig. 4.8a**), the predicted out-of-limit plot appears to break the measured out-of-limit peak as two high limit peaks.

On the other hand, the univariate model of using only attenuation IRm (**Fig. 4.8b**) produced the approximately similar density distribution as of the measured densities and the general model predicted densities. From the out-of-limit plots, the univariate model captured most of the higher peaks of the limit points, of which neither the measured or general model predicted plots did.

Taking advantage of the higher correlation of attenuation-density in Data1 and Data2, a scaling scheme of the control limits presents a relativity approach. **Fig. 4.9** shows the comparison of the measured density distribution and the different scaling of the attenuation IRm values. From the scaling search, the 9% scale produced the same out-of-limits points as the univariate model (**Fig. 4.8b**). The prediction of the density generally improved with increasing ND levels.

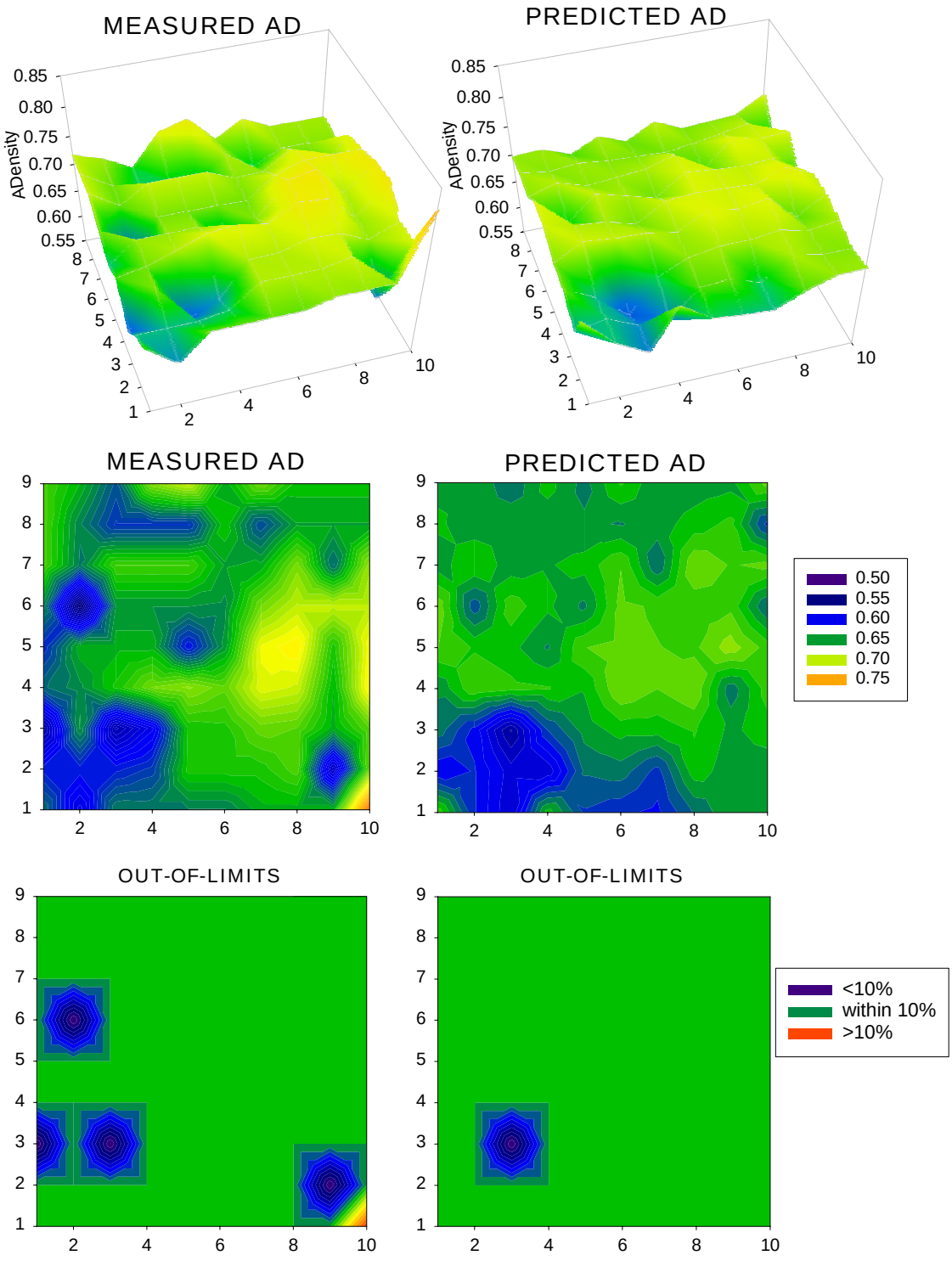

Fig. 4.6. 3-D, contour, and out-of-limits plots of AD comparing the measured and predicted AD's by General Model for RC 6% at ND 0.60 g/cm^3 applied in Data2.

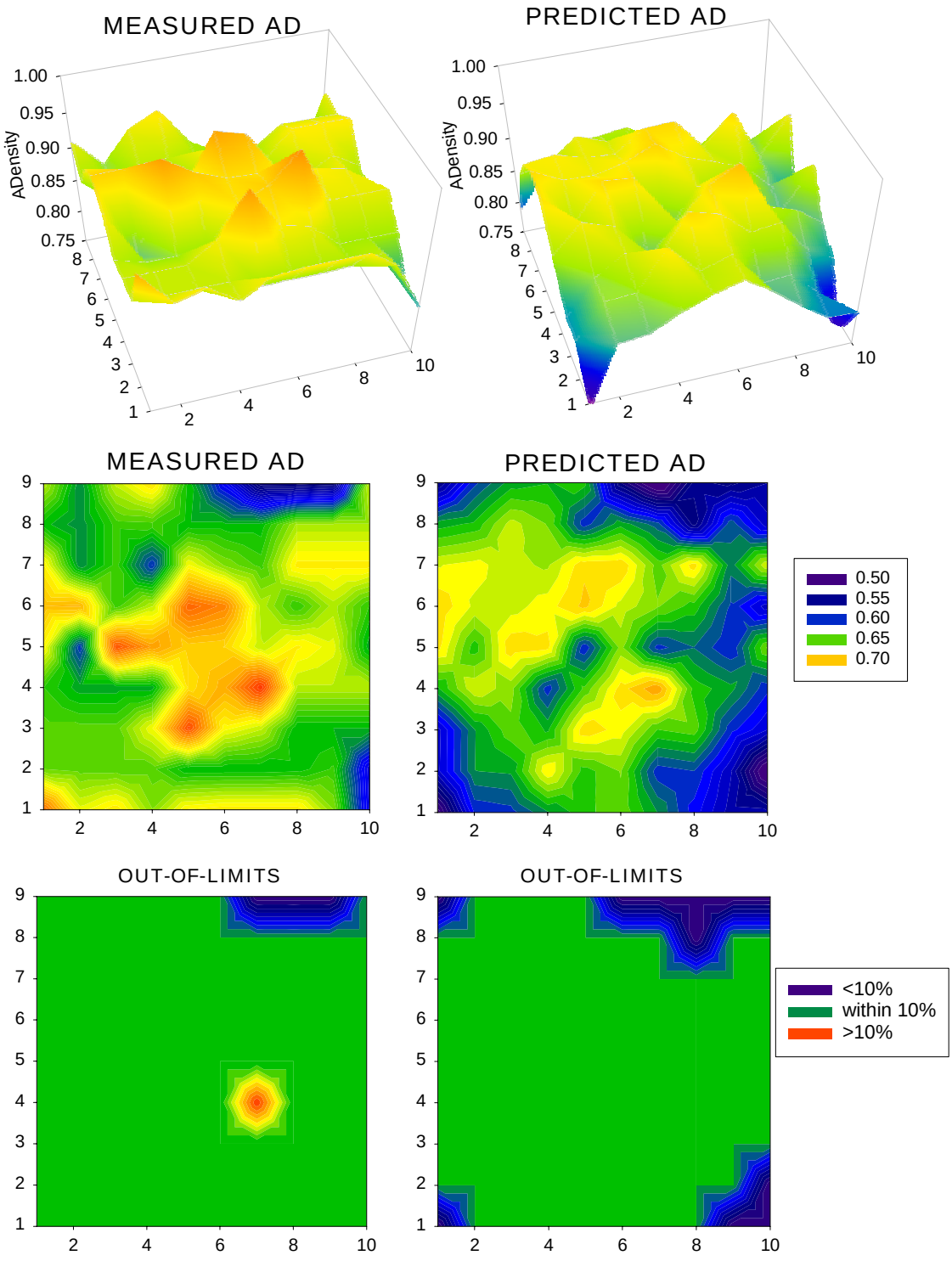

Fig. 4.7. 3-D, contour spatial, and out-of-limits plots of AD comparing the measured and predicted AD's by General Model for RC 6% at ND 0.80 g/cm^3 applied in Data3.

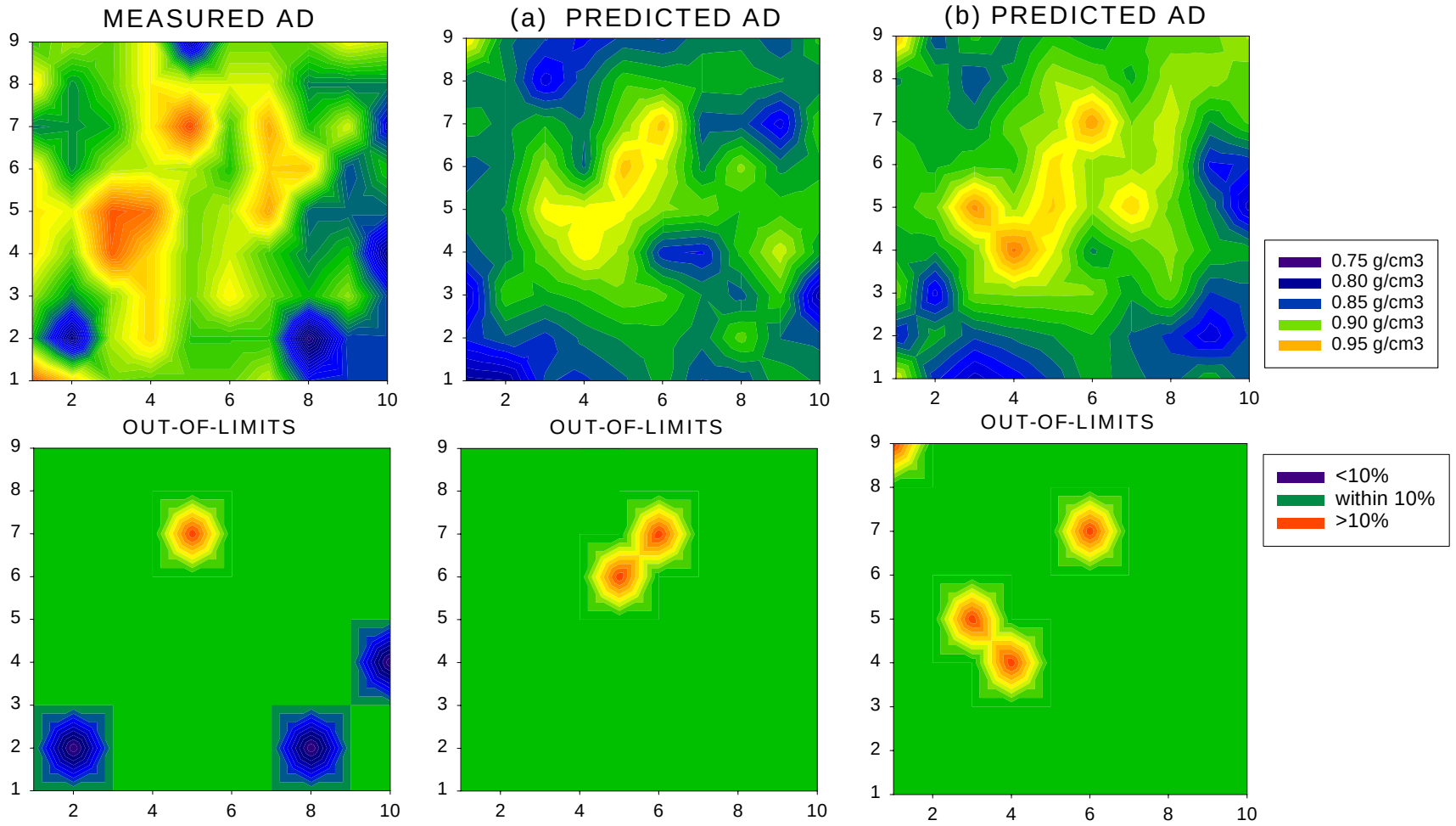

Fig. 4.8. Contour spatial and out-of-limits plots of AD comparing the distribution of the measured and predicted AD's by General Model (a), and by Univariate IRm Model (b) for RC 2% at ND 0.80 g/cm^3 applied in Data1.

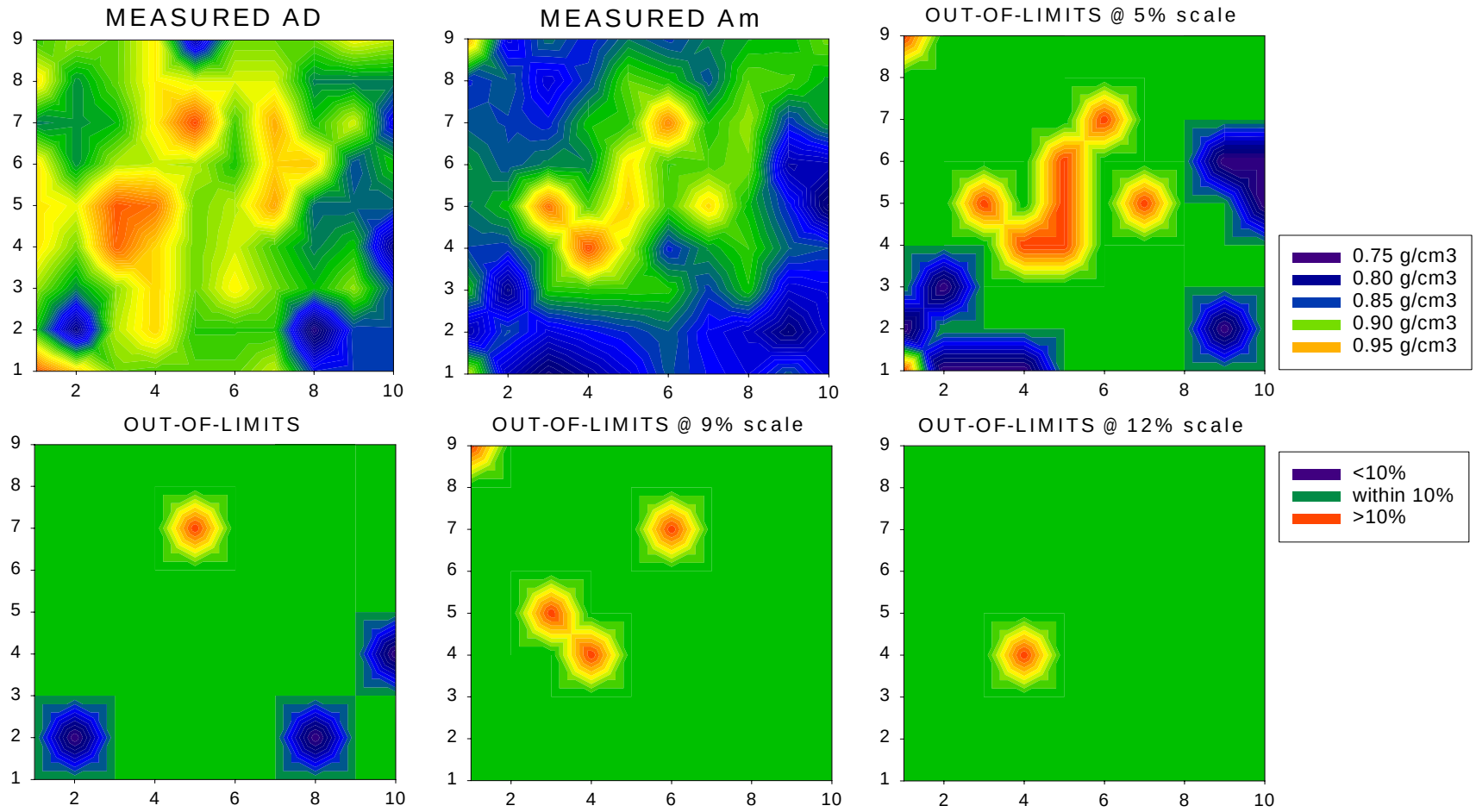

Fig. 4.9. Contour spatial AD plots of the measured AD's and measured attenuation with the respective out-of-limits spatial plots comparing each scaling of the control limits (5%, 9%, and 12%) for RC 2% at ND 0.80 g/cm^3 applied in Data1.

4.4. CONCLUSIONS AND RECOMMENDATION

Horizontal density variation is inherent in OSB due to embedded voids and the discretely different consolidated particle densities in the mat. The consistent horizontal density distribution is the key to determining the creep resistance and durability of wood composites. Non-contact ultrasonic technology is providing a valuable tool in defining the internal structure of typical wood composites.

The NCU variables revealed a curvilinear relationship with density. The high variability of the density in the ND 0.40 panels led to the high variability in the velocity measurements, which also indicated that velocity is affected by physical interfacial impediments in the low density panels. However, the transmissivity of attenuation was not affected by the nominal density and resin content levels and the data scheme; hence, attenuation is a significant NC variable to predict density in the panel. Based on the current calibration of the NCU system, the transmissivity coefficient approaching constant beyond ND 0.60 g/cm^3 and RC 4% levels indicated the threshold for the NCU monitoring of density in oriented strandboard.

A combination form of ultrasonic predictors used for density modeling across the RC levels was effective. The models were validated by a spatial cohesive conformation of the predicted density to the measured density as well as their percent out-of-limit points. Other than the density prediction of the General Models, the attenuation univariate modeling and/or the scaling of the attenuation values could also be an effective alternative. The density prediction improved for

panels with higher RC and higher ND levels. Based on the EN300 standard, models validated in the control charts indicated that only 0.40-g/cm^3 panels did not meet the standard, primarily because of the inherently high coefficient of variation of density. The validation results further indicated that at least ND 0.60 g/cm^3 OSB panel satisfied the ±10% limitation for this horizontal density variation study.

The NCU investigation of the horizontal density is convenient and effective for monitoring quality of a large panel. Notwithstanding the benefits of other ultrasonic methods, this study acknowledges the sensitivity of NCU responses to match local representation of internal constituents of the wood composites. With its state-of-art and unique features, NCU offers an alternative approach in wood science research and development. Further study in optimal sample-to-transducer size for the search of improving the sampling effectiveness and accuracy (or perhaps in voids investigation) is hereby recommended.

4.5. REFERENCES

Beall, C. F. 2002. Overview of the use of ultrasonic technologies in research on wood properties. Wood Sci. Technol. (36): 197-212.

Bhardwaj, M.C. 2002. Non-destructive evaluation. *In* Mel Schwartz, ed. Encyclopedia of Smart Materials volume 2:690-714. John Wiley & Sons, Inc. New York.

Bucur, V., M.P. Ansell, C.Y. Barlow, J. Pritchard, S. Garros, and X. Deglise. 1998. Physical methods for characterizing wood composite. Holzforschung (52):553-561.

Chen, L-H, and F.C. Beall. 2000. Monitoring bond strength development in particleboard during pressing, using acousto-ultrasonics. Wood Fiber Sci. 32(4): 466-477.

Kruse, K., C. Dai, and A. Pielasch. 2000. An analysis of strand and horizontal density distributions in oriented strand board (OSB). Holz Roh-Werkstoff 58(4):270-277.

Judd, N.C.W., and W.W. Wright. 1978. Voids and their effects on the mechanical properties of composites-An appraisal. SAMPE Journal, January/February: 10-14.

Lenth, C.A., and F.A. Kamke. 1996. Investigations of flakeboard mat consolidation. Part I. Characterization of the cellular structure. Wood Fiber Sci. 28(2): 153-167.

Neter, J., M.H. Kutner, C.J. Nachtsheim, and W. Wasserman. 1996. Applied Linear Statistical Models. 4th Ed. Irwin McGraw-Hill, Chicago:345-373.

Ross, R.J. and R.F. Pellerin. 1988. NDE of wood-based composites with longitudinal stress waves. Forest Prod. J. 38(5): 38-45.

Smith, C.D. 1982. Waferboard press closing strategies. Forest Prod.J. 32(3):40-45.

Steiner, P.R., and C. Dai. 1993. Spatial structure of wood composites in relation to processing and performance characteristics: Part 1. Rationale for model development. Wood Sci. Technol. (28):45-51.

Suchsland, O. 1962. The density distribution in flakeboard. Q. Bull., Michigan Agric. Expt. Sta., Michigan State Univ. 45(1):104-121.

Suchsland, O., and H. Xu. 1989. A simulation of the horizontal density distribution in a flakeboard. Forest Prod. J. 39(5): 29-33.

Suddarth, S.K. 1965. Detection of adhesive bond defects in the Polaris missile nose firing through mechanical impedance measurements. 2nd nondestructive testing of wood symposium; April; Pullman, WA: Washington State University: 267-285.

Szymani, Ryszard. 1985. An overview of scanning technology in sawmilling. *In* Pages I.1-I.33, Proceedings, 1st. International conference on scanning technology in sawmilling. October 10-11, San Francisco, CA, U.S.A.

Vogt, J.J. 1986. Longitudinal stress waves as predictors of internal bonding strength. 12th. Particleboard/composite materials symposium; March, WA: Washington State University.

Vun, R.Y, and F.C. Beall. 2002. Monitoring creep rupture in oriented strandboard using acoustic emission. *In* International NDT2002 Symposium, University of California, Berkeley, CA, 19-21 August, Forest Products Society, Madison, Wisconsin.

Vun, R.Y, Q. Wu, M.C. Bhardwaj, and G. Stead. 2003a. Ultrasonic Characterization of Structural Properties of Oriented Strandboard: Direct-Contact vs. Non-Contact methods. Wood Fiber Sci. 35(3) (*In-press*).

Vun, R.Y, Q. Wu, and C. Monlezun. 2003b. Ultrasonic Characterization of Horizontal Density Variations in Oriented Strandboard. Wood Fiber Sci. 35(3) (*In-press*).

Wolcott, M.P., A. Bozo, and J.D. Linville. 2001. Spatial variation in wood composites. *In* Proc. Of the Ibero-American Forest Products Conference. Univ. Bio-Bio, Conception, Chile.

CHAPTER 5. THROUGH-THICKNESS ULTRASONIC CHARACTERIZATION OF WOOD AND AGRICULTURAL-FIBER COMPOSITES

5.1. INTRODUCTION

World consumption of wood composites are expected to triple during the period 1996 to 2010 (FAO 1999) due to population and economic growth. The sobering U.S. population projection for 2100 accompanied by the decrease of forest area from 1.1 to 0.5 ha per capita (Bowyer and Stockmann 2001) makes reconstituted wood and fiber composites a sustainable building product for the foreseeable future. In the state of Louisiana, agriculture and forestry together, the second largest employer (LSU AgCenter 2002), generated 7.8 million tons of biomass wastes annually in the forms of bark, wood chips, sawdust, cotton gin trash, rice hulls and sugar bagasse (deHoop et al. 1997, Kleit et al. 1994). Converting biomass residue into particleboard is crucial to reduce the risk of environmental hazard and the pressure to exploit forestland for the supply of wood fiber (Russell 1996). Many agricultural composite panels are produced to standard (Chow 1976, Gertjejansen 1977, Hague et al. 1998, Kuo et al. 1998, Odozi et al. 1986, Youngquist et al. 1994), but their commercial utilization remains slow. Their properties in dimensional stability, long-term durability, and termite-attack (Grace 1996) can be improved and compared to other wood composites using the ultrasonic technique as presented in this chapter.

Desired product performance for a particular application can be achieved by design – combining appropriate processing and material variables in an industrial production system (Kelly 1977). With reconstituted wood materials, properties changes are studied at the fiber, particle, flake, or veneer level that make up the basic element for composite wood products. The type and distribution of the different basic particle sizes determined the composites properties and end-uses. Inherently, voids are embedded in the manufacture of all bio-based reconstituted panels, which affect the internal structure of each panel. The presence of voids in the mat causes in-plane density variation that reduces mechanical strength (Wu 1999). Vun et al. (2003) successfully evaluated the density variation of oriented strandboard (OSB) using a through transmission ultrasonic technique. Applicability of the technique to characterize other types of composites is highly desirable.

The study is generally aimed at differentiating panels made of different particle size using a direct contact ultrasonic characterization methodology, which may be a technological bridge to other composites. The specific objective was to assess the ultrasonic responses to density and internal bonding properties as affected by the different size particles in three typical panel types: aspen oriented strandboard (a structural panel utilizing hardwood flakes), western red cedar particleboard (a termite-toxic, granular particulated board), and bagasse particleboard (a fibrous particulated board).

5.2. PANEL MANUFACTURING

5.2.1. Aspen Oriented Strandboard

Aspen (*Populus tremuloides*) lumber was processed using a disc-type flaker to obtain 0.635x13x76 mm flakes. The flakes were dried to about 3% moisture content (MC) before being blended with wax and resin. The single-layer aspen OSB's were made in four nominal density (ND) levels (0.56, 0.72, 0.96, and 1.12 g/cm^3) and two resin content (RC) levels (4% and 6% based on ovendry weight and abbreviated as OSB14 and OSB16, respectively) using liquid phenol-formaldehyde (PF) resin and 0.5% wax. Two replication of boards were made for each ND/RC combination. Application of wax and resin was carried out in separate lines through air-atomizing nozzles inside the tumbling blender for about ten minutes. The single layer mat was formed with controlled alignment level. The 13x610x610 mm panels were prepressed to thickness prior to heating the mats for resin curing at 190^oC for 6 minutes. After hot pressing, the panels were conditioned and edge-trimmed.

5.2.2. Western Red Cedar Particleboard

Small diameter western red cedar (*Juniperus virginiana*) trees were chipped in the field using a drum chipper. Two types of chips were prepared from the whole trees; one including bark and branches, and the other only wood chips. The chips were shipped from Oklahoma to the Louisiana Forest Products Development Center (LFPDC) at Louisiana State University, where they were hammer-milled.

For the heterogeneous three-layer boards, large particles passing through the 16 mm screen were laid out as the core layer. Hand-screened fine particles smaller than 3 mm were used for the two outer face layers. A 30:70 flake weight ratio of face to core was used. The homogeneous single-layer boards were constructed using medium sized particles (which included bark) of about 6 mm.

Single layer red cedar particleboard (RCPB1) was constructed at the two ND levels 0.50 and 0.65 g/cm^3. Three-layer particleboard (RCPB3) was made at the four ND levels 0.40, 0.50, 0.65, and 0.75 g/cm^3. Both types of particleboard were bonded with 7% of urea formaldehyde (UF) resin and 1% wax. Two replicates at each ND were made for both the single and three layer boards.

Particles were dried to 3.5% MC, and then blended with commercial urea-formaldehyde and wax in a laboratory rotary drum-type blender. For the three-layer construction, separate blending was required for the outer face and core layers. The mats were randomly formed and compressed to 13x508x610 mm under 190^{o}C and 4.44 MPa in the hot press for 7 minutes. After hot pressing, the panels were conditioned and edge-trimmed.

5.2.3. Bagasse Particleboard

Year old bagasse residuals in the form of fiber-bundles of outer sheath and spongy pith were procured after sugarcane processing. The coarse bagasse was shredded and rotary-dried to 10-12% MC. In the tub grinder, impurities were removed before the bagasse was hammer-milled through a 6-mm screen. Prior to hot press, the particles were blended with diphenylmethane di-isocyanate (MDI).

Resination time was four minutes. The press cycle was 165 s under a loading rate of 0.8 s/mm for the 13 mm boards. The mats were steam-pressed for six minutes at 185˚C. After hot press, the boards were cooled, stacked and sanded as the finished product Duracane Agrifiber panel manufactured by Acadia Board Company (Donnell 2000). The product declared properties for each 13x1219x2438 mm panel were 1043 to 1361 kg hardness and 272 kg screw-pull.

The bagasse particleboards were bonded with MDI resin at two RC levels (5% and 8%) and at two ND 0.72 g/cm^3 and 0.88 g/cm^3 levels. For each of the four RC/ND combinations, three 13x1219x2438 mm panels were selected for analysis (a total of twelve panels). From each panel, four 13x305x305 mm boards were cut randomly at the plant by the manufacturer and shipped to LFPDC for evaluation (a total of 48 boards).

5.3. SPECIMEN PREPARATION AND CONDITIONING

Eight, eight, and twelve 13x51x51 mm specimens were randomly selected and cut from the middle portion of each of OSB, BAPB, and RCPB, respectively. Each specimen in the study was conditioned for three weeks at 24˚C and 70% relative humidity (RH). To study the moisture effect, the RCPB specimens were conditioned for three weeks at 50% RH and 24˚C prior to their three weeks conditioning at 70% RH and 24˚C. The details of specimens processed are summarized in **Table 5.1**.

Table 5.1. Basic parameters of test panels.

Panel Type	Usage	Layer	Particulate -type	Particulate -size (mm)	Resin (% - type)	ND Levels	Replicate (specimens)	Total Specimens
Oriented strandboard (aspen)								
OSB14	Structure	single	Slender	0.635x 13x76	4%-PF	0.56, 0.72, 0.96, 1.12	2 (8)	64
OSB16	Structure	single	Flake	0.635x 13x76	6%-PF	0.56, 0.72, 0.96, 1.12	2 (8)	69
Particleboard (western red cedar)								
RCPB1	termite-	single	Granule	6, Core	7%-UF	0.50, 0.65	2 (12)	50
RCPB3	Toxicity	three	Granule	3, Face	7%-UF	0.40, 0.50, 0.65, 0.75	2 (12)	95
Bagasse particleboard (sugarcane)								
BAPB5	Residue	single	fiber-	<1, bundle	5%-MDI	0.72, 0.88	3 (4x2)	48
BAPB8	Product	single	Bundle	<1, bundle	8%-MDI	0.72, 0.88	3 (4x2)	48

5.4. DENSITY AND MOISTURE CONTENT MEASUREMENTS

Average Density (AD), equilibrium moisture content (EMC), and density profile across thickness were measured for each specimen after each conditioning regimen. Density profile across thickness was obtained using a Quintek Density Profiler (QDP-01X) for each specimen.

5.5. ULTRASONIC TRANSMISSION MEASUREMENTS

The system setup for the direct-contact ultrasonic transmission (UT) was described in **Fig. 2.1a**. The ultrasonic variables velocity, impedance, attenuation, and root mean square (RMS) voltage were used and measured in this study (Refer to Equations 2.2, 2.3, 2.4, and 2.5, respectively). The UT measurements (velocity, attenuation, RMS voltage) were adjusted as their respective specific terms by dividing the values with the sample density. In this chapter, a preliminary variation

of the gain setting caused a profound effect on the UT measurements, as expected. Therefore, the hardware calibration settings of gain, damping, pulse height, pulser gain, and attenuator, were maintained at a constant level while the UT measurements were taken for specimens of all densities.

5.6. DESTRUCTIVE STRENGTH MEASUREMENTS

After AD, MC, and UT measurements were taken, the specimens were mounted on internal bond (IB) blocks and conditioned at 24^{o}C and 70% RH for about a week to achieve MC equilibration and glueline curing. The IB strength for each specimen was then evaluated at a constant strain rate of 1.0 mm/minute (0.04 in./min.) using an Instron 4260 universal machine according to the ASTM D1037 standard. Only specimens without glueline failures in the IB tests were included in the analyses. MC of each specimen was determined at the time of testing. The internal bonding was also adjusted as specific IB (*SIB* in kN.m/kg) for density differences among panel types.

5.7. RESULTS AND DISCUSSION

5.7.1. EMC for 70% RH Conditioning

Sample averages for all variables are tabulated in **Table 5.2** by ND and panel type. From the two-factor ANOVA model with F[3,52], the EMC means between ND's in BAPB5 are not significantly different (neither are those of AD, Attenuation, RMS voltage, IB, etc.), indicating that these specimens originated only from higher ND panels; therefore, the BAPB5 data was excluded from all analyses. From the two-factor ANOVA model with F[7,110], there is significant

ND*Panel type (i.e., RC levels) interaction for EMC ($p=0.015$), and the EMC main effects for the two OSB panel types are highly significant ($p=0.005$). For the RCPB panels (using the ANOVA model with F[5,139]), there is no restricted panel type*ND(levels 0.50 and 0.65 only) interaction for EMC ($p=0.756$), and the two restricted EMC panel type main effects are highly significantly different ($p<0.0001$).

In **Table 5.2**, the highest EMC average (7.5%) was attained by OSB, followed by RCPB (6.3%), and BAPB8 (4.3%). The particulate size differences between the three panel types suggest the relative amount of sorption sites available for water molecules in the S2 cell wall layer in each panel type. The large flakes of OSB16 contain the most sorption sites. The granular particles of RCPB's contain intermediate amounts of sites. The small fibrous particles of BAPB8 contain the least amount of sorption sites (with the assumption that the adhesive consumed most of the surface sorption sites). Also the BAPB8 panels with lower density had the largest water adsorption; the higher EMC (5.0%) in the ND 0.72 panels than the ND 0.88 panels (3.7%), which is consistent with Wu (2001).

Table 5.2. Average values of properties and ultrasonic measurements by panel type.

Panel type	n	ND levels	AD g/cm^3 (SD)	C/R*	EMC % 70% RH (SD)	IB MPa (SD)	SIB kN.m/kg (SD)	V km/s (SD)	SV m^4/(s.kg) (SD)	Z g/(s.m^2) (SD)	A -dB (SD)	SA dB.cm^3/g (SD)	RMS v (SD)	SR V.cm^3/g (SD)
Oriented strandboard (aspen)														
OSB14	17	0.56	0.574 (0.03)	1.5	p q 7.1 (0.3)	0.45 (0.11)	n 0.78 (0.19)	0.75 (0.09)	1.30 (0.12)	0.43 (0.07)	29.2 (6.45)	51.1 (12)	0.50 (0.15)	j 0.88 (0.26)
	18	0.72	0.802 (0.06)	2.1	p r 6.8 (0.5)	0.80 (0.19)	m o 0.99 (0.21)	0.90 (0.08)	e f 1.12 (0.10)	0.72 (0.10)	a c 4.38 (4.37)	g h 5.80 (6.2)	d 1.13 (0.15)	1.40 (0.14)
	16	0.96	0.991 (0.08)	2.6	qrs 7.3 (0.5)	0.93 (0.18)	k o 0.93 (0.14)	1.17 (0.20)	e 1.18 (0.14)	1.17 (0.28)	a b 2.26 (2.06)	g i 2.40 (2.4)	d 1.10 (0.11)	1.12 (0.18)
	7	1.12	1.226 (0.04)	3.2	s 7.8 (0.3)	1.07 (0.16)	kmn 0.87 (0.12)	1.28 (0.14)	f 1.05 (0.13)	1.57 (0.16)	b c 1.01 (0.66)	h i 0.82 (0.5)	0.96 (0.10)	j 0.78 (0.11)
	58	Avg.	D 0.898 (0.05)	2.2	7.3 (0.4)	0.81 (0.16)	0.89 (0.17)	E 1.02 (0.13)	1.16 (0.12)	F 0.97 (0.15)	G 9.20 (3.39)	H 15.0 (5.3)	0.92 (0.13)	1.04 (0.17)
OSB16	18	0.56	0.587 (0.04)	1.5	8.2 (1.8)	0.70 (0.19)	d e 1.19 (0.28)	0.79 (0.08)	1.35 (0.14)	0.47 (0.06)	28.8 (8.97)	49.8 (17)	0.29 (0.16)	0.49 (0.24)
	16	0.72	0.776 (0.07)	2.0	f i 7.6 (0.5)	x 1.19 (0.13)	1.54 (0.17)	0.96 (0.06)	Y 1.25 (0.13)	0.75 (0.09)	u 6.18 (6.99)	z 8.65 (11)	0.85 (0.24)	b 1.08 (0.25)
	17	0.96	0.977 (0.06)	2.6	f j 7.7 (0.5)	x 1.23 (0.25)	c d 1.26 (0.26)	1.17 (0.17)	Y 1.20 (0.13)	1.15 (0.23)	v 1.20 (1.46)	a 1.27 (1.6)	w 1.16 (0.16)	b 1.19 (0.14)
	9	1.12	1.253 (0.10)	3.3	i j 7.3 (0.6)	1.48 (0.16)	c e 1.19 (0.19)	1.32 (0.21)	1.05 (0.11)	1.67 (0.38)	u v 2.81 (5.41)	z a 2.19 (4.1)	w 1.12 (0.25)	0.90 (0.20)
	60	Avg.	D 0.898 (0.07)	2.2	7.7 (0.9)	1.15 (0.18)	1.30 (0.23)	E 1.06 (0.13)	1.21 (0.13)	F 1.01 (0.19)	G 9.75 (5.71)	H 15.5 (8.4)	0.86 (0.20)	0.92 (0.21)
Particleboard (western red cedar)														
RCPB1	25	0.50	0.585 (0.04)	1.8	t 6.3 (0.9)	0.59 (0.07)	1.00 (0.09)	s 1.03 (0.07)	1.77 (0.20)	0.60 (0.05)	7.17 (3.15)	12.7 (6.2)	0.53 (0.17)	0.89 (0.24)
	25	0.65	0.680 (0.03)	2.1	t 7.0 (0.7)	0.72 (0.06)	1.06 (0.08)	s 1.04 (0.05)	1.54 (0.07)	0.71 (0.06)	3.67 (1.73)	5.50 (2.9)	0.73 (0.13)	1.07 (0.18)
	50	Avg.	0.633 (0.04)	2.0	6.7 (0.8)	0.65 (0.07)	1.03 (0.08)	1.04 (0.06)	K 1.65 (0.13)	0.66 (0.05)	5.42 (2.44)	9.08 (4.6)	0.63 (0.15)	0.98 (0.21)
RCPB3	15	0.40	0.426 (0.05)	1.3	7.4 (0.7)	0.38 (0.13)	0.87 (0.19)	k 0.99 (0.07)	2.36 (0.28)	0.42 (0.07)	9.93 (2.98)	23.6 (7.3)	0.34 (0.16)	0.78 (0.32)
	25	0.50	0.521 (0.06)	1.6	5.1 (0.4)	0.56 (0.16)	1.06 (0.21)	k j 0.97 (0.07)	1.89 (0.30)	0.51 (0.06)	3.82 (2.88)	7.73 (6.2)	0.71 (0.22)	q 1.34 (0.35)
	25	0.65	0.687 (0.02)	2.1	R 5.9 (1.2)	0.97 (0.07)	1.41 (0.08)	j 0.95 (0.05)	O 1.38 (0.08)	0.65 (0.04)	m 0.81 (0.76)	p 1.20 (1.2)	n 1.12 (0.12)	q 1.63 (0.16)
	30	0.75	0.802 (0.04)	2.5	R 6.2 (1.2)	1.21 (0.16)	1.50 (0.17)	1.08 (0.08)	O 1.35 (0.07)	0.87 (0.10)	m 0.63 (0.37)	p 0.79 (0.5)	n 1.13 (0.13)	1.41 (0.17)
	50	Avg**	0.604 (0.04)	2.0	5.5 (0.8)	0.76 (0.11)	1.23 (0.15)	0.96 (0.06)	K 1.64 (0.19)	0.58 (0.05)	2.32 (1.82)	4.47 (3.7)	0.91 (0.17)	1.48 (0.26)
Bagasse particleboard (sugarcane)														
BAPB5	12	0.72	a 0.939 (0.02)	1.4	h 4.3 (0.4)	d 1.88 (0.49)	g 2.00 (0.53)	1.33 (0.13)	1.41 (0.15)	1.24 (0.12)	b 2.49 (1.30)	e 2.67 (1.4)	c 0.81 (0.10)	f 0.87 (0.09)
	20	0.88	a 0.933 (0.02)	1.4	h 4.3 (0.9)	d 1.82 (0.14)	g 1.95 (0.17)	1.18 (0.06)	1.26 (0.07)	1.10 (0.07)	b 2.47 (1.03)	e 2.66 (1.1)	c 0.81 (0.08)	f 0.86 (0.08)
	32	Avg.	0.936 (0.02)	1.4	C 4.3 (0.6)	A 1.85 (0.32)	1.98 (0.35)	1.25 (0.10)	B 1.34 (0.11)	1.17 (0.09)	2.48 (1.17)	2.66 (1.3)	0.81 (0.09)	0.87 (0.09)
BAPB8	16	0.72	0.802 (0.03)	1.2	5.0 (1.1)	1.54 (0.34)	1.91 (0.37)	1.09 (0.06)	i 1.36 (0.07)	0.87 (0.07)	4.66 (1.56)	5.87 (2.1)	0.66 (0.10)	j 0.82 (0.11)
	8	0.88	0.934 (0.08)	1.4	3.7 (0.7)	2.49 (0.53)	2.64 (0.37)	1.30 (0.10)	i 1.39 (0.05)	1.22 (0.19)	2.93 (1.28)	3.22 (1.5)	0.76 (0.13)	j 0.81 (0.10)
	24	Avg.	0.868 (0.05)	1.3	C 4.3 (0.9)	A 2.01 (0.44)	2.28 (0.37)	1.19 (0.08)	B 1.37 (0.06)	1.05 (0.13)	3.80 (1.42)	4.55 (1.8)	0.71 (0.11)	0.81 (0.10)

ANOVA pairwise comparisons (p.c.) of ND's within panel type and also main effects (m.e.) between panel groups** (F[1,110] for OSB, F[1,139] for RCPB, and F[1,52] for BAPB): a,b,c, … p.c.'s not significant with p≥0.17; A, B, C, … m.e.'s not significant with p≥0.11; **For RCPB, m.e. defined for ND's 0.50 and 0.65 only. n = number of specimens, * C/R = compact ratio (0.38 g/cm^3 aspen quaking, 0.32 g/cm^3 western red cedar, 0.65 g/cm^3 bagasse).

5.7.2. Internal Bonding Strength

From the two-factor ANOVA models, there is no significant ND*OSB panel type (i.e., RC levels) interaction for IB ($p=0.28$), while the restricted RCPB panel type*ND (levels 0.50 and 0.65 only) interaction is highly significant ($p<0.0001$). The OSB panel type main effects of IB (see **Table 5.2**) are highly significantly different, as are the restricted RCPB panel type IB main effects ($p\leq0.0001$). Within OSB panel type, the pairwise comparisons between ND levels are significant, the lone exception being ND 0.72 and 0.96 for OSB16 ($p=0.487$). When IB is corrected for density (SIB), the SIB ND means for OSB14 are not significantly different beyond ND 0.72 ($p\geq0.18$). For OSB16, the maximum SIB average occurs at ND 0.72.

From **Table 5.2**, the highest SIB averages for the BAPB8, RCPB, and OSB specimens are 2.28, 1.15, and 1.09 kN.m/kg, respectively. These averages are directly related to the relative surface areas of the particles in the three types of panels: the largest average SIB comes from the largest surface area, or vice versa. The fine fibrous bundles in BAPB form a synergistic bonding derived from lesser void spaces and better fibrous contact cohesion, resulting in the highest SIB average among specimen types. The superior bonding of RCPB relative to OSB is due to the larger surface area of the smaller granular RCPB particles than those of the more slender OSB flakes, resulting in maximum SIB average for RCPB exceeding that of OSB.

The compaction ratio (C/R, defined as the ratio of the nominal panel density to material density) is inversely related to the maximum SIB average values and is directly related to specimen type particulate size. The C/R ratios for BAPB8, RCPB, and OSB are 1.3, 2.0, and 2.2, respectively. The OSB had to have higher C/R to achieve a strength comparable to that RCPB.

Results of quadratic regressions of IB and SIB versus AD for the five panel types are summarized in **Table 5.3**. For all panel types, the least squares regression models for IB versus AD are highly significant ($R^2 \geq 0.67$); in fact, $R^2 \geq 0.86$ for RCPB3 and BAPB8. All quadratic regression IB curves increase with increasing density. For RCPB and BAPB specimens, the IB curves appear linear as compared to the quadratics of OSB shown in **Fig. 5.1**. For the "linear" curves, BAPB8 has the steepest slope, followed by RCPB3 and RCPB1, respectively. The OSB16 quadratic curve rises to its apex and levels off and is uniformly higher than the OSB14 quadratic curve.

The least squares SIB quadratic curves for both OSB14 and OSB16 increase and then decrease over the range of observed data, unlike their IB counterparts. Maximum SIB occurs for OSB14 and OSB16 at the approximate AD values 1.0 and 0.9 g/cm^3, respectively. The SIB quadratic curves for RCPB3 and BAPB8 exhibit the pattern of increasing then leveling off at the largest AD data values, 1.1 for BAPB8 and 0.85 g/cm^3 for RCPB3, while their IB counterparts appear linear and increase only. Both the IB and SIB least square quadratics for RCPB1 increase over the range of observed data.

Table 5.3. Regression models ($Y = A + B\rho + C\rho^2 + \varepsilon$) where Y is IB, SIB, Velocity, SV, Z, Attenuation, RMS, and ρ = AD (g/cm^3).

Variable	Panel types	A	B	C	R^2
IB	BAPB8	-6.37	12.21	-2.91	0.86
	RCPB1	0.03	0.67	0.50	0.70
	RCPB3	-0.69	2.58	-0.27	0.94
	OSB14	-0.73	2.60	-0.90	0.77
	OSB16	-1.14	4.23	-1.73	0.67
SIB	BAPB8	-8.81	20.03	-8.28	0.69
	RCPB1	0.80	0.31	0.10	0.09
	RCPB3	-1.07	5.91	-3.36	0.82
	OSB14	-0.11	2.28	-1.20	0.16
	OSB16	-2.45	9.87	-6.16	0.28
Velocity	BAPB8	-0.03	1.40	/	0.81
	RCPB1	0.97	0.10	/	0.01
	RCPB3	0.84	0.25	/	0.17
	OSB14	0.19	0.93	/	0.76
	OSB16	0.30	0.86	/	0.77
SV	BAPB8	1.34	0.03	/	0.00
	RCPB1	3.29	-2.59	/	0.72
	RCPB3	3.31	-2.58	/	0.81
	OSB14	1.43	-0.30	/	0.21
	OSB16	1.59	-0.42	/	0.38
Z	BAPB8	-11.04	24.50	/	0.95
	RCPB1	-0.46	10.89	/	0.79
	RCPB3	-1.12	11.68	/	0.91
	OSB14	-6.39	17.72	/	0.91
	OSB16	-6.42	18.18	/	0.94
Attenuation	BAPB8	52.1	-94.6	44.3	0.56
	RCPB1	86.3	-217.0	139.7	0.78
	RCPB3	36.3	-90.8	57.3	0.68
	OSB14	137.8	-263.6	124.8	0.86
	OSB16	139.9	-263.4	122.0	0.83
RMS	BAPB8	-1.96	5.09	-2.29	0.47
	RCPB1	-3.16	9.77	-5.91	0.68
	RCPB3	-2.11	7.95	-4.83	0.82
	OSB14	-2.71	8.05	-4.16	0.79
	OSB16	-2.72	7.04	-3.18	0.74

/ based on simple linear regression (C=0).

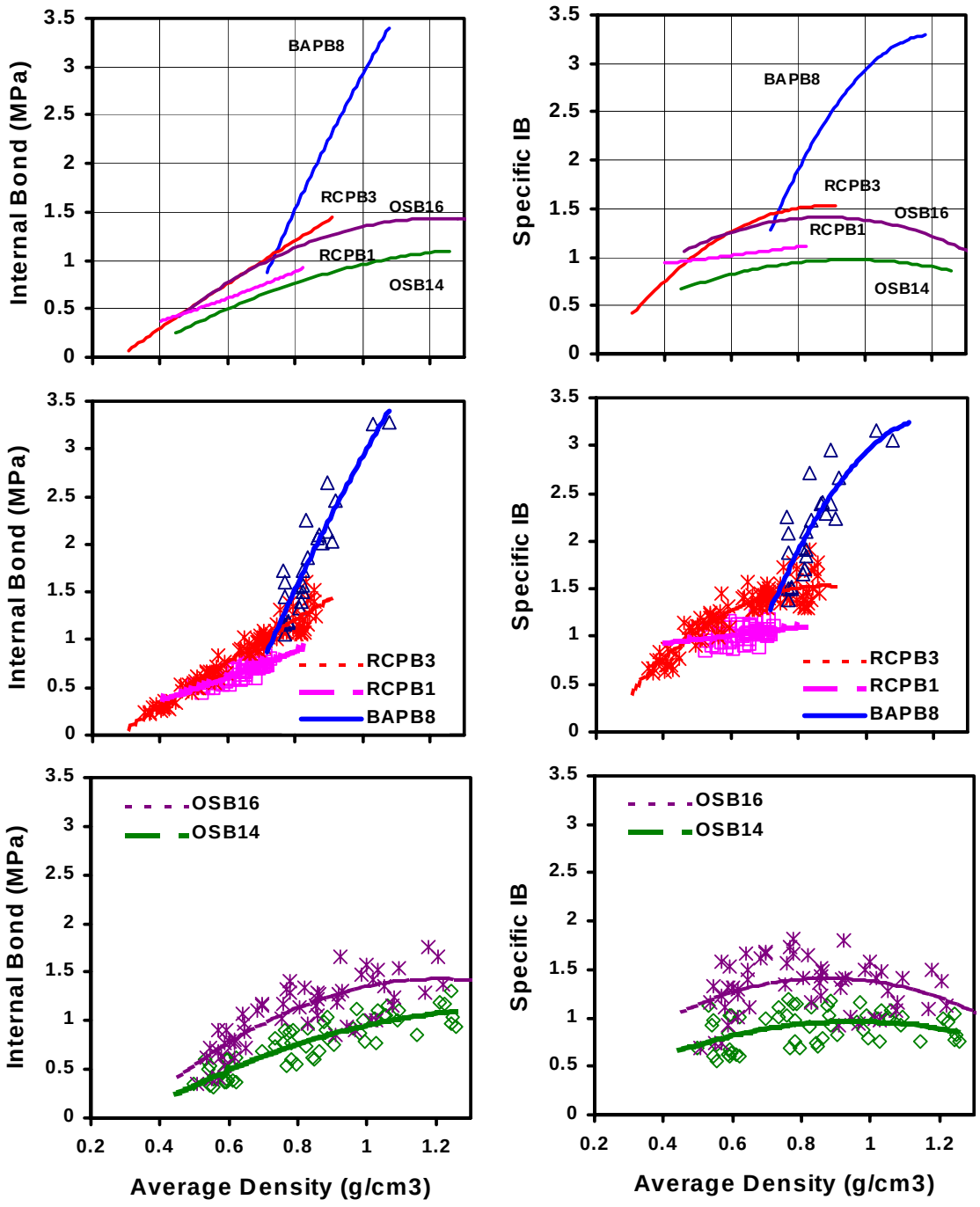

Fig. 5.1. Least squares quadratic curves of IB and SIB versus AD for the five panel types.

The intersection of the IB (SIB) curves for BAPB8, RCPB3 and OSB16 occurs at the approximate AD value of 0.75 g/cm^3, indicating that a common IB (SIB) strength of about 1.1 (1.4) kN.m/kg could be attained for these panel types. For AD values $\geq$ 0.75 g/cm^3, the SIB curves for the five panel types follow the ordering BAPB8, RCPB3, OSB16, RCPB1, OSB14. The last two panel types contain bark impurities, and have lower resin contents than the first three types. This may account for the ordering of the SIB curves.

5.7.3. Velocity and Impedance

For the UT variable velocity, the resin content mai effects for the OSB type (see **Table 5.2**) are not significantly different (p=0.129), while the resin main effects for specific velocity (SV) are (p=0.032). Conversely, for the RCPB specimens, the velocity restricted number of layer main effects (restricted to ND 0.50 and 0.65 only) are significantly different (p=0.002), whereas, those of SV are not (p=0.638). The BAPB attained the highest average velocity value (1.19 km/s). For the variable impedance (Z), the OSB resin content main effects are not significantly different (p=0.308).

In **Fig. 5.2**, the least squares straight lines for the three UT variables velocity, SV, and Z versus AD are depicted. For OSB specimens, both velocity lines have positive slope, while the slopes of the SV lines are negative. Both RCPB velocity lines are basically level, and are, therefore, unaffected by density; however, both RCPB SV lines have negative slope. The BAPB velocity line increases with increasing density, but the BAPB SV line is level (i.e., specific

velocity is unaffected by density). Since the SV line has zero slope only for BAPB specimens, and negative slope for the other two types, absolute velocity (defined to be SV) is impeded by the larger particles of the other two types, but not by the fine fibrous particles of BAPB.

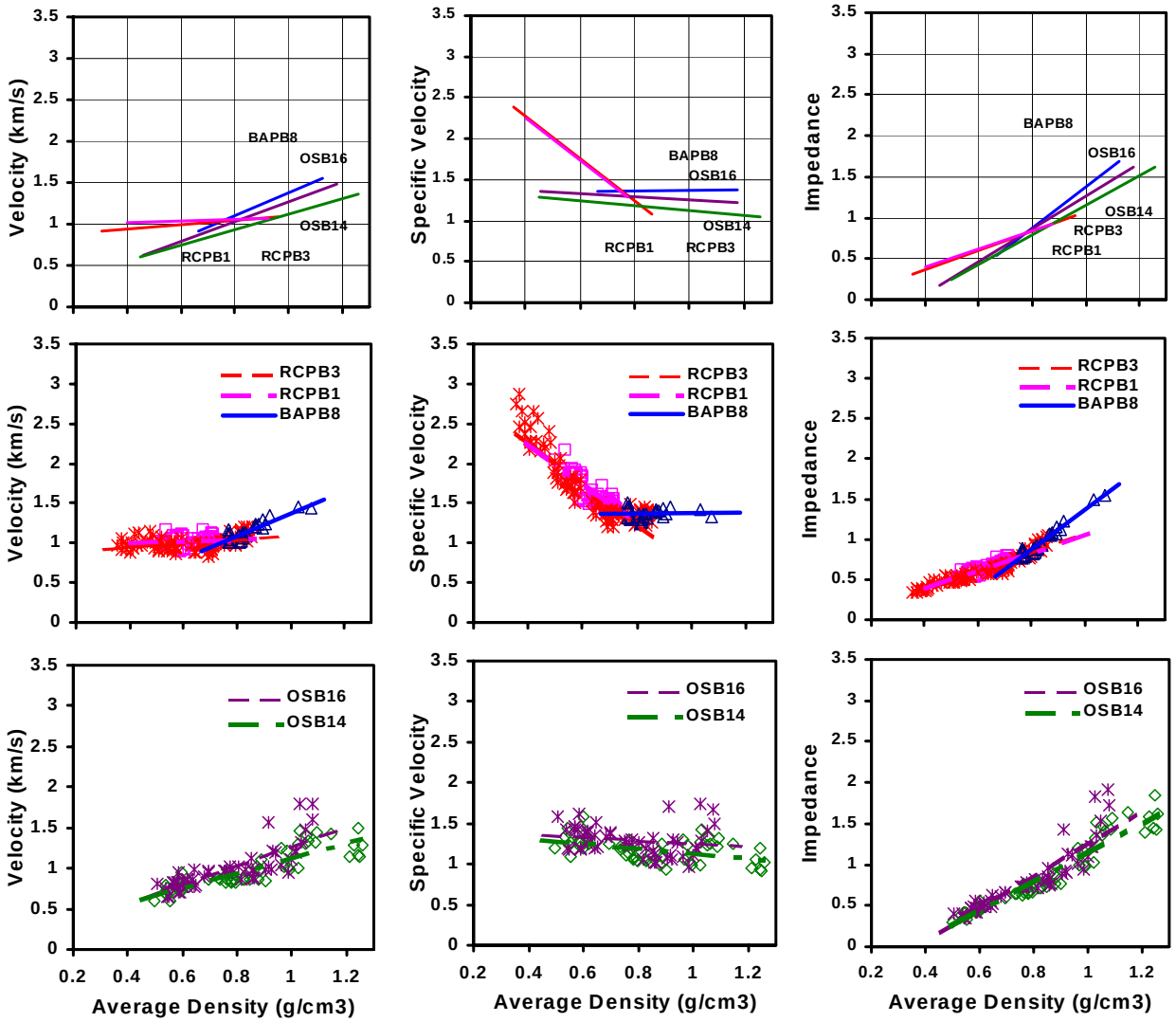

Fig. 5.2. Least squares straight lines of velocity, SV and impedance versus AD for five panel types.

The impedance lines for all panel types have positive slopes (**Fig. 5.2**). The magnitudes of the slopes follow the particle sizes of the panels. The line for the fine particle of BAPB8 had the greatest slope followed by lines for OSB16, OSB14, RCPB3, and RCPB1 in that order. The slopes for the velocity lines follow this same ordering. Thus, impedance is a measure of tortuosity of velocity flux through the material.

5.7.4. Attenuation and RMS

For all panel types, the least squares quadratic regression curves for attenuation against average density appear in **Fig. 5.3**. The attenuation curves for OSB14 and OSB16 are parallel (p=0.68). As previously mentioned, attenuation is a good measure of transmissivity of stress wave energy through the materials. Minimum attenuation for the RCPB and BAPB curves occurs at the approximate average density values 0.8 and 1.1 g/cm^3, respectively. The (negative) minimum value for the OSB least square curves occurs at the approximate average density value of 1.1. Negative values for the OSB curve (from approximately 0.9 to 1.2) correspond to attenuation values of zero.

Maximum RMS for the RCPB and BAPB curves occurred at the AD values for which the corresponding attenuation curves were minimized. The AD values at which the OSB14 and OSB16 curves were maximized (0.9 and 1.1, respectively) constitute the AD interval over which both OSB attenuation curves were negative.

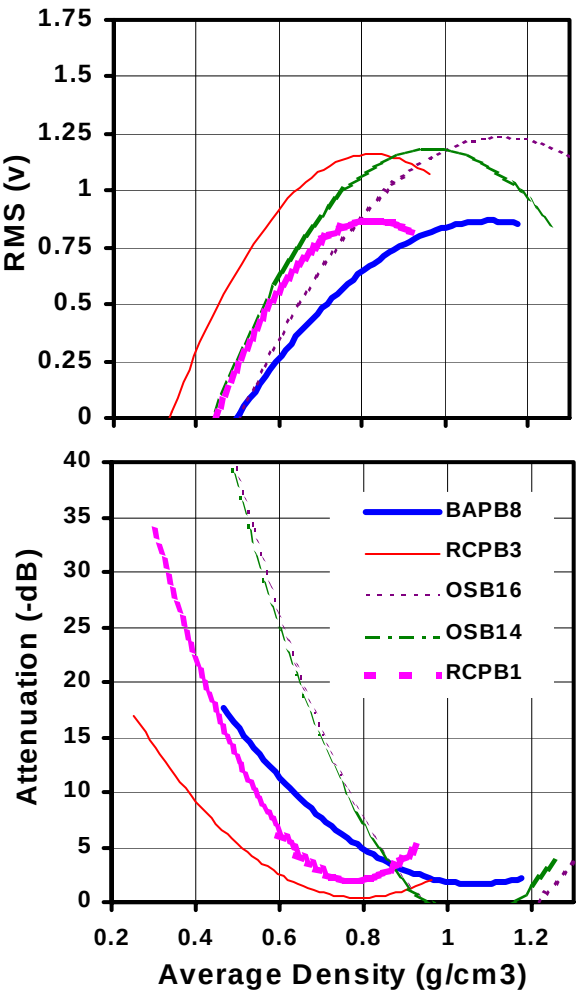

Fig. 5.3. Least squares quadratic curves of RMS voltage and attenuation versus average density for the five panel types.

The coincidence of these AD values may indicate the density for the greatest transmissivity of stress wave energy at these so-called "zero voids" densification levels for the respective panels. This densification phenomenon, also observed in Vun et al. (2003), is the transitional points of diminishing void structure, a function of particle size and density. Beyond these densities, absolute IB appeared to be diminishing with density. In general, the ultrasound dissipation

characteristics by absorption or scattering result from a careful balance of its density, porosity, fineness of fibers, bulk elasticity, and thickness (consistent with Smith 2001), contributing to the mechanical behaviors and properties for a particular product.

5.7.5. Effect of MC on UT Parameters

The moisture effect for the RCPB3 ND 0.65 (RCPB3-65), RCPB3 ND 0.75 (RCPB3-75), and RCPB1 ND 0.65 (RCPB1-65) specimens, EMC, IB, and the three primary UT measurements are studied and results are summarized in **Table 5.4** for the two 50% and 70% RH conditioning regimens. Using individual paired t tests, average EMC's for 50% and 70% RH conditioning were found to be significantly different for all RCPB specimens ($p \leq 0.021$). For RCPB1-65, attenuation and RMS voltage averages for the 50% and 70% RH conditions are significantly different ($p \leq 0.049$), while those for velocity are not ($p = 0.286$). This shows that both attenuation and RMS voltage are indicators of moisture change in the single layer RCPB ND 0.65 boards.

The 50% and 70% averages for the UT variables attenuation and RMS voltage are significantly different ($p \leq 0.050$) for the RCPB3-65 specimens, but the velocity averages are not significantly different ($p = 0.160$). Hence, velocity is not affected by the change in moisture content. For higher density RCPB3-75 specimens, EMC averages for the two RH conditions are significantly different ($p = 0.002$), while the UT variables are not ($p \geq 0.173$). The increase in density for the RCPB3-75 specimens results in acoustic bulking that increases the molecular

cohesion and reduces internal friction in particleboards, making velocity, attenuation and RMS voltage measurements invariant to the 50% and 70% RH conditioning regimens (consistent with the findings of Norimoto and Gril 1993). For all RCPB types, the internal bonding (IB) averages for the two conditionings are not significantly different ($p \geq 0.122$).

Table 5.4. Internal bond and UT variables values at 50% and 70% RH conditioning for the single-layer RCPB1-65, and three-layer RCPB3-65 and RCPB3-75.

	RCPB3-65		RCPB3-75		RCPB1-65	
	Total		Total		Total	
Specimens	Mean	p-value[a]	Mean	p-value[a]	Mean	p-value[a]
EMC5@50%RH (%)	5.16	0.021	5.13	0.002	6.14	0.000
EMC7@70%RH (%)	5.88		6.20		7.02	
Velocity5 (km/s)	0.97	0.160	1.12	0.173	1.07	0.286
Velocity7 (km/s)	0.95		1.08		1.04	
Atten5 (-dB)	0.45	0.041	0.74	0.358	2.87	0.047
Atten7 (-dB)	0.81		0.63		3.67	
RMS5 (v)	1.09	0.050	1.10	0.623	0.85	0.049
RMS7 (v)	1.12		1.13		0.73	
IB5 (MPa)	0.97	0.846	1.28	0.122	0.81	0.246
IB7 (MPa)	0.97		1.21		0.72	

a Two tailed p-values from paired t-tests: t(24) tests for both ND 0.50 and 0.65, and t(29) for ND 0.75. Gain set at (-8,40 dB).

5.8. CONCLUSIONS

The equilibrium moisture content of the panels indicates the relative amount of sorption sites available for water molecules: the large flake particles of OSB's (7.5%) have the most sorption sites, followed by the small granular particles of RCPB's (6.3%) and the fine fibrous particles of BAPB (4.3%). Panels with the lowest density had the largest water adsorption. Both attenuation and RMS voltage are indicators of moisture change in the single layer RCPB, while velocity is not.

Fibrous bundles in BAPB's form a synergistic IB strength derived from lesser void spaces and better fibrous contact cohesion. The better bonding achieved in RCPB over OSB is due to its larger surface area of small granular particles than the slender flakes in OSB. For each panel types, IB values increase with increasing compact ratio. IB strength of a particular panel is a balance of the material and processing makeup (material density, impurities, fineness of particle, porosity, MC, RC, resin type, etc). The IB curves for OSB level off, as opposed to those for RCPB3 and BAPB8, whose IB could still be improved by increasing the density level. IB for RCPB1 may also be improved by increasing AD, but not as much as RCPB3 and BAPB8 because of the adverse effect of the bark impurities.

The net effect of velocity propagation is impeded by the larger particle sizes of OSB and RCPB, but not by the fibrous constituents in BAPB. Therefore, velocity is a good indicator of physical impediments due to particle attributes in

these types of panels. The impedance versus AD least squares lines generally followed their velocity counterparts for the five panels.

Minimum attenuation and maximum RMS voltage occur at the density level of greatest stress wave transmissivity of energy for each of the five panel types. Such densities are the transitional points of diminishing void structure, a function of particle size and density. In general, an appropriate ultrasonic system calibration of these material factors is essential for optimization of desired properties and a technological bridge for these reconstituted composites.

5.9. REFERENCES

Bowyer, Jim L., and V.E. Stockmann. 2001. Agricultural residues: an exciting bio-based raw material for the global panels industry. Forest Products J. 51(1):10-21.

Chow, P. 1976. The use of crop residues for board-making. Environmental Conservation 3(1): 59-62.

DeHoop, C.F., S. Kleit, J. Chang, R. Gazo, and M. Buchart. 1997. Survey and mapping of wood residue users and producers in Louisiana. Forest Products J. 47(3):31-37.

Donnell, Ric. 2000. Acadia starts up bagasse board plant in Louisiana. Panel World 41(3): 34-41.

Food and Agricultural Organization of the United Nations, 1999. State of the World's Forest. FAO, Rome, Italy.

Gertjejansen, R. 1977. Properties of particleboard from sunflower stalks and aspen planer shavings. Technical Bulletin 311, Forestry Series No. 24. University of Minnesota, Agri. Expt. Sta., St. Paul, Minnesota.

Grace, J.K. 1996. Susceptibility of compressed bagasse fiber to termite attack. Forest Products J. 46(9): 76-78.

Hague, Jamie, A. McLauchlin, and R. Quinney. 1998a. Agri-materials for panel products: a technical assessment of their viability. *In* Proc. 32nd International Particleboard/Composite Materials Symposium. R. Tichy, D. Bender and M. Wolcott, eds. Washington State University, Pullman, WA.

Kelly, M. 1977. Critical review of the relationship between processing parameters and physical properties of particleboard. USDA Forest Products Lab. Gen. Tech. Rep. FPL 10:1-65. Madison, WI.

Kleit, S., C. deHoop, and J. Chang. 1994. An overview of Agricultural waste production in Louisiana. Pages 573-580 *in* Vol.2 Proc. 6th National Biomass Energy, Bioenergy Conference.

Kuo, M., D. Adams, D. Myers, D. Curry, H. Heemstra, J. Smith, and Y. Basin. 1998. Properties of wood/agricultural fiberboard bonded with soybean-based adhesives. Forest Products J. 48(2): 71-75.

LSU Agricultural Center. 2002. Progress Report: 5 years animal, fisheries, wildlife and plant commodities. Louisiana Cooperative Extension Service, Louisiana State University Agricultural Center, Baton Rouge, LA.

Norimoto, M., and J. Gril. 1993. Structure and properties of chemically treated woods. Pages 135-154 *in* Recent Research on Wood and Wood-based Materials. Shiraishi, N., H. Kajita, and M. Norimoto eds. Elsevier Science Publishers, Ltd., Essex, England.

Odozi, T., O. Akaranta, and P. Ejike. 1986. Particleboards from agricultural wastes. Agriculture Wastes 16(3): 237-240.

Russell, C. 1996. The straw resource: a new fiber basket? *In* Proc. International Particleboard/Composite Materials Symposium. M. Wolcott and L. Leonhardy, eds. Washington State University, Pullman, WA.

Smith, W.R. 2001. Wood: Acoustic properties. Pages 9578-9583 *in* Encyclopedia of Materials: Science and Technology. Elsevier Science Ltd, London.

Vun, R.Y., Q. Wu, M.C. Bhardwaj, and G. Stead. 2003. Ultrasonic Characterization of Structural Properties of Oriented Strandboard: A Comparison of Direct-Contact vs. Non-Contact Methods. Wood and Fiber Science 35(3)-- (*In-press*).

Wu, Q. 1999. In-plane dimensional stability of oriented strand panel: Effect of processing variables. Wood and Fiber Science 31(1): 28-40.

Wu, Q. 2001. Comparative properties of bagasse particleboard. Pages 277-284 *in* Mei C., Zhou X., Sun D., Zheng Y., Xu X. eds. Proc. Symposium on Utilization of Agricultural and Forestry Residues, October 31-November 3. Nanjing Forestry University, Nanjing, China.

Youngquist, J., B. English, R. Scharmer, P. Chow, and S. Shook. 1994. Literature review on use of non-wood plant fibers for building materials and panels. General Technical Report FPL-GTR-80. USDA Forest Service, Forest Products Lab., Madison, Wisconsin.

CHAPTER 6. MONITORING CREEP RUPTURE IN ORIENTED STRANDBOARD USING ACOUSTIC EMISSION

6.1. INTRODUCTION

The structural panel market is primarily for new housing and consumer applications. Low-cost oriented strandboard (OSB) is substituting plywood in sheathing, roofing, and flooring. The load-carrying capacity in service depends on the creep resistance of OSB. Creep, the rheological time-dependent deformation of the material under constant load, is exhibited through its viscoelastic responses to combined external factors (humidity, thermal, and load history) and intrinsic constitutive properties (species, resin, furnish quality, and processing effects).

The rheological behavior of creep in wood composites can be explained by linear viscoelastic theory, which treats the total deformation as a sum of three creep deformations: elastic (instantaneous and recoverable), delayed elastic or viscoelastic (time-dependent and recoverable), and viscous (permanent, plastic, and non-recoverable) deformations (Bodig and Jayne 1993). Most creep-rupture tests in high stress level exhibit the three creep stages. Primary-secondary stages suggest stress stabilization during early stages of loading, whereas tertiary creep signifies the approach to final failure.

Most creep studies in wood composites use 20-25% stress level resulting in a long duration-of-load modeling, while few creep-rupture studies at high stress level have been done. The creep rupture limit for a solid wood beam is relatively moderate in duration at 40% stress level (Sugiyama 1967). Under 70% stress level,

creep-rupture behavior in bending is affected by large cyclic changes of relative humidity (RH), due to sorption that affects the viscoelastic behavior of composites (Bryan and Schniewind 1965, Schniewind 1967, Haygreen et al. 1975). Fast cyclic changes in RH also cause hygroscopic fatigue. The onset of the tertiary creep manifested by an exponentially increasing rate is attributable to critical moisture content changes. Comparing the relative creep of chipboard, plywood, fiberboard and solid wood, waferboard is the least affected by either temperature or RH (Arima et al. 1986, Dinwoodie et al. 1991, 1992, Tang et al. 1997). However, the linear creep responses in plywood and chipboard are more adverse to temperature than humidity changes (Dinwoodie et al. 1985).

Much research on creep behavior of wood composites has been done using a wide range of experimental procedures and standards, where the long-term creep properties are compared to short-term static mechanical properties of small specimens. Small specimen tests, however, give 30% greater bending strength and 10% lesser stiffness than those large specimens tested in pure moment (McNatt et al. 1990). The pure moment test produces comparable values (Laufenberg 1987, CEN112 1997) to the 4-point bending test as adopted by the International Union of Testing & Research Laboratories for Materials & Structures (RILEM).

Integrity of the creep specimens depends on the analysis of actual fracture development, in which empirical methods dependent on deflection alone were not feasible. Nondestructive evaluation by monitoring acoustic emission (AE) in bio-based materials offers an alternative approach that is associated with the

development of internal flaw and crack propagation (Hamstad 1986, Beall 1996, Schniewind et al. 1996, Aicher et al. 2001, Dill-Langer et al. 2002, Vun and Beall 2002). When fibers or matrix elements in composites subject to stress exceeding its viscoelastic limit, fracture will occur releasing elastic energy in the form of AE events (Beattie 1983, Sato et al. 1984, Beall 1986b, Hsu 1994) that could be captured and studied for assessing fracture behavior in the material. Many AE studies (Drouillard and Beall 1990) in wood products are related to finger jointing strength of hardwood (Ayarkwa et al. 2001), resin content, density, and moisture conditioning effects on particleboard (Niemz 1981, Beall 1985, 1986a, 1986b), radial decay of wood (Beall and Wilcox 1987), flexural testing of OSB (Beall 1994), termite detection in wood (Noguchi et al. 1991, Lemaster et al. 1997), wood fiber in machining (Cyra and Tanaka 2000), and surface roughness and quality (Lemaster and Beall 1996, Rice and Phillips 2001). Much of the transducer advancements (Hamstad 1994) have made AE technology an effective real-time process monitoring device (Cavalloni and Kirchheim 1994). Creep studies were quite effective using AE technology (Beall 1996, Beall 1992). However, studies of creep-rupture in OSB subject to high stress are still lacking.

In this duration of load study, the RILEM protocol was used to provide comparable mechanical properties for large OSB panel performance subjected to high stress loading under different and changing humidity conditions. Specifically, an acoustic emission technology was used to provide a real-time system to evaluate and monitor the creep-rupture responses of commercial OSB under 80%

of ultimate strength exposed in low, increasing, and high moisture conditioning regimens.

6.2. METHODS AND PROCEDURE

6.2.1. Specimen Preparation

Twelve 15x1200x2400 mm commercial aspen OSB of 650 kg/m^3 bonded with 7% liquid phenol-formaldehyde resin were procured. From the middle portion of each board, eight 300x1000-mm specimens were obtained. In this study, the large specimens were side-matched and evaluated for the short-term strength and long-term creep-rupture tests.

6.2.2. Short-Term Strength Test

The short-term specimens were conditioned at ambient conditions for a month. Each specimen was tested in pure moment done in a third-point flexural fixture on a Baldwin machine (according to ASTM D3043), which determined its short-term strength properties. The specimen was supported in a 900-mm span and a 300-mm spacing between the loading heads, forming a constant moment area in the central third of the specimen. This configuration is the same as that RILEM creep test. Since the rate of 0.025 to 1 mm/s does not affect the short-term derivation of the ultimate strength in OSB (Beall 1994), a loading rate of 0.25 mm/s was applied until failure. The modulus of rupture (MOR) was calculated as

$$MOR = \frac{P(L - L_i)C}{4I} \qquad \textbf{(6.1)}$$

where, P is the ultimate load (N), L the span between pivot supports, L_i the spacing between loading heads, C the distance from the panel neutral axis to the extreme fiber (h/2), and I the panel moment of inertia ($bh^3/12$). The modulus of elasticity (MOE) was calculated as

$$MOE = \frac{(P'/\partial)(L - L_i)L_i^2}{32\,I} \qquad \textbf{(6.2)}$$

where, P'/∂ is the slope of the strain rate curve at instantaneous/initial elastic limit stressed at 80% ultimate strength.

6.2.3. Creep-Rupture Test

Creep-rupture test specimens were preconditioned at ambient conditions for a month before conditioning to the respective equilibrium moisture content (EMC) at the four test regimens: (1) Ambient: conditioned and tested at ambient room temperature and RH; (2) 12/12: conditioned for two weeks and then tested at 12% EMC (20°C, 65%RH); (3) 12/24: conditioned at 12% EMC for two weeks and then tested at 24% EMC (20°C, 95%RH); and (4) 24/24: conditioned for a month and then tested at 24% EMC.

A duration-of-load test frame (**Fig. 6.1a**) was constructed for the creep-rupture test (according to McNatt and Laufenberg 1991, Laufenberg 1986). A dead load equivalent to 80% of the mean ultimate stress was used for each specimen respective to its side matched short-term test counterpart. The load was applied at a rate of 0.50 mm/s, reaching a full load in about 10 seconds. Deflection at the center of the specimen referenced to the loading heads was

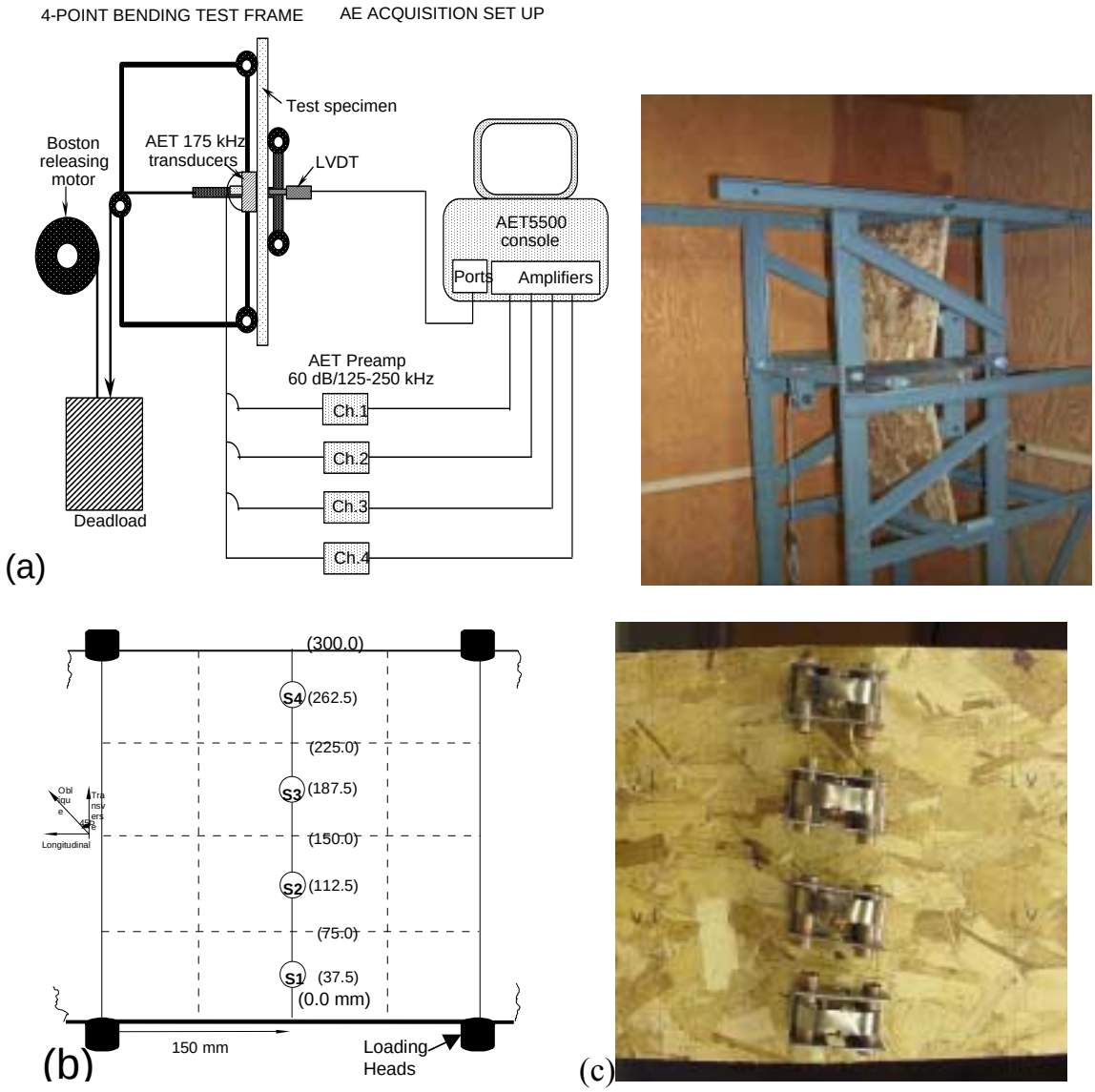

Fig. 6.1. Duration of Load frame and acoustic emission acquisition setup for the creep-rupture test (a) and sensor positions in the constant moment area of the specimen (b & c).

measured directly using a 0.8 v/mm LVDT that was connected to an analog port of the acoustic emission system (AET5500). The fracture pattern in the constant moment area (**Fig. 6.1b**) at the middle of the specimen was noted after failure. The

central moment area of the tested specimens was subdivided into 30x30-mm sections and carefully sawn for the spatial measurements of the average density.

6.2.4. Defect Test

In addition to the creep-rupture test, eight specimens were preconditioned for a month and then creep-rupture tested at the two conditioning regimens, i.e., ambient and 12% EMC (20°C, 65%RH). The influence of critical surface defects on creep was investigated by sawing an artificial notch on either the compression or tension side of the specimen, and tested in the duration-of-load frame. A saw with a 0.5-mm kerf was used to cut a notch to half the thickness of the specimen at 100-mm offset from the sensor axis.

6.2.5. AE Instrumentation Setup

During the duration of loading, the AET5500 multi-channel system acquired real-time acoustic emission (AE) data from four AET-175 kHz transducers positioned as in **Fig. 6.1b**. A 100 dB total gain was used to capture most signals of 14 to 77 dB amplitudes: 60 dB from the AET-160B preamplifiers (with 125-250 kHz filters) and 40 dB from the AET208-SPU console. A floating threshold of 1.0 volt was used to remove background noise. Calibration of AE transducers was done using lead breaks taken at a fixed point (see details in Beall 2002). A special transducer spring attachment was used to attach each sensor to the specimen. Using a double-sided adhesive tape, the sensors were bonded onto the smooth tension side of the specimen to minimize the effects of possible reduction of transducer coupling during flexure of the specimens.

6.2.6. Creep Parameters

6.2.6.1. Creep Factor

Creep defined as the time-dependent deformation exhibited by a material under constant load is commonly expressed as creep factor (CF) or relative creep. Some authors (Pu et al. 1992a, 1992b, Van Wyk et al. 1985) have defined creep factor (CF) as a ratio of the net creep deflection with time to the instantaneous elastic deflection. The net creep factor, CFn(t), is given as

$$CFn\ (t) = \frac{C(t) - C(0)}{C(0)} = \frac{C(t)}{C(0)} - 1 \qquad \textbf{(6.3)}$$

Appropriate for design applications, the CF used in this paper was computed as the total creep deformation with time normalized to the instantaneous elastic deformation (Laufenberg 1987, Halligan and Schniewind 1972, and Gressel 1972). The total creep factor, CF(t), is computed as

$$CF\ (t) = CFn\ (t) + 1 = \frac{C(t)}{C(0)} \qquad \textbf{(6.4)}$$

where, *C(t)* is the total deflection at time t, and *C(0)* the instantaneous elastic deflection immediately after loading. However, *C(0)* is dependent on the loading rate, specifically the elastic limit is taken as a function of the linear stress-strain slope. The elastic limit was reached in about 2.5 minutes. Some authors took the instantaneous elastic limit at a standard one-minute of loading. Creep factor is an important safety index to compare the relative creep behavior of panels with different MOE, and used appropriately to the applied stress level and environmental conditions. For example, in a wood-to-wood composite structural

system, a CF of 1.5 to 2.0 as a rule of thumb is a structural design safety factor (National Forest Products Association 1991). In a service condition of 24°C and a stress level of 16 to 20%, the CF for aspen OSB can range from 2.5 to 3.5, up to 5.0, for constant hot and humid conditions, and from 3.0 to 7.0 for cyclic hot and humid conditions (Pu et al. 1992a). In comparison, a CF of 1.5 for dried lumber is considered a non-conservative design factor for a duration-of-load greater than 2 to 3 weeks, and a factor of 2.0 for green lumber is sufficient for 2 months up to 50 years duration (Fridley 1992b). In defect-free laminated southern pine beam tests subjected to various loadings under a constant environmental condition, a CF of 1.48 for a stress level of 50% is recommended (Van Wyk 1985).

6.2.6.2. Creep Limit

The amount or level of stress, defined as the ratio of the applied load to the average ultimate bending strength of the control specimens, has a substantial effect on creep behavior in terms of total creep and permanent deflection. The effect of the various stress levels determines the duration-of-load factor in the creep limit. Creep limit is defined as the maximum stress in the viscoelastic range that produces a creep-rate approaching zero with time, or simply, the lowest limit of sustaining a maximum load that can be withstood by a material without creep failure. Numerous creep models were used to find the creep limit of a product, but its accuracy depends on the data reliability of a technique.

6.2.6.3. Creep Modulus

Creep modulus (CM), defined as the ratio of applied stress (in term of stiffness) to creep strain rate (Dinwoodie et al. 1985, Pu et al. 1992), is determined by

$$CM\ (t) = \frac{MOE_{\ i}}{1 + CF\ (t)} \qquad \textbf{(6.5)}$$

where MOE_i is the elastic modulus at instantaneous elastic limit and $CF(t)$ the creep factor at time t. Creep modulus, a combined effect of temperature and (medium to high cyclic) RH, is used as an index to predict long-term load-carrying capacity of a structural member.

6.3. RESULTS AND DISCUSSION

6.3.1. Equilibrium Moisture Content and Thickness Swelling

The specimens in the respective EMC conditioning regimens attained the following average moisture content (MC) on oven-dry basis: 7.2% MC (at 12% EMC); 23% MC (at 24% EMC); and 4.9% MC (at 6% EMC). Based on the 12% EMC specimens, the 24% EMC specimens attained 18.5% thickness swelling, while negligible thickness shrinkage was observed for both 6% EMC and ambient specimens. The MC between the ambient and 12/12 specimens is not significantly different ($p=0.11$). The high swelling in the 24% EMC is obviously a spring-back due to the high compaction ratio (1.7, the ratio of panel density to aspen density). Also at high MC, the high swelling rate is adversely affected the panel resistance to creep.

6.3.2. Deflection Versus AE parameters

An acoustic emission (AE) event contains many parameters, such as peak amplitude, event duration, ringdown count, rise time, energy (PA+10Log(Duration), or slope (PA(mv)/RT(us)), to permit assessment of the fracture behavior in the material (**Fig. 6.2**). Beall (2002) typically used the peak amplitude and event duration in his AE studies. However, **Table 6.1** gives the high correlation ($R^2 \geq 0.96$) between the deflection and the various logarithmic cumulative AE parameters for both the low/constant (12/12) and the high/constant (24/24) specimens. This indicates any logarithmic cumulative AE parameters can be an appropriate substitute for deflection. Particularly, the cumulative AE event count captured over the central moment area indicates an accumulation of incipient flaws up to final rupture. After fully loaded, spurious event peaks of fractures were still detected as seen in **Fig. 6.3c** (viz. cumulative event curves of either combined or individual sensor as in **Fig. 6.3b**), while these bursts of events were not readily indicated in the deflection.

The AE events captured are related to the fracture mechanism in the material. Under high stress beyond the yielding limit, wood or the resin elements undergo an atomic translocation of viscous (plastic) deformation by sustaining "microfractures". A microfracture at a locality can grow into a bigger fracture until the stress is subdued with an occurrence of a subcritical microfracture. With the remaining residual stress, further migration of the stress to other elements continues, or else an eventual critical rupture would occur.

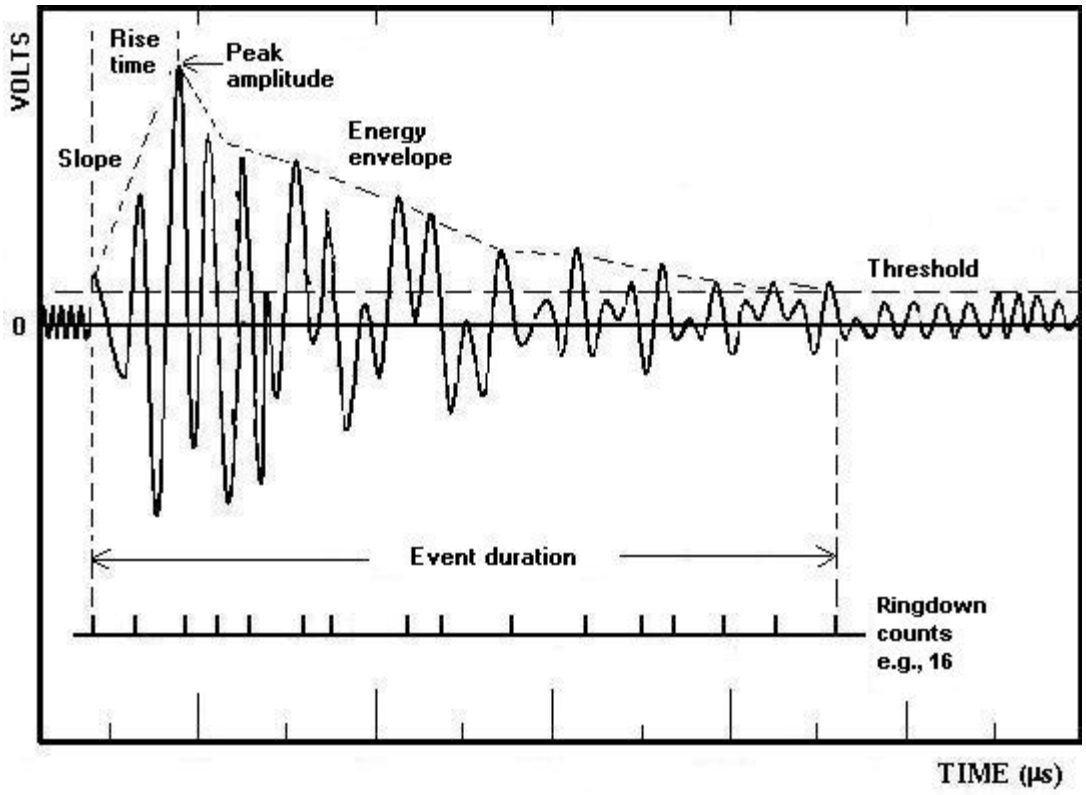

Fig. 6.2. A typical acoustic emission event showing wave parameters. The threshold level is set to obtain maximum AE sensitivity without introducing background noise. Event duration is the time between the first and final threshold crossing. Peak amplitude is measured from the baseline.

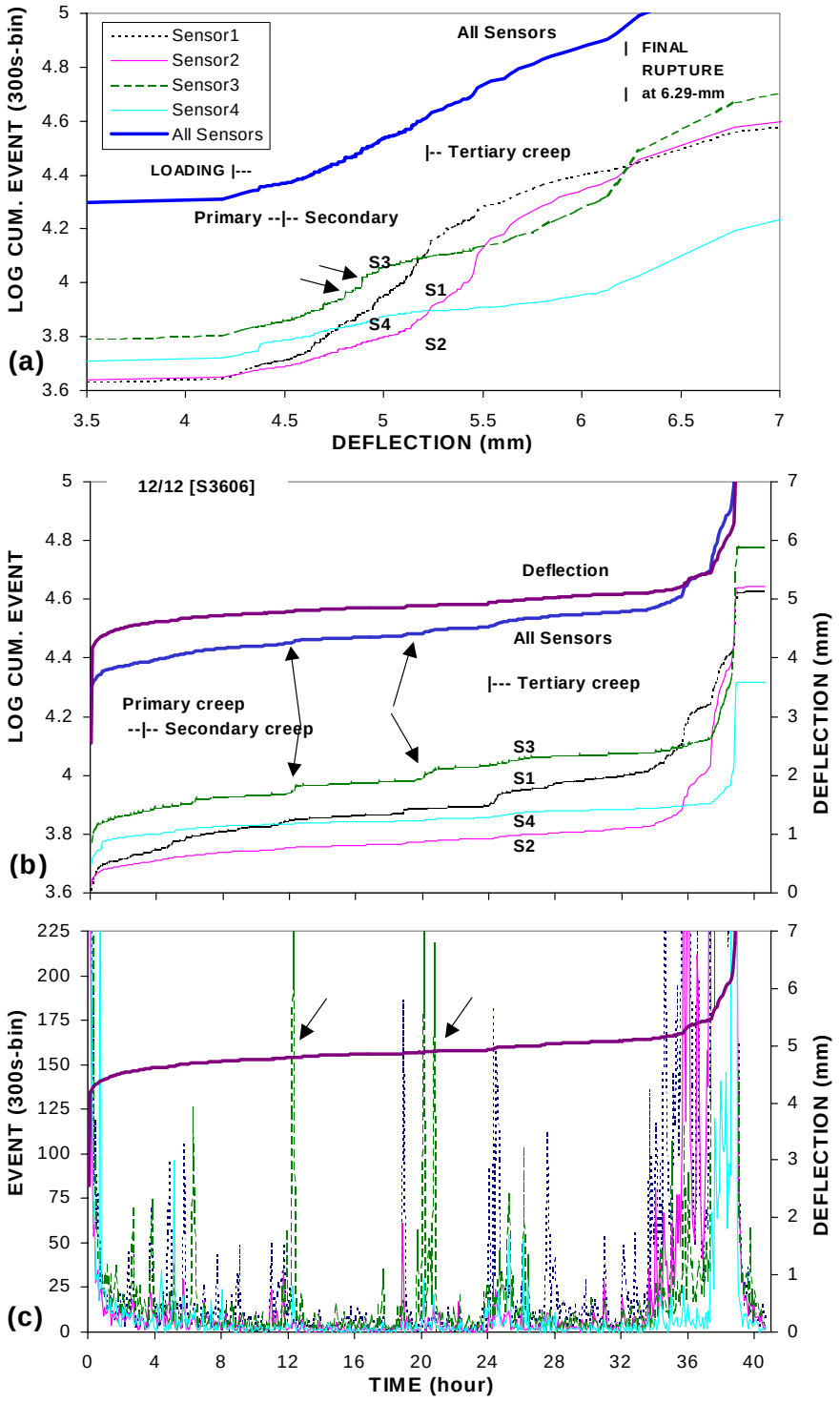

Fig. 6.3. AE event versus deflection in a 12/12 specimen [S3606] showing the individual sensor event to deflection correlations (a), the sensitivity of the cumulative event relative to deflection by sensor (b) that indicates the occurrences of sub-critical flaws at vicinity of sensor 3 in the secondary creep stage (c).

Table 6.1. R^2 values of the least squares regressions of the deflection as a function of logarithmic cumulative AE parameters for the low MC (12/12) and high MC (24/24) specimens.

Regimen: specimen	AE Parameters	Sensor 1	Sensor 2	Sensor 3	Sensor 4	All Sensors
12/12: C3606	Event	0.968	0.883	0.936	0.926	0.990
	Peak Amplitude	0.958	0.949	0.946	0.937	0.986
	Event Duration	0.971	0.935	0.954	0.962	0.990
	Ringdown Count	0.971	0.916	0.942	0.938	0.991
	Rise-Time	0.974	0.936	0.959	0.970	0.990
24/24: C4304	Event	0.976	0.917	0.877	0.950	0.974
	Peak Amplitude	0.976	0.902	0.871	0.801	0.967
	Event Duration	0.976	0.913	0.888	0.930	0.966
	Ringdown Count	0.978	0.912	0.894	0.923	0.966
	Rise-Time	0.966	0.915	0.887	0.941	0.965

For all regimens, the early flaw developments in the primary-secondary stages are manifested with relatively higher initial value of the logarithmic cumulative AE event curve than the deflection curve. The cumulative event curve then follows a relatively similar slope to the deflection (**Fig. 6.4**). Although moisture apparently dampened the detection of early events for the 24/24 specimens by 78% lower than those 12/12 specimens, the logarithmic cumulative event to deflection relationships for either low or high MC specimens are highly correlated ($R^2 \geq 0.97$). The cumulative AE event count, thus, is a suitable parameter for substituting deflection, because of its sensitivity and appropriate representation to incipient creep damages developed in the central moment area of the specimens.

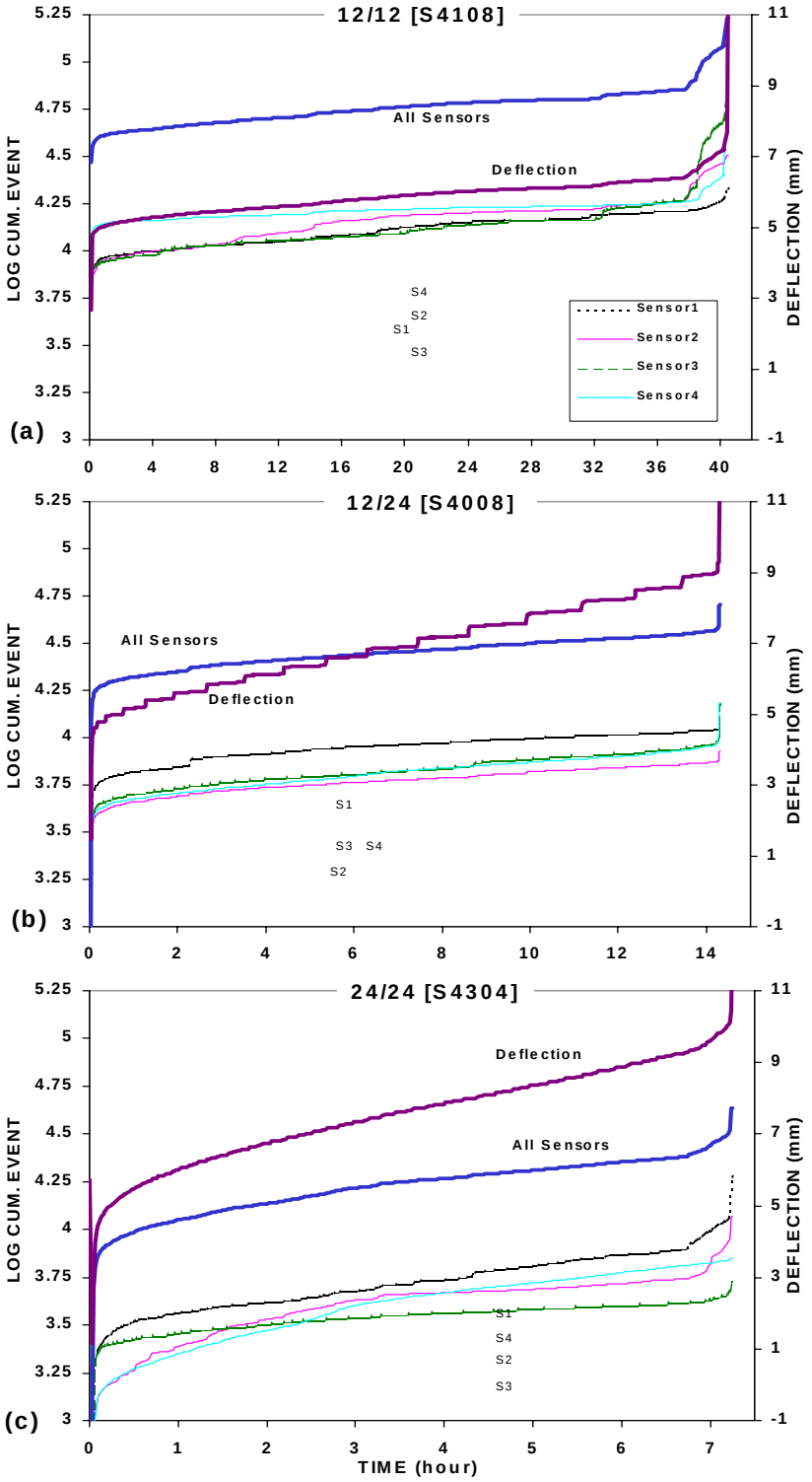

Fig. 6.4. Log cumulative event and deflection curves for the three test conditions for a 12/12 specimen (a); for a 12/24 specimen (b); for a 24/24 specimen (c).

6.3.3. Creep Stages

Primary creep spans the instantaneous viscoelastic limit of material deformation. The first bend or "knee" of the cumulative count curve is defining the nature of the elastic deformations transitioning to non-elastic deformations during loading. This knee is indicating the basic behavioral of the viscoelastic proceedings, which influences the probable creep rate or creep limit of the board. A relatively acute knee of the 12/12 specimens had a longer time to creep rupture than that of an obtuse knee. The primary-secondary stages suggest the importance of the proceeding for stress stabilization during the early stages of loading.

The stress stabilization in the secondary creep appears as diminishing damages reflected by the leveling rate of deflections and the appropriate representation of the respective cumulative event curves to temporal fracture events. Two subcritical flaw events occurred at sensor 3 (as bursts of AE, indicated by arrows in **Fig. 6.2b**) is propagated to another sub-critical flaw at sensor 1, which in turn triggered critical failures at sensor 2, the onset of an exponential failing rate to rupture. The combined-sensor cumulative event in **Fig. 6.2a** shows an erratic curve which is an indication of unstable stress stabilization leading to a tertiary rupture stage. However, some stiffer 12/12 specimens proceeded with stable secondary creep that prevailed without final rupture. On the other hand, the changing moisture content of 12/24 specimens caused many sub-critical flaws occurring in all positions (from the similar sensor trends seen in **Fig. 6.4b**) that eventually caused final rupture. The nature and distribution of the defect

elements (forming the points of stress concentration) would therefore determine whether the applied stress could be subdued, or further crack could be propagated leading to a tertiary rupture stage.

6.3.4. Creep-Rupture Regimens

6.3.4.1. 12/12 Specimen (constant/low MC)

Typical creep-rupture responses in the constantly low EMC (12/12) specimens were characterized by short time to elastic limit, high creep modulus (CM), high short-term MOR, and low creep rate leading to a long creep-rupture time (**Fig. 6.5a**). As expected, the 12/12 specimens reached their elastic limit faster due to a high CM (3.5 GPa) and MOR (24.3 MPa). From the first bend, a relatively acute knee curvature, the 12/12 specimens attained an elastic instantaneous deformation without ensuing viscous deformations.

The viscoelastic behavior for 12/12 specimens led to a longer time (+218%, based on time to elastic limit) to reach the nonlinear elastic limit, as compared with the obtuse knee of 24/24 specimens (+24% shorter time). Among all regimens, the stress stabilization in 12/12 specimens is due to the resilient elasticity (of lesser viscous deformation). Hence, the 12/12 specimens sustained brittle fractures beyond the 55% of the elastic deflection level that resulted in a constant creep rate (**Table 6.2**). This is evident in panels of high rigidity signified by the lowest creep rate (0.04 mm/h) and the longest time to rupture (51 h). As a rule of thumb, a critical reduction of 21% in stiffness and 56% in CF (1.56) would cause final rupture of the OSB exposed in dry conditions.

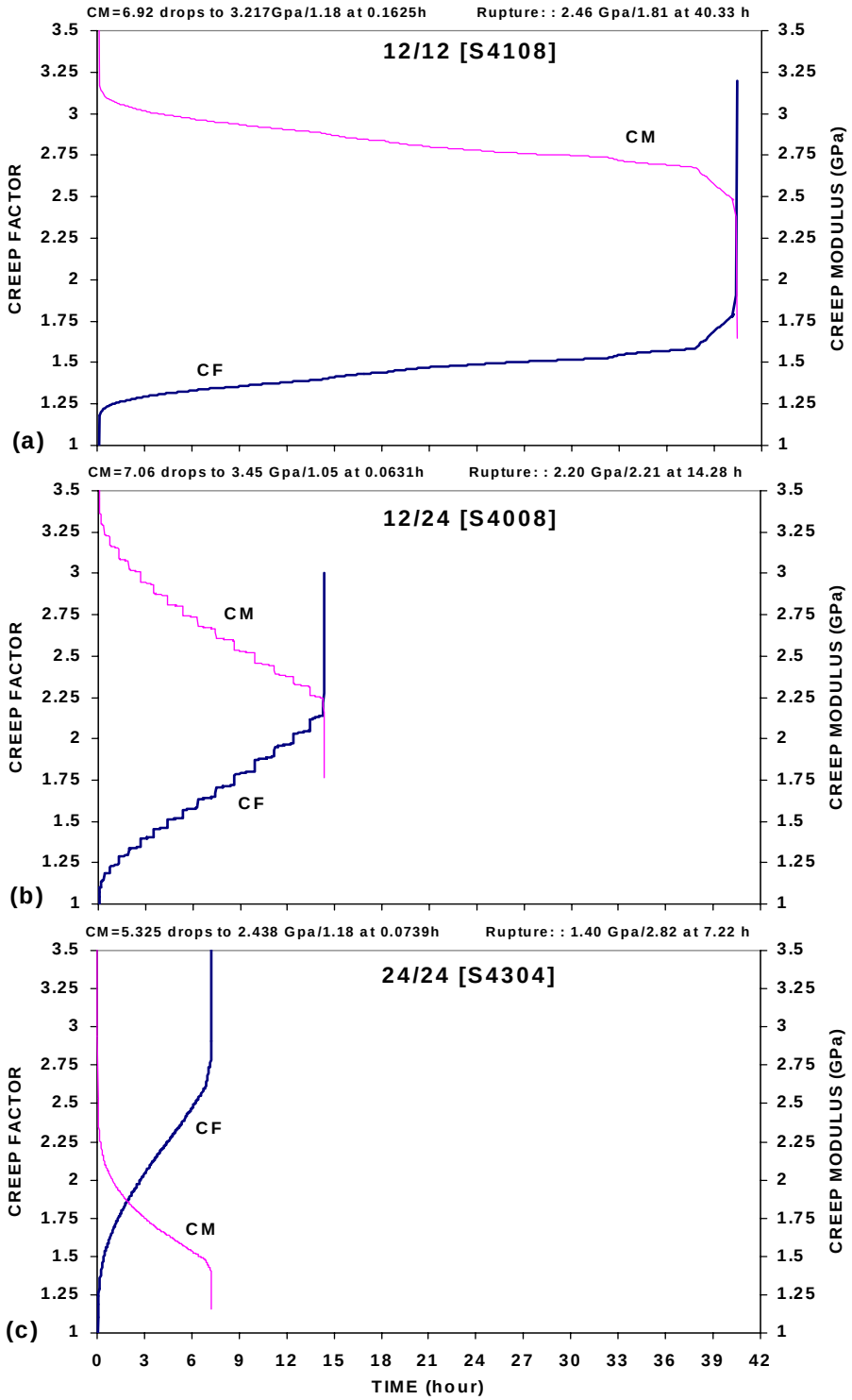

Fig. 6.5. Creep factor and creep modulus curves for the three test regimens for a typical 12/12 specimen (a); a 12/24 specimen (b); a 24/24 specimen (c).

Table 6.2. Results of the creep rupture by test regimen**.**

	REGIMEN						RECOVERY	
CREEP PARAMETER	12/12	*(±%)a*	12/18	*(±%)a*	18/18	*(±%)a*	(12/12)	
Side-matched pair								
MOE (GPa), short-term	6.98	*1%*	7.07	*-27%*	5.08	*13%*	7.86	
MOR (MPa), short-term	24.3	*-3%*	23.5	*-23%*	18.7	*-2%*	23.9	
MOE/MOR ratio	287	*5%*	301	*-5%*	272	*15%*	330	
Time-								
To elastic limit (s)	153	*6%*	162	*-3%*	148	*-1%*	151	
		218%		*40%*		*24%*		*150%*
To nonlinear elastic limit (s)	486	*-53%*	227	*-62%*	184	*-22%*	378	
		532%		*392%*		*-1%*		*2324%*
To rupture (h)	51.18	*-64%*	18.61	*-94%*	3.05	*198%*	152.7	c
	b*1907%*		b*589%*		b*24%*		b*5968%*	
Deflection (mm)								
At elastic limit	4.12	*0%*	4.14	*5%*	4.31	*-11%*	3.67	
		8%		*3%*		*14%*		*20%*
At non-linear elastic	4.43	*-3%*	4.28	*11%*	4.91	*0%*	4.41	
		44%		*119%*		*87%*		*6%*
At rupture	6.39	*47%*	9.38	*44%*	9.2	*-27%*	4.67	c
	b*55%*		b*127%*		b*113%*		to 0.42	
Creep rate (mm/h)								
At elastic limit	97		92		105		87	
At primary stage	3.35	*131%*	7.75	*1690%*	60.0	*250%*	11.74	
At secondary stage	0.04	*616%*	0.27	*3626%*	1.43	*-96%*	0.002	c
At tertiary stage	0.12	*304%*	0.50	*2316%*	3.02			
Creep Modulus (GPa)								
At elastic limit	3.49	*1%*	3.54	*-27%*	2.54	*13%*	3.94	
		-21%		*-38%*		*-35%*		*-9%*
At rupture	2.75	*-20%*	2.2	*-40%*	1.64	*30%*	3.57	c
Creep Factor							to 7.03	
At rupture	1.56	*46%*	2.28	*40%*	2.18	*-93%*	0.11	c

a percent change based on 12/12.
b percent change from elastic limit.
c recovery at unloading point.

Notably, the creep behavior for both ambient and 12/12 specimens is not significantly different. The cyclic RH fluctuation between 50% and 70% in the

ambient conditions has the same creep effects as for the constant 60% RH (also observed by Haygreen et al. 1975). Dinwoodie et al. (1984) also noted that creep response is greater for chipboard, waferboard, and plywood in a cycle of 65-95% RH than of 30-65% RH. A similar creep for flakeboard is seen in a fast cycle of 65-95% RH. The fast cyclic change in moisture causes fatigue, cumulatively weakens the adhesive bonds, and reduces the recoverable elastic creep due to hygroscopic movement of internal stresses. However, in a slow cycle of 95-65% RH, creep increases with desorption of moisture during low RH, while decreases with adsorption during high RH (Yeh 1990, Sugiyama 1967).

6.3.4.2. 24/24 Specimen (constant/high MC)

For the most extreme scenario, the constantly high EMC (24/24) specimens sustained a low elastic CM (2.54 GPa), a low short-term MOR (18.7 MPa), much higher strains for both elastic and non-linear elastic deflections, and shorter time to reach the non-linear elastic limit. With a relatively obtuse knee of the viscoelastic behavior, the high MC caused a 24% faster to reach the nonlinear elastic limit (see **Table 6.2**). Basically, the stress stabilization process is disrupted with more viscous deformations leading to an accelerated rupture time (3.05 h; 94% faster than the 12/12 rupture time). Coupled with the high swelling rate due to springback, the obtuse knee also signified the largest secondary creep rate (1.43 mm/h). **Fig. 6.5c** also shows that the high MC rapidly reduced the CM to the lowest (1.64 GPa, 40% below the 12/12), a phenomenon also observed by Pritchard et al. (2001). The remarkable increase in the creep deflection is

attributed to the large viscous component causing drastic reduction of the material strength. Since creep deformation is a time-dependent phenomenon, the viscous deformation would not vary linearly with time at high stress (Bodig and Jayne 1993) or high MC levels (Dinwoodie et al. 1985). Hence, a critical reduction of 44% (from the 12/12 elastic limit) in deflection (of 9.2 mm) and 118% in CF would cause catastrophic rupture when the panel is exposed to very humid conditions.

6.3.4.3. 12/24 Specimen (dynamic/rising MC)

The weakening effect of dynamic moisture changes (12% to 24% EMC's) has a practical implication as observed in the 12/24 specimens. **Fig. 6.5b** shows the rising moisture specimens undergoing accelerated deflection, which is stepwise. Clearly seen in **Fig. 6.6**, the occurrence of acoustic emission bursts preceded the deflection slippages, which indicates the significance of accumulation of flaw that led to the final slippages. Although the 12/24 creep rate to rupture (0.27 mm/h) is 81% smaller than the 24/24 (1.43 mm/h), it is 85% larger than 12/12 (0.04 mm/h). During loading, the 12/24 specimens produced a stepwise obtuse knee - an accelerated stepwise viscoelastic path - to reach the nonlinear elastic deflection. These typically large initial non-elastic deflections were the results of dynamic moisture adsorption seen as small-accelerated deflections following the subsequent adsorptions. This impact reduced the creep modulus (CM) by a substantial 38%. In fact, the CM is well correlated to the non-linear instantaneous elastic deflection (R^2=0.87).

The swelling in the boards from dynamic moisture adsorption initiated critical fractures, increased the wood flake separation, reduced adhesion and internal bonding strength. These data indicated a substantial flaw occurrence as a result of moisture adsorption (Bryan and Schniewind 1965, Dinwoodie et al. 1985) rather than fatigue at low humidity. However, surface failures may also be caused by desorptions (Bariska 1985, McNatt 1991). Therefore, the steeper slope of the various CF's in **Fig. 6.5** illustrated the deteriorating impact of dynamic rising of MC in OSB with a drop of CM from 3.5 to 2.2 GPa resulting in the highest CF value of 2.28 (**Table 6.2**).

For all regimens, the high correlation of the instantaneous elastic deflection to the stiffness of the panels (R^2=0.93) for all regimens indicates that stiffer panels have indeed a greater load-carrying capacity and also signified by the smaller instantaneous elastic and deflections, leading to a longer rupture time. In addition, the MOE/MOR ratio (the rank order of deflection) is a good indicator for nonlinear instantaneous deflection. For example, the higher the MOE/MOR ratio the lower will be the nonlinear elastic instantaneous deflection (consistent with findings by Pierce et al. 1979).

6.3.5. Creep Recovery

Most rheological creep components usually increase with increasing RH and temperature. To illustrate the viscoelasticity behavior of OSB during creep rupture, creep recovery tests were carried out for those ambient or 12/12 specimens that did not fail (a typical result of sample S4102 as given in **Table 6.2)**

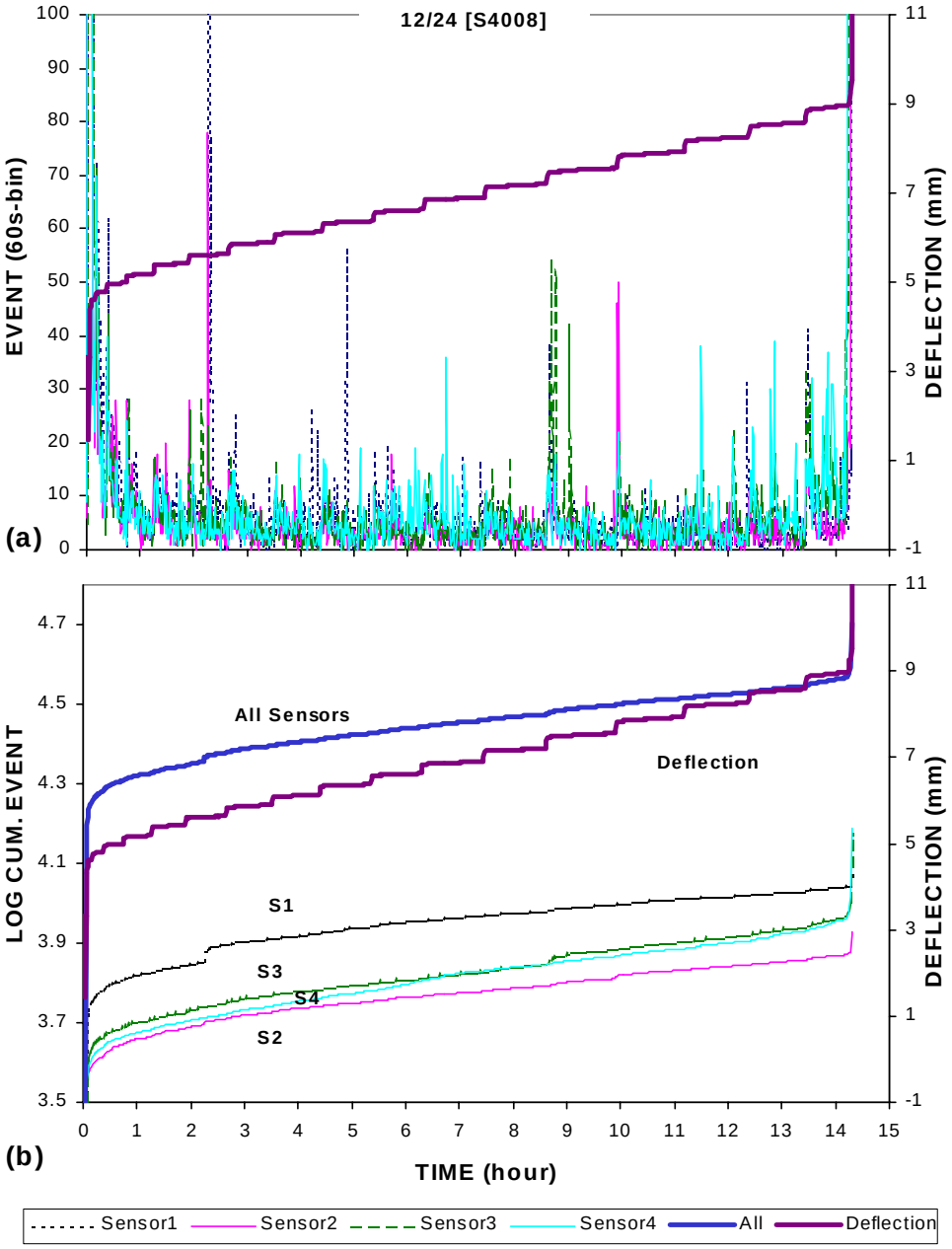

Fig. 6.6. Incremental event and deflection rates of a 12/24 specimen resulting in a step-wise slipping of deflection [S4008]. The event surges preceded the slips indicating the intensity of developing fracture due to moisture-stress interactions (a); the corresponding cumulative events by sensor versus the deflection curves (b).

After fully loaded, a low instantaneous elastic deformation of 3.67 mm (CF of 1.00 and CM of 3.94 GPa) was attained, indicating the response of the relatively high stiffness of the boards to the applied stress. The load was held for one week before it was instantaneously removed. In Fig. 6.7a, the typical creep recovery curves show that the AE bursts in sensor 3 of the secondary creep subdued the stress by sustaining local sub-critical failures/delamination, followed by massive events of friction or debonding. After fully unloading, the sensors captured the events pertaining to the shape recovery due to elastic and viscoelastic components.

Interesting behaviors are observed: a shorter time (22% lesser than 12/12) and the largest deflection change (20% of elastic limit) from the elastic limit to nonlinear-elastic limit (**Table 6.2**). The creep progressed at a negligible rate of 0.006 mm/h until unloading. **Fig. 6.7a** shows the elastic deflection of 3.666 mm was the lowest. When unloading was carried out at 4.664 mm (153 h), the deflection bounced instantaneously to 0.690 mm (after 0.2 h) recovering the elastic deformation. A final 0.437 mm deflection was reached (after another 13.5 h) recovering the viscoelastic deformation. The total creep recovered was 4.227 mm; of which 3.974 mm (85.2%) is due to the recoverable instantaneous elastic, 0.253 mm (5.4%) to the recoverable viscoelastic, and 0.437 mm (9.4%) to the permanent-viscous deformations. Although the pure viscoelastic component of the total creep was expected to increase with time (Moliński et al. 2000, Leicester 1971, Moren 1993), it was not significantly different. The viscous and viscoelastic portions, when combined, are smaller than the elastic portion. Subsequently, the

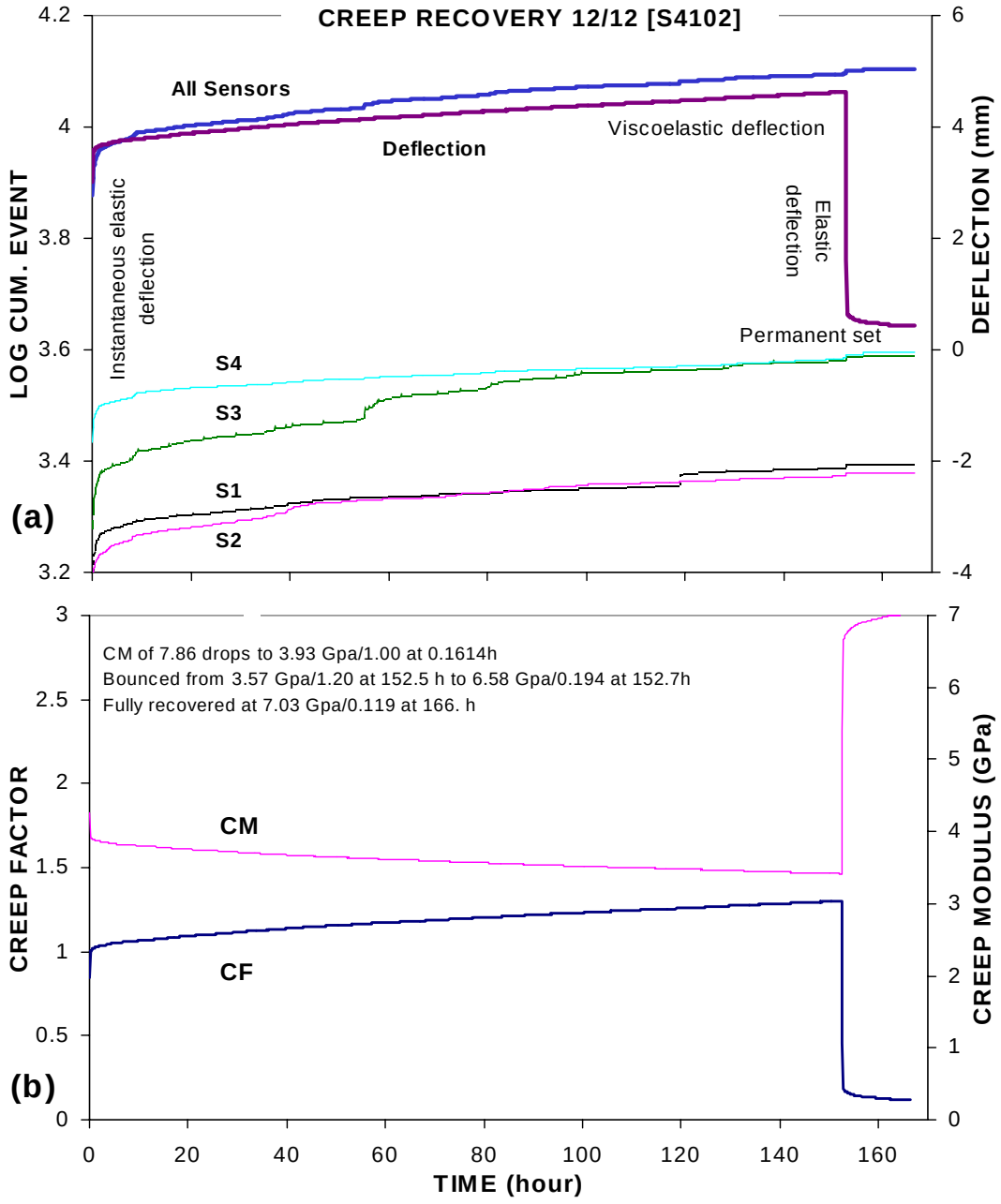

Fig. 6.7. Creep deflection and recovery test in a 12/12 specimen [S4102] showing the whole duration by cumulative sensor event and deflection curves (a), and the creep factor (CF) and creep modulus (CM) rates (b).

creep caused by high moisture condition does not fully recover when the specimen is redried to lower moisture content. Significant variation in the viscoelastic behavior, thus, depends on the viscous component of creep.

After fully loaded as in **Fig. 6.7b**, the short-term stiffness instantaneously dropped from 7.89 to 3.94 GPa of the elastic limit and stabilized at 3.57 GPa. With unloading, the stiffness bounced instantaneously to 6.58 GPa and stabilized at 7.03 GPa. The total MOE recovered was 4.32 GPa; of which 3.01 GPa (69.7%) is due to the recoverable elastic, 0.45 GPa (10.4%) to the recoverable viscoelastic, and 0.86 GPa (19.9%) to the permanent irreversible MOE's.

At high stress levels, the effect of the viscoelastic deflection (5.4%) represents twice of the viscoelastic stiffness (10.4%), as is in the case of the permanent deflection. Because of the resilient elastic toughness energy (Stanzl-Tschegg et al. 1996) in the creep recovery, elastic deflection component (85.2%) is compensated by having 15% lesser of the recoverable elastic stiffness (69.7%). This relationship is valid for OSB exposed at ambient or 12/12 conditions.

Considering the inverse relationships of CF and CM, the secondary creep slopes are especially useful in determining the creep limits. Specimen C3806 showed a typical creep recovery. It took 24 days (t=570 h) to rupture, which serves as the creep limit for the following models:

$$CF(t)=1.0661e^{0.0014(t)},\ R^2=.97 \qquad \textbf{(6.6)}$$

$$CM(t)=3.8068e^{-0.0008(t)},\ R^2=.97 \qquad \textbf{(6.7)}$$

$$C(t)=3.7911e^{0.0014(t)},\ R^2=.97 \qquad \textbf{(6.8)}$$

$$\text{Log Cum. Flaw Event}(t) = 3.9874e^{0.0002(t)},\ R^2=0.93 \qquad \textbf{(6.9)}$$

Under 80% stress level, most tests ruptured at about 1/3 of the creep limit. Since the large specimens were only one-eighth of the commercial size, actual density variations within specimens do exist, as they do between the commercial panels. Ability to control in-plane density variation within a certain tolerance would holistically address this concern, on which most mechanical properties depend.

6.3.6. Effects of Critical Defects Position

The MC between the ambient and 12/12 specimens is not significantly different (p=0.11). Negligible thickness shrinkage was observed for both 12/12 and ambient specimens. Hence, the natural RH fluctuation between 50% and 70% in the ambient conditions has similar creep effects as for the 12/12 specimens. Under 80% stress level, artificially notch was induced on either tension or compression sides on each of the 12/12 specimens. Although the artificial notch at the tension side of the specimen induced an early occurrence of tertiary creep (**Fig. 6.8a**), flaw development remained dormant in the secondary creep stage. Sometimes a long interplay of this mechanism leads to a longer period of creep. The long dormant period apparently shows stronger fiber-fiber or fiber-adhesive bonding, a resistance against the initiation and growth of critical cracks. Choi and Takahashi (1994) also observed a similar silent phenomenon at 88% stress level before a final rupture of a short fiber-reinforced composite occurred. Stress

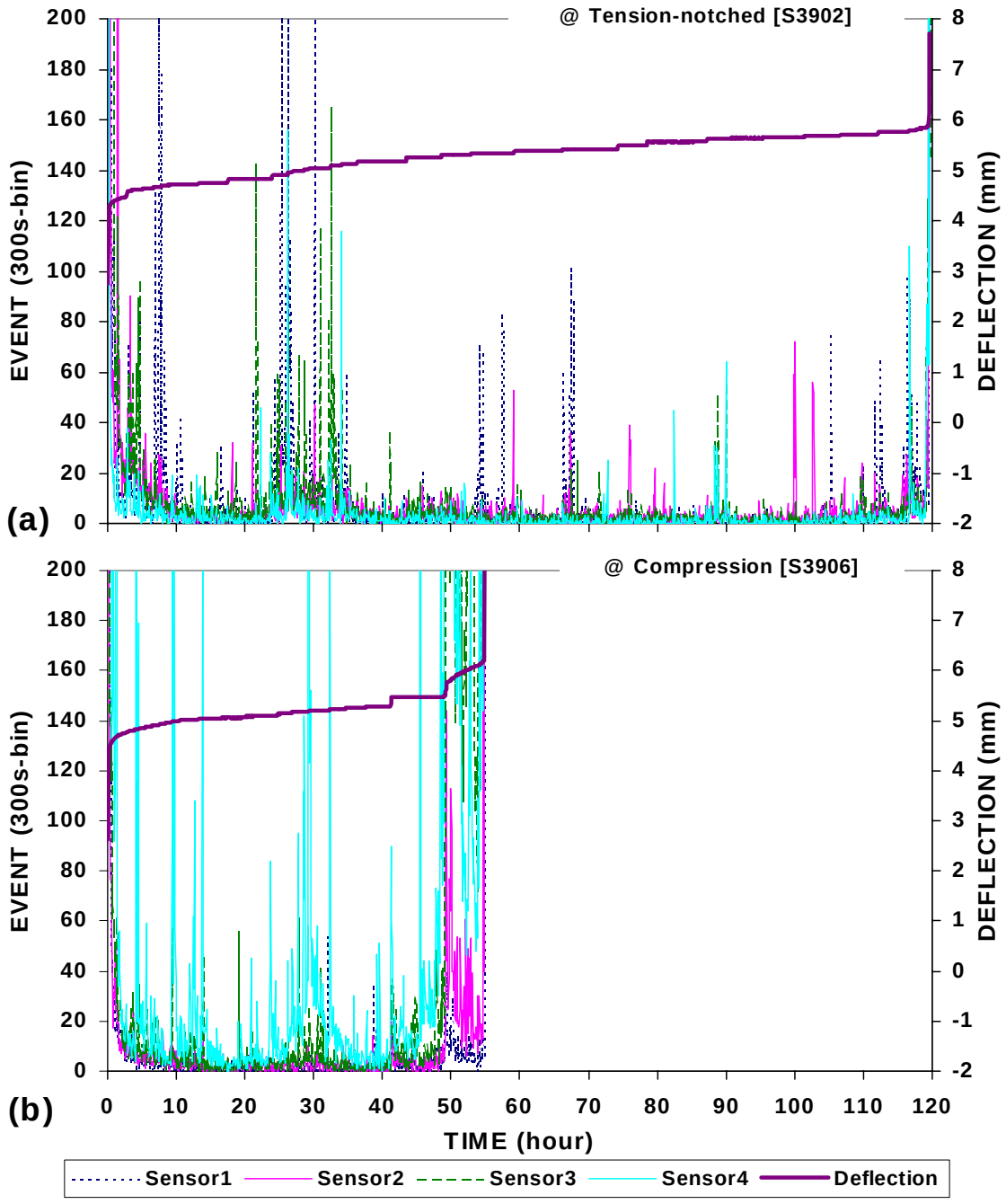

Fig. 6.8. Event and deflection rates for artificial notched specimens at 12/12 regimen. The sawed-notch on the tension-side [S3902] caused an early tertiary creep at the 30th hour, but did not warrant an early rupture (a); while on the compression-side [S3906] resulted in a chain of failure events in the early stage that accelerated catastrophic failure (b).

relaxation responses to crack formation and propagation may explain the silence AE of the dormancy of the tension-notched, which depend on the remaining level of the applied stress and the neighborhood material strength. Often, stress is being partially distributed to other supporting materials, or else the sustaining material would incur plastic straining, and a microfracture would ensue. Hence, the long dormant period of creep in the tension-notch did not critically warrant an early rupture, confirmed by the four side-match tests.

However, specimens with a notch on the compression side (**Fig. 6.8b**) failed in half the rupture time of those tension-notched specimens. As in all cases, the fracture did not seem to propagate through the notch made, but stress migrated to lower-density portions where critical fractures occurred. When fully loaded, the bending stress is at a maximum in the surface of the compression side, exerting the greatest load on the extreme wood fiber. Since wood fiber is weak in compression (about 10% of the bending strength), the extreme fiber is expected to creep into incipient plastic strain and eventually crushed, reducing the effective cross-section modulus of the panel. Then, the redistribution of the stresses and creep in time gradually shifts the neutral axis towards the tension-side, inducing greater stress and further rupture on the compression-side of the extreme fibers.

The negligible or lesser tensile creep under high stress level shows that total deflection depends on the extreme fiber creep at the compression-side of a bending board. The surface quality at the compression side is therefore critical and adversely affected the creep much more than the tension-side. In service

environments of dynamic changes of RH, worsened with wide RH fluctuation rates, moisture protection of the surface (particularly on the compression-side) of OSB is specially necessary to reduce flexural creep (consistent with Bach et al. 1993 finding). Similarly, Chen and Lin (1997) found that surface-laminated boards have a reduced creep deflection as compared with sanded specimens. These findings suggest that surface protection by temporary coatings or laminates safeguards the surface quality of a wood composite panel to resist creep in duration-of-loading. Notably, the creep fractures in OSB are not in total separation, but remain intact suspending the load, which could serve as a warning of impending structural catastrophe.

6.3.7. Density Variation as Defect Trench

Typical surface fracture patterns (along the loading head, oblique, and intermediary transverse) were superimposed against the measured average density distribution in the central moment area (**Fig. 6.9abc**). The fracture seemed to propagate and follow the valleys of low-density zones. This phenomenon can be related to the applied stress distribution in the in-plane direction. Stress causes deformations by crack formation and propagation, given a greater sustaining applied stress over the supporting material strength. Often, the stress is subdued by stronger supporting materials, or else the weak material would incur plastic straining and eventually a microfracture may ensue (Stanzl-Tschegg et al. 1996). As an effect of in-plane stress distribution, the critical cracks were initiated at the weakest wood elements, happened to be the lowest density zones in the boards.

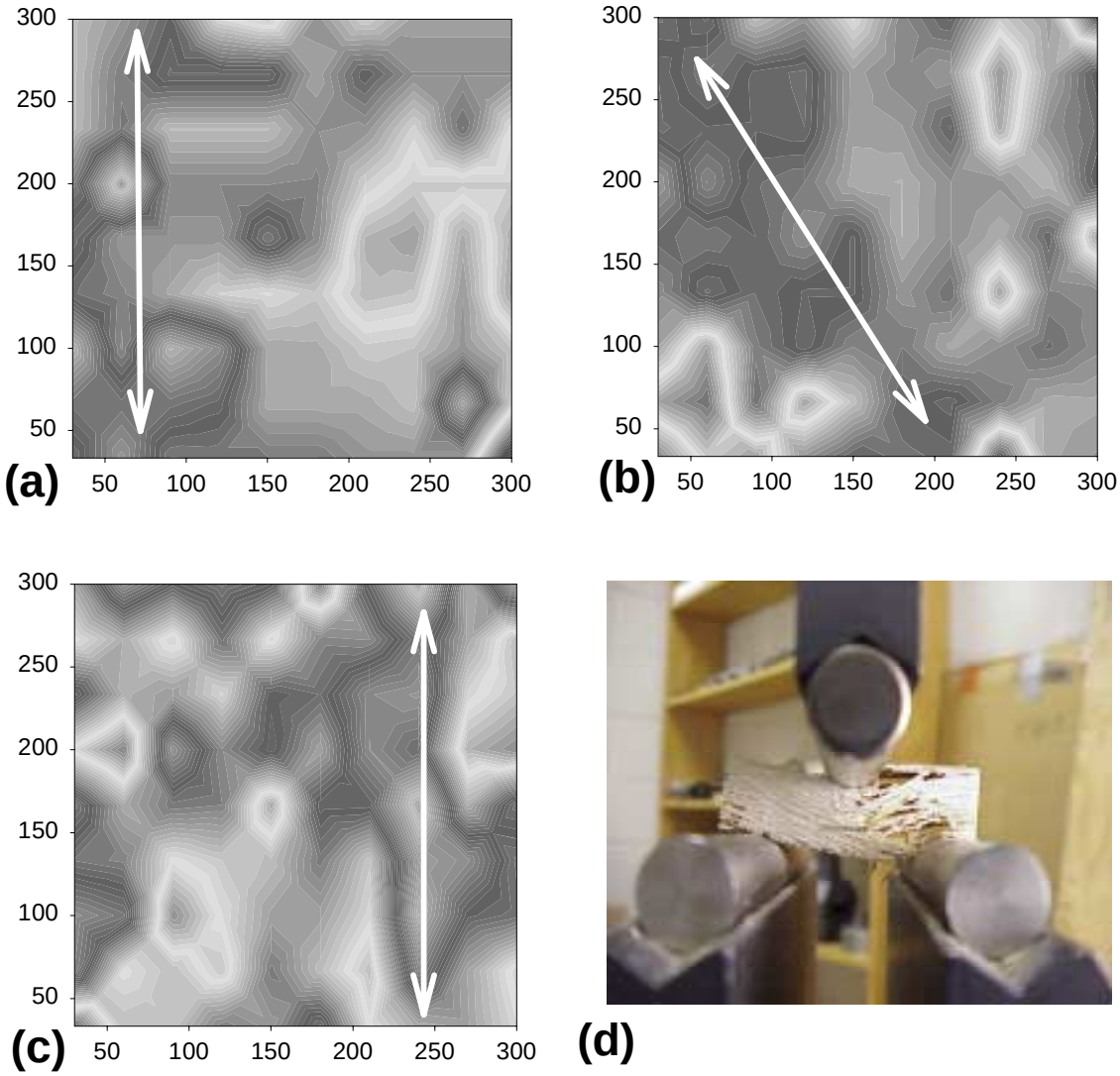

Fig. 6.9. Typical fracture directions (arrow) superimposed onto the measured average density distribution in the central moment area: along the loading head (a), oblique (b), intermediary transverse (c) directions for the three typical boards. The low-density zones (dark area) served as the defect trench for fracture initiation and propagation (d).

The low-density areas suffered the foremost critical damages, observed as breakage, splitting or delaminating.

In addition, coupled with the dynamic MC change and the maximum bending stress at the surface, the wood particles closest to the surface are the most readily to break, split, or delaminate (also observed in Bariska 1985). In high stress applications such as this study, most ruptures observed were proned to low-density zones as a defect trench (see **Fig. 6.9d)** – much more prevalent with wider density variation. Recognizing density variations do exist within specimens and between the boards, ability to control in-plane density variation within a certain tolerance could address the effects of defect distribution, in which most mechanical properties depend.

6.4. CONCLUSIONS

Specimens exposed to the high MC (24/24) conditioning have high thickness swelling (18%) due to the high compaction ratio of making the aspen OSB. This is adversely affected the panel resistance to creep. Under 80% ultimate stress, most failures occurring in the 24/24 specimens had reduced strength due to unrecoverable permanent deflection. As compared to the 12/12 specimens, the 24/24 specimens stiffness dropped by 27% to 5.08 Gpa and the strength by 23% to 18.7 MPa. The creep-rupture rate for the 24/24 specimens was the highest (1.43 mm/h) as the worst-case scenario as compared to the dynamic rising MC (12/24) specimens (0.27 mm/h) and the constantly low MC (12/12) specimens (0.04 mm/h). Although the specimen 12/24 creep rate was relatively smaller than that

24/24, the dynamic rising MC caused considerable damages, resulting in the largest CF of 2.28. The effect of dynamic moisture change at the surface of the specimen, therefore, is critical and posed immediate impact on creep, as shown by an accelerated stepwise deflection to failure.

Empirically, the impact of creep-rupture at the various test conditions can be predicted from the percent change from either CF or CM based on the instantaneous elastic deformation. A change of 56% in CF in 12/12 specimens and about 120% in both 24/24 and 12/24 specimens can be an indicator for impending failure. The recovered total creep in ambient or 12/12 conditions consisted of 85.2% instantaneous elastic, 5.4% viscoelastic, and 9.4% viscous deformations. The recovered total MOE consisted of 69.7% elastic, 10.4% viscoelastic, and 19.9% unrecoverable permanent MOE's. This commercial OSB had a 24-day creep-rupture limit.

Defects on the compression side of the specimen in a bending were found more critical in accelerating the creep rupture time than those on the tension side. This fact affirmed that surface protection or surface quality of a wood composite is a critical factor to consider the formulation of intrinsic factors to resist creep of a particular external use. A surface protective (temporary/permanent) barrier is recommended to prevent the adverse impact of moisture adsorptions or wetting when the boards are used in humid conditions. Complete protection of board bundles should be made when exposed at site construction. In addition, valleys of

low-density zones formed the defect trench for final failures – root from a wide horizontal density variation.

All AE cumulative parameters are highly correlated to deflection. In particular, cumulative event is a suitable substitute for deflection, because of its sensitivity and appropriate representation to incipient creep damages development in the central area of the specimen. The AE technology, therefore, has shown to be an effective tool in monitoring creep, potentially in fracture mechanism and source location evaluations, and appropriate in the analysis of horizontal density distribution in wood composites.

6.5. REFERENCES

Aicher, S., L. Hofflin, G. Dill-Langer. 2001. Damage evolution and acoustic emission of wood at tension perpendicular to fiber. Holz als Roh-und Werkstoff 59:104-116.

American Society for Testing and Materials. 1996. Annual Book of ASTM: Standard D3043-96, American Society for Testing and Materials (ASTM), Philadelphia, PA.

Arima, Takanori, N. Maruyama, and M. Sato. 1986. Creep of wood, wood-based materials and wood composite building elements at various conditions. International Union of Forest Resource Organizations. Grp S5.02. Jubljana, Jougoslavia.

Ayarkwa, J., Y. Hirashima, K. Ando, and Y. Sasaki. 2001. Monitoring acoustic emissions to predict modulus of rupture of finger-joints from tropical African hardwoods. Wood and Fiber Science 33(3):450-464.

Bach, Lars, N.W. Zhao, and J.J.R. Chang. 1993. Surface coating can reduce creep of OSB. Forest Products Journal 43(6):43-44.

Bariska, M. 1985. Creep and fracture phenomena in wood tissues. Pages 16-18 Vol. 1 *in* Proc. Symposium on Forest Products Research International - Achievements and the Future. Pretoria, S. Africa.

Beall, F.C. 1985. Relationship of acoustic emission to internal bonding strength of wood-based composite panel materials. Journal of Acoustic Emission 4(1):19-29.

Beall, F.C. 1986a. Effect of moisture conditioning on acoustic emission from particleboard. J. of Acoustic Emission 5(2):71-76.

Beall, F.C. 1986b. Effect of resin content and density on acoustic emission from particleboard during internal bonding. Forest Products Journal 36(7/8):29-33.

Beall, F.C., and W.W. Wilcox. 1987. Relationship of acoustic emission during radial compression to mass loss from decay. Forest Products Journal 37(4):38-42.

Beall, F.C. 1992. Use of acoustic emission in evaluating creep from wood composites. Pages 370-373 *in* Proc. 4th. International Symposium on Acoustic Emission from Composite Materials, July 27-31, 1992, Seattle, WA. American Society for Testing Materials, Columbus, Ohio.

Beall, F. C. 1994. Acoustic emission from oriented strandboard during flexural testing. Pages 143-148 *in* Proc. Progress in Acoustic Emission VII. The Japanese Society for Nondestructive Inspection, Sopporo, Japan.

Beall, F.C. 1996. Application of ultrasonic technology to wood and wood-based materials. Second International Conference on Development of Wood Science-Technology and Forestry. Sopron, Hungary. 10pp.

Beall, F.C. 2002. Overview of the use of ultrasonic technologies in research on wood properties. Wood Sci. Technol. (36): 197-212.

Beattie, A.G. 1983. Acoustic emission, principles and instrumentation. Journal of Acoustic Emission 2(1/2):95-128.

Bodig, J., and B.A. Jayne. 1993. Mechanics of wood and wood composites. Krieger Publishing Co., Malabar, Florida, 176-229 pp.

Bryan, E.L. and A.P. Schniewind. 1965. Strength and rheological properties of particleboard as affected by moisture content and sorption. Forest Products Journal 15(4):143-148.

Cavalloni, C., and A. Kirchheim. 1994. New acoustic emission sensors for in-process monitoring. Pages 91-97 *in* Proc. Progress in Acoustic Emission VII. The Japanese Society for Nondestructive Inspection, Sopporo, Japan.

Chen, T-Y. and J-S. Lin. 1997. Creep behavior of commercial wood-based boards under long-term loading at room conditions in Taiwan. Holz als Roh- und Werkstoff 55:371-376.

Choi, N.S. and K. Takahashi. 1994. Acoustic Emission during fracture process of short fiber reinforced plastics. Pages 445-450 *in* Progress in Acoustic Emission VII. The Japanese Society for Nondestructive Inspection, Sopporo, Japan.

Cyra, G., and C. Tanaka. 2000. The effects of wood-fiber directions on acoustic emission in routing. Wood Science and Technology 34(237-252.

Dill-Langer, G., T. Ringger, L. Höfflin, and S. Aicher. 2002. Locating acoustic emission sources in timber loaded parallel to grain. *In* 13th. International NDT2002 Symposium, 19-21 August, University of California, Berkeley, CA. Forest Products Society, Madison, WI.

Dinwoodie, J.M., C.B. Pierce, and B.H. Paxton. 1984. Creep in chipboard: Part 4. The influence of temperature and moisture content on the creep behavior of a range of boards at a single stress level. Wood Science & Technology 18:205-224.

Dinwoodie, J.M., B.H. Paxton, C.B. Pierce, and E.J. Aloysius. 1985. Quantification and prediction of creep in particleboard and other wood-based sheet materials. Pages 9-14 Vol. 6 *in* Proc. Symposium on Forest Products Research International-Achievements and the Future. Pretoria.

Dinwoodie, J.M., D.J. Robson, and J.S. Higgins. 1991. Creep in chipboard: Part 8. The effect of steady-state moisture content, temperature and level of stressing on the relative creep behavior and creep modulus of a range of boards at a single stress level. Wood Science & Technology 25:225-238.

Dinwoodie, J.M., J.S. Higgins, and D.J. Robson. 1992. Creep in particleboard: Part 11. The effect of cyclic changes in moisture content and temperature on the creep behavior of a range of boards at different levels of stressing. Wood Science & Technology 26:429-448.

Drouillard, T.F., and F.C. Beall. 1990. AE literature – Wood. Journal of Acoustic Emission 9(3): 215-222.

European Committee for Standardization. 1997. Wood-based panels: Determination of duration of load and creep factor. prENV 1156. CEN/TC112, Brussels.

Fridley, K.J. 1992. Designing for creep in wood structures. Forest Products Journal 42(3): 23-28.

Gressel, P. 1972. Effect of time, climate and loading on the creep behavior of wood based materials. Part I. Previous investigation, test plan and research methods. Part II. Test results dependent on creep parameters. Part III. Discussion of results. Holz Roh-Werkstoff 30:259-266, 347-355, 479-488.

Halligan, A. F., and A. P. Schniewind. 1972. Effect of moisture on physical and creep properties of particleboard. Forest Prod J 22(4):41-48.

Hamstad, M.A. 1986. A review: acoustic emission, a tool for composite materials studies. Experimental Mechanics 26(1):7-13.

Hamstad, M.A. 1994. An examination of piezoelectric polymers as wideband acoustic emission displacement sensors. Pages 79-86 *in* Proc. Progress in Acoustic Emission VII. The Japanese Society for Nondestructive Inspection, Sopporo, Japan.

Haygreen, J., H. Hall, and K.N. Yang. 1975. Studies of flexural creep behavior in particle board under changing humidity conditions. Wood and Fiber 7(2):74-90.

Hsu, N. Nelson, and Y. Tsukahara. 1994. Acoustic emission transmitted through a solid/fluid interface – Theory. Pages 553-558 *in* Proc. Progress in Acoustic Emission VII. The Japanese Society for Nondestructive Inspection, Sopporo, Japan.

Laufenberg, T.L. 1987. Creep testing of structural composite panels: A literature review and proposed standard. Pages 297-313 *in* T.M. Maloney ed. Proc. International Particleboard-Composite Materials Symposium. Washington State University, Pullman, WA.

Laufenberg, T.L. 1986. Creep and creep-rupture in reconstituted panel products. Pages 61-66 *in* Proc. International Workshop on Duration on Load in

Lumber and Wood Products. Special publ. no. SP-27. Forintek Canada Corp. Vancouver, B.C.

Leicester 1971. A rheological model for mechano-sorptive deflections of beams. Wood Science & Technology 5:211-220.

Lemaster, R.L., and F.C. Beall. 1996. The use of an optical profilometer to measure surface roughness in medium density fiberboard. Forest Products Journal 46(11/12):73-78.

Lemaster, R.L., F.C. Beall, and V.R. Lewis. 1997. Detection of termites with acoustic emission. Forest Products Journal 47(2):75-79.

National Forest Products Association. 1991. Design specification for wood construction. Washington DC.

McNatt, J.D., and T.L. Laufenberg. 1991. Creep and creep-rupture of plywood and oriented strandboard. Pages 3.457-3.464 *in* Proc. International Timber Engineering Conference. TRADA, London.

McNatt, J.D., R.W. Wellwood, and L. Bach. 1990. Relationships between small-specimen and large panel bending tests on structural wood-based panels. Forest Products Journal 40(9):10-16.

Moliñski, W. J. Raczkowski, and L. Muszyñski. 2000. Acoustic emission generated upon mechano-sorptive creep of wood bent across to the grain under asymmetrical moistening. Holzforschung 54:305-308.

Moren, T.J., and S.M. Sehlstedt-Persson. 1993. Creep response to drying of timber boards of Scots pine. Forest Products Journal 43(10): 58-64.

Niemz, P. 1981. Nature of creep deformation of particle boards. Holztechnologie 22:215-221.

Noguchi, M., Y. Fujii, M. Owada, Y. Imamura, M. Tokoro, and R. Tooya. 1991. AE monitoring to detect termite attack on wood of commercial dimension and posts. Forest Products Journal 41(9):32-36.

Pierce, C. B., J. M. Dinwoodie, and B. H. Paxton. 1979. Creep in chipboard: Part 2. The use of fitted response curves for comparative and predictive purposes. Wood Science & Technology 13:265-282.

Pritchard, J., M.P. Ansell, R.J.H. Thompson, and P.W. Bonfield. 2001. Effect of two relative humidity environments on the performance properties of MDF, OSB and chipboard. Wood Science & Technology 35:405-423.

Pu, J.H., R.C. Tang, and W.C. Davis. 1992a. Creep behavior of commercial oriented strandboards under high relative humidity. Forest Products Journal 42(4): 49-54.

Pu, J.H., R.C. Tang, and E.W. Price. 1992b. Effect of hot and humid environmental conditions on the creep of commercial structural oriented strandboard. Forest Products Journal 42(11/12):9-14.

Rice, R.W., and D.P. Phillips. 2001. Estimating the moisture excluding effectiveness of surface coatings on Southern Yellow pine using acoustic emission technology. Wood Science & Technology 34:533-542.

Sato, K., N. Kamei, M. Fushitani, and M. Noguchi. 1984. Discussion of tensile fracture of wood using acoustic emissions: a statistical analysis between the relationships of AE and fracture stress. Journal of Japan Wood Research Society 30(8):653-659.

Schniewind, A. P. 1967. Creep-rupture life of Douglas fir under cyclic environmental conditions. Wood Sci Technol 1:278-288.

Schniewind, A. P., S.L. Quarles, and S-H Lee. 1996. Wood fracture, acoustic emission and the drying process: Part 1. Acoustic emission associated with fracture. Wood Science & Technology 30:273-281.

Stanzl-Tschegg, S.E., D.M. Tan, and E.K. Tschegg. 1996. Fracture resistance to the crack propagation in wood. Journal of Fracture 75:347-356.

Sugiyama, Hideo. 1967. On the effect of the loading time on the strength properties of wood. Wood Sci Technol 1:289-303.

Van Wyk, W.J., and G.F.R. Gerischer. 1985. Creep behavior of laminated pine beams under sustained loading. Pages 3-22 Vol. 4 *in* Proc. Symposium on Forest Products Research International. Pretoria, S. Africa.

Vun, R.Y, and F.C. Beall. 2002. Monitoring creep rupture in oriented strandboard using acoustic emission. *In* International NDT2002 Symposium, 19-21 August 2002. University of California, Berkeley, CA.

Tang, R.C., J.H. Pu and E.W. Price. 1997. Effect of temperature on the creep of commercial oriented strandboards under cyclic relative humidity. Forest Products Journal 47(7/8): 100-106.

Yeh, M.C., R.C. Tang and C.Y. Hse. 1990. Flexural creep of structural flakeboard under cyclic humidity. Forest Products Journal 40(10): 51-57.

CHAPTER 7. CONCLUSIONS

Nondestructive characterization of engineering performance in oriented strandboard (OSB) and particleboard using active ultrasonic methods and passive acoustic emission technology were performed. From the results of the study, the following conclusions can be deduced.

1. Silicon gel-coupled direct-contact (DC) and air-coupled non-contact (NC) ultrasonic methods were developed and suitably used to characterize engineering properties of aspen OSB in a through-thickness ultrasonic transmission (UT) mode. For both methods, the UT responses correlated nonlinearly to sample density and not affected by the panel shelling ratio for the three-layer boards. UT variables attenuation and root means square voltage (RMS) were suitably used as density predictors if the flake alignment level is known, or otherwise velocity parameter could be used. The internal bond (IB) strength, bending stiffness, and breaking resistance in single-layer boards were highly correlated to attenuation and RMS. The density of 900 kg/m^3 marked the transition point for the UT responses. The high correlations of DC-Velocity and NC-Attenuation to density and strength properties attest a feasible application of both methods in wood composite research and in a real time quality control for bio-based composite facilities.

2. The DC method was found suitable to map and validate the horizontal density distribution in southern pine OSB. The UT variables velocity, attenuation, and RMS formed excellent complementary predictors of density for all resin content (RC) and panel types. Based on the allowable ±10% variation in the average measured densities, both the General and Polynomial Models provided improved density prediction for boards at higher RC and nominal density (ND) levels. Using the contour and out-of-limits plots, the predicted *in-situ* densities gave a reasonable spatial approximation to the measured densities. Panel densities of 0.60 g/cm^3 or greater conformed well to the limits, with declining conformity towards the lower RC panels.
3. The NC UT technique was used successfully to locate and map the spatial properties of southern pine OSB. Control charts and spatial graphic plots produced reasonable resemblance to the measured density distributions in OSB. With the high transduction transducers, NC ultrasonic was found to be a sensitive tool to match the local representation of internal constituents of the wood composites. With the advantage of non-physical contact between the sensor and specimen, NC UT broke the technological limitations over the other nondestructive techniques that requiring physical contacts.
4. The direct contact through transmission ultrasonic method was successfully used to differentiate the effect of size particulates on panel properties

among the different reconstituted bio-products, including a flake-type OSB, granular-type red cedar particleboard (RCPB), and fine particle bagasse particleboard (BAPB). Internal bond (IB) strength improved with the amount of surface area of particles. The equilibrium moisture content of the panel types increased with increasing particle size. Both attenuation and RMS voltage were found to be good indicators of moisture change in the single layer RCPB, while velocity was not. However, the ultrasonic velocity was found to be a good indicator of the particulate physical impediment to the ultrasonic waves; velocity decreased with increasing particle size for OSB and RCPB, but not for BAPB. The variable impedance was also a measure of tortuosity of velocity flux through the material. Minimum attenuation and maximum RMS points for RCPB, OSB, and BAPB were obtained at approximate density values 0.75, 0.9, and 1.1 g/cm^3, respectively, marking lesser void scattering and absorption with respect to size particles in each panel type. For the respective panel types, these density values indicated the greatest transmissivity of stress wave energy at these points – so-called the "zero void density." Beyond these densities, absolute IB appeared to be diminishing with density. Hence, an appropriate ultrasonic system calibration of these material factors is essential for optimization of desired properties and a technological bridge for these reconstituted composites.

5. The creep rupture phenomenon in large specimens of commercial aspen OSB were successfully studied with an acoustic emission (AE) technique. Compared to deflection, the cumulative event AE parameter was found more sensitive and an appropriate representation to the accumulation of incipient damages until final failure. Under the 80% ultimate stress level, the high MC condition caused the highest creep-rupture rate (1.43 mm/h) as compared to the dynamic rising MC and low MC conditions (0.27 and 0.04 mm/h, respectively). The accelerated step-like deflection in the constantly rising MC specimens was critically devastating to rupture, with the largest creep factor of 2.28. The total recovered deflection in ambient conditions was attributable to 85.2% recoverable elastic, 5.4% recoverable viscoelastic, and 9.4% permanent irreversible deflections. Correspondingly, the total recovered stiffness was attributable to 69.7% recoverable elastic, 10.4% recoverable viscoelastic, and 19.9% permanent irreversible. The observed creep limit of the commercial OSB was 24 days to failure. Defects on the compression-side of the bending specimen were found to be more critical than those on the tension-side in creep rupture. In-plane fracture patterns followed the defect trenches of low-density valleys, worsening with larger density variation, a concern for controlling horizontal density variation in OSB.

The results of this research indicate that bio-based composites can be developed to meet specific service performance needs, based on the integrity of

structural adequacy, dimensional stability and bond performance. The nondestructive evaluation approaches, i.e., the contact and non-contact ultrasonic methods and the acoustic emission, present a viable alternative tool toward the optimization of strength and density for a particular composite design for certain engineering properties and service performance.

VITA

Ronnie hailed from Kota Belud town in the West Coast of the State of Sabah, east Malaysia. After he graduated with a baccalaureate diploma in forestry from the Agricultural University of Malaysia (Universiti Pertanian Malaysia) at Kuching, Sarawak in 1984, he joined the Sabah Foundation. He helped manage the foundation's one-million hectare of forest concession in timber operations and forest inventory planning for six-years. From his work, he was and still is inspired to fully utilize the limited forest resources into useful products. He completed a bachelor of science degree in forest products engineering *magna cum laude* and a master's in forestry both from the University of the Philippines at Los Baňos in 1994 and 1995, respectively. He returned to work for two years assisting the forestry upstream group manager and the forestry consultant before he proceeded to the University of California at Berkeley (UCB). He completed another master of science degree in wood science and technology in 1998. His research entailed, "creep rupture monitoring in oriented strandboard (OSB) using an acoustic emission technique," one of the many nondestructive evaluation techniques he learned at UCB. At the Louisiana State University, he applied the ultrasonic technique to investigate the gross internal structure that caused horizontal density variation in OSB, a defect trench for fracture

initiation and propagation. He also designed and converted other bio-resources into useful reconstituted panels by optimizing the different particle strength properties. His research work was well recognized and awarded the second prize of the 54th Annual Wood Award for the year 2003 by the Forest Products Society. He is interested to impart his knowledge in institution of higher learning, or to continue his development and research responsibility for better quality panels and manufacturing in the industries.